DETERMINATION OF ASTROPHYSICAL DIRECT CAPTURE REACTION RATE FOR ^{26}Si(p,γ)^{27}P BY EXTRACTING THE ASYMPTOTIC NORMALIZATION COEFFICIENTS IN THE MIRROR NUCLEAR SYSTEM

A Dissertation

by

MURAT DAG

Submitted to the Office of Graduate and Professional Studies of
Texas A&M University
in partial fulfillment of the requirements for the degree of

DOCTOR OF PHILOSOPHY

Chair of Committee,	Robert E. Tribble
Committee Members,	Carl A. Gagliardi
	Charles M. Folden III
	Che-Ming Ko
Head of Department,	Peter McIntyre

December 2016

Major Subject: Physics

ABSTRACT

The $^{26}Si(p,\gamma)^{27}P$ reaction is of primary interest to this study in connection with its role in the destruction of the important astrophysical observable ^{26}Al. Due to very limited experimental information, more experimental data are clearly needed in the calculation of the $^{26}Si(p,\gamma)^{27}P$ reaction rate at the temperature of astrophysical interest. However, the reaction rate information for $^{26}Si(p,\gamma)^{27}P$ cannot be obtained today with direct measurements. Hence, it was decided to study the $^{26}Si(p,\gamma)^{27}P$ reaction using the indirect asymptotic normalization coefficient (ANC) technique. In this method, $^{26}Si(p,\gamma)^{27}P$ can be studied by means of its mirror nuclear systems $^{26}Mg+n\rightarrow^{27}Mg$, and the reaction rate for the radioactive proton capture $^{26}Si(p,\gamma)^{27}P$ at stellar energies can be determined through measurements of the ANC in the mirror nuclear system $^{26}Mg+n\rightarrow^{27}Mg$. For this reason, $^{13}C(^{26}Mg,^{26}Mg)^{13}C$ and the single neutron transfer channel $^{13}C(^{26}Mg,^{27}Mg)^{12}C$ measurements were performed. The extracted neutron asymptotic normalization coefficient for ^{27}Mg was used to determine the reaction rate for $^{26}Si(p,\gamma)^{27}P$. As a part of this dissertation, the elastic scattering of ^{28}Si and ^{32}S on ^{13}C experiments were also performed using the newly upgraded Oxford detector. The extracted optical parameters along with an overview of the upgrade process of the Oxford detector are presented.

ACKNOWLEDGEMENTS

This dissertation would not have been possible without the help of a multitude of people. First and foremost is my advisor, Prof. Robert Tribble who has generously given me his time and support over the years. His inspiring enthusiasm, knowledge, and guidance assisted me to complete this dissertation. I am indebted for all that he has taught me over the years.

I also would like to express my sincere gratitude to Prof. Carl A. Gagliardi for his valuable guidance and help throughout my project, and Prof. Charles M. Folden III and Prof. Che-Ming Ko for serving as committee members and for their time, and helpful input to my work.

I would like to convey my special thanks to Dr. Matthew McCleskey for his great patience in answering my questions, and his knowledge shared with me. A similar note of thanks is extended to Dr. Ellen McCleskey for her kindness friendship and helpful suggestion.

I am grateful to the member of the RET group, Dr. Brian Roeder, Dr. Antti Saastamoinen, Ms. Alexandria Spiridon and Mr. Roman Chyzh for their time and help with these measurements. I also would like to thank Dr. Vladilen Goldberg for sharing his knowledge with me.

Additionally, I must thank the DHY group, Dr. Y.-W Lui and Dr. J. Button for their contributions and generous help in preparing the experimental setup on the MDM spectrometer. I owe a similar vote of thanks to GRG group, in particular H. Jayatissa, S. Upadhyayula, J. Hooker, C. Hunt and C. Magana for their time and help in taking data.

I would like to extend my grateful appreciation to Dr. A. Mukhamedzhanov and especially Dr. D. Pang for their time and help to make input file for FRESCO code. I must extend a similar note of thanks to Dr. T. Abdullah for answering my questions. I would like to express my gratitude to the Ministry of National Education in Turkey for

providing me the option to pursue my Ph.D. at Texas A&M University. Finally, I would like to thank my family for all their support throughout graduate school.

TABLE OF CONTENTS

LIST OF FIGURES

Page

LIST OF TABLES

Page

CHAPTER I

INTRODUCTION

Nuclear astrophysics -the union of astrophysics and nuclear physics- is of great importance in building a coherent picture of the universe. In particular, the origin of the elements is of particular interest in this subfield. Intimately, this is tied to the production and evolution of stars, leading to stellar nucleosynthesis.

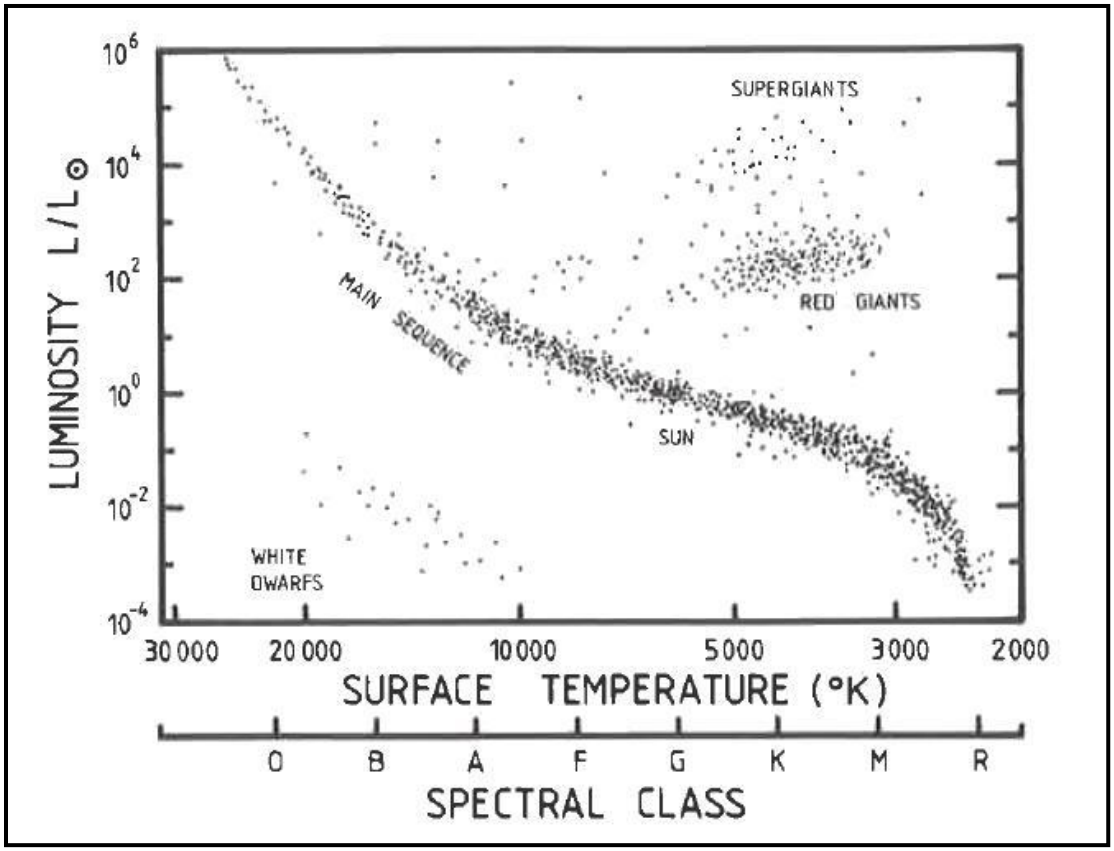

Figure 1: The Hertzsprung-Russell (H-R) diagram [1].

The Hertzsprung - Russell diagram

One of the tools used to classify stars into groups and to understand their evolving patterns is the Hertzsprung-Russell diagram (hereafter HR), as seen in Figure 1. In the HR diagram the effective surface temperatures of stars (or color, or spectral class) is plotted against their luminosity (as a ratio to that of the Sun).

Stellar Evolution and Processes

The majority of isolated stars, including our sun, are main sequence stars, as seen in Figure 1. As the temperature in the core of the star reaches about 10^7 K, thermonuclear reactions begin by converting hydrogen to helium called hydrogen burning. The outward expansion of the star due to hydrogen burning balances the gravitation force. The star will settle into a long-lived state, where gravitational contraction is temporarily halted [1].

On the other hand, one of the crucial elements that determine stars evolution is the initial mass of the proto-star. Hence, if the initial mass of proto-star is equal to or less than 0.1 solar masses, it may not able to have self-sustaining hydrogen burning due to insufficient mass. This is called a brown or black dwarf and is completely outside of the main sequence [1]. If the initial mass is between 0.08 and 0.4 solar masses, then it is known as a red dwarf, which has hydrogen fusing to helium in its core [2].

A star on the main sequence remains in its original position as long as the thermonuclear energy generated in its interior is sufficient enough to balance the gravitational contraction. The main two ways for burning hydrogen in a main sequence star is either through the pp chain for masses $M<1.5M_{\odot}$ or via the "cold" CNO (carbon-nitrogen-oxygen) cycles in heavier stars. Once all the hydrogen in the core has been consumed, the star leaves the main sequence, and moves to the red giant branch where helium burning creates carbon and oxygen in the core. The hydrogen layer above the core continues burning hydrogen through the CNO cycle. Once all the helium is consumed,

the star contracts since there is no internal nuclear energy to halt the gravitational contraction [2]. If the star is less massive than 4 solar masses, it never develops the necessary temperatures or central pressures to initiate thermonuclear reactions that use carbon and oxygen as a fuel. Instead, the process of mass ejection strip away from the outer layers of the star and leaves behind the star with a dense core of carbon-oxygen called a white dwarf [2].

If the initial mass is higher than 4 solar masses, carbon burning begins as the central temperature reaches 6.10^8 K. This thermonuclear process produces oxygen, neon, sodium, and magnesium. If a star has a mass of about 8 solar masses, the process of neon burning begins at around 10^9 K after the cessation of carbon burning. Throughout the process the neon accumulated from carbon burning is used up, and further increases the concentrations of oxygen and magnesium in the star's core. In a similar manner, oxygen burning starts and the principal product of oxygen burning is sulfur. Once oxygen burning is over, silicon burning begins, resulting in the creation of heavier elements up to nickel (Ni). The star now has a Fe/Ni core, which, as shown in Figure 2, is surrounded by an onion shell-like structure containing unburned silicon, oxygen, neon, carbon, helium, and hydrogen. The outer shells continue burning, adding heavier nuclei to the core. The gravitational contraction commences again to increase the core temperature and density, but, on the contrary to the previous burning stage, no ignition occurs in the Fe/Ni core due to very high binding energies of the Fe/Ni in the core. Hence, once the Chandrasekhar limit of $1.4M_{\odot}$ is exceed, the star collapses on itself and produces a shockwave that propagates outward from the core. This shockwave heats up the outer shells causing explosive nucleosynthesis. It leads to the ejection of mass from the outer shells to the interstellar medium, and leaves behind a neutron star or black hole. This explosive scenario is termed a core collapse supernova explosion [2].

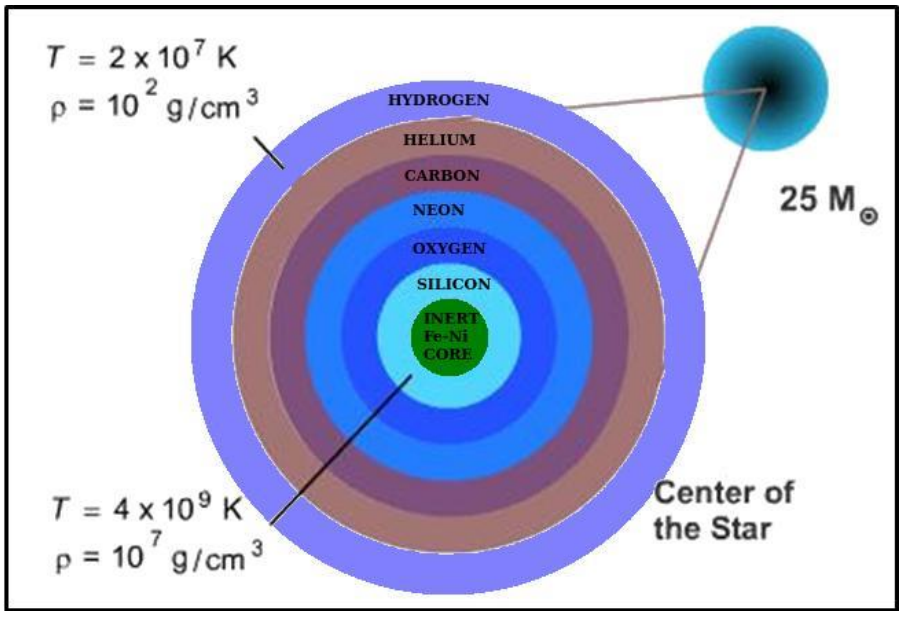

Figure 2: A giant star with an Fe/Ni core and burning layers.

Nucleosynthesis of Heavy Elements

The effectiveness of fusion reactions reduces in a star that has evolved to a stage where it has a Fe/Ni core, because iron is the most stable element. But, sufficient gravitational pressure to contract and heat the residues causes further transmutation reactions initiating the production of heavier elements.

An effective method of nucleosynthesis beyond this point is the neutron capture process which is responsible for synthesizing heavier nuclei. Neutron capture reactions play a significant role in the observed abundances of the heavy elements since in contrast to proton captures, neutron captures are not hindered by the Coulomb barrier. There are two neutron capture processes contributing to the synthesis of elements beyond the iron region: the s- and r- processes create neutron-rich nuclei. The s-process produces nuclei close to stability, while the r-process produces very neutron-rich radioactive nuclei, far from stability. Radioactive proton capture reactions also contribute to the synthesis

process even though their contribution to the observed abundances of the heavy elements is small. There are two dominant reaction mechanisms which are responsible for producing proton rich nuclei: the p- and rp- process. The p-process produces nuclei which are neutron-deficient with A≥74 (between selenium to mercury). This process is dominated by a series of (γ,n), (γ,p), and (γ,α) photo-disintegration, and occurs likely in outer layers of core-collapse supernova.

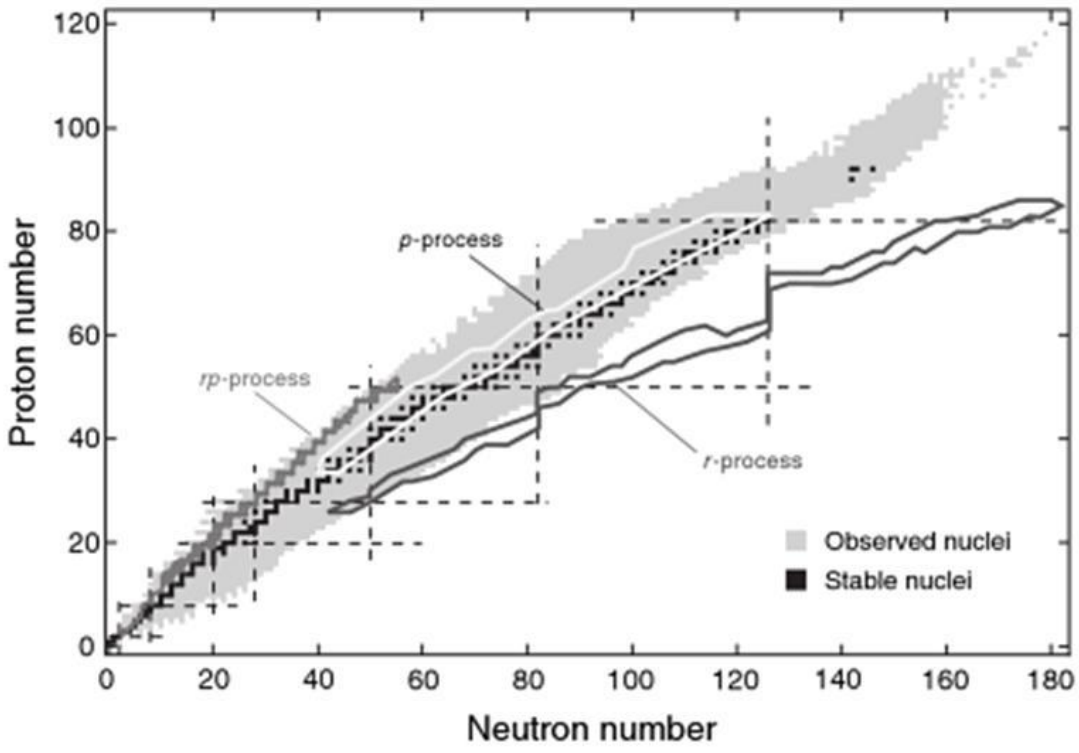

Figure 3: The predicted rp- process path on the valley of the stability. Figure courtesy of [3].

The Rapid Proton Capture Process (rp-Process)

The other process by which proton-rich nuclei are synthesized is the rapid proton capture process (rp-process), which occurs through a sequence of (p,γ) and (α,p) capture reactions and subsequent β-decays. The path of this process lies between the proton drip line and the line of stability, as shown in Figure 3. Even though it does not contribute significantly to the overall production of elements, the rp-process is primarily important for synthesizing many of the light and medium proton-rich nuclei [3].

The reaction mechanism that primarily contributes to the rp-process is the radioactive proton capture reaction in which the seed nucleus (X) captures an energetic proton to form new nucleus (Y) while emitting a gamma ray. A general representation for a radioactive proton capture reaction is shown below.

$$ {}^{A}_{Z}X + p \rightarrow {}^{A+1}_{Z+1}Y + \gamma \quad or \quad X(p,\gamma)Y \tag{1.1} $$

The newly produced nucleus repeats the proton capture process, leading towards the proton drip line as long as the newly formed nucleus is stable or has a relatively long beta-decay half-life. As the number of captured proton increases, the nucleus becomes more unstable, and thus can undergo rapid β-decay toward a more stable system. This suggestion was first presented by B2FH (Burbridge, Burbridge, Fowler and Hoyle), and has been improved thereafter [3].

The stellar environments favoring the rp-process are X-ray bursts, novae, and supernovae, which are under astrophysical conditions of extreme temperature and density [3, 4].

Binary Star Systems

A binary star system consists of two stars that revolve around a common center of gravity. Probably as many as one-half of the stars in our Galaxy are members of binary systems, but only a small percentage are members of a close binary system [2].

In a close binary system, each star is surrounded by a hypothetical surface illustrating its gravitational region, called the Roche lobe, which is shown as a dashed figure-eight curve in Figure 4. The point where two Roche lobes touch is termed as the Inner Lagrangian point in which the effects of gravity and rotation cancel each other. If the material of two stars is within the Roche lobe, the binary system then is stable. When one of the stars starts evolving off the main sequence, it may fill its Roche lobe surface and then material is flown onto its companion through the inner Lagrangian point. This can occur for binary systems that contain a compact object, either a neutron star or a white dwarf [1, 2].

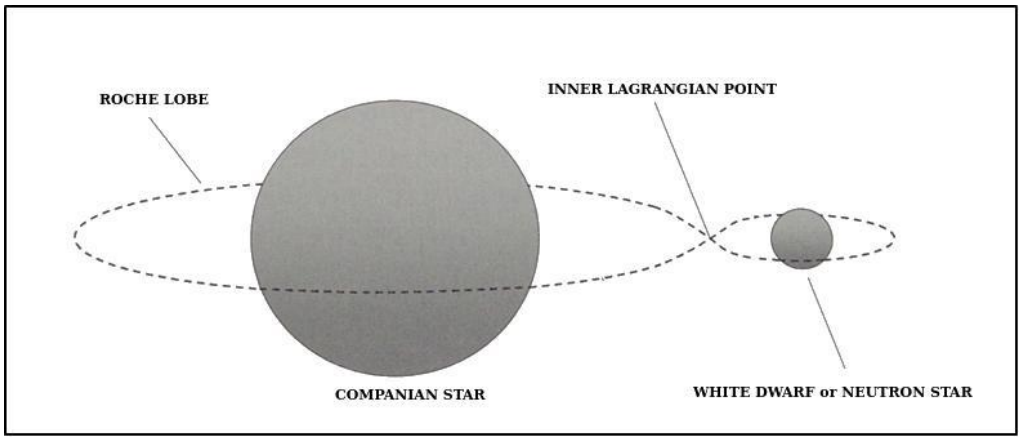

Figure 4: The gravitational region of each star in a close binary system is illustrated. A dashed-figure-eight curve represents the Roche Lobe.

Classical Novae

Classical novae are stellar explosions that occur in close binary systems in which one member is a white dwarf. In this case, the hydrogen-rich envelope material from a companion star which has filled its Roche lobe is transferred onto the white dwarf companion. A white dwarf with masses on the order of 1 solar mass is usually composed of carbon-oxygen (C-O), while if its mass in the range 1.2 – 1.4 solar masses, then it can be composed of oxygen-neon-magnesium (O-Ne-Mg). A white dwarf, which previously has used all of its available hydrogen and helium fuel by converting it to carbon and oxygen, has a very strong gravitational field due to its high density. The transferred matter from the companion star accumulates onto the white dwarf surface, as shown in Figure 5 [1]. Because of strong surface gravity, the material accreting onto the white dwarf surface is compressed and hence heated. The temperature becomes high enough to fuse hydrogen to helium via pp chain reactions during the accretion phase, causing a gradual increase of the temperature. At some point, the bottom of the accreted layer becomes electron degenerate. As its temperature increases, the envelope does not inflate due to electron degeneracy, and thus a thermonuclear runaway occurs near the base of the accreted layers at the temperature T= 0.1-0.2 GK for C-O white dwarf and T= 0.4-0.5 GK for an O-Ne-Mg white dwarf. At this period, explosive hydrogen burning via hot CNO cycles dominates. The NeNa cycle and the MgAl cycle are the other cycles that can also occur [4].

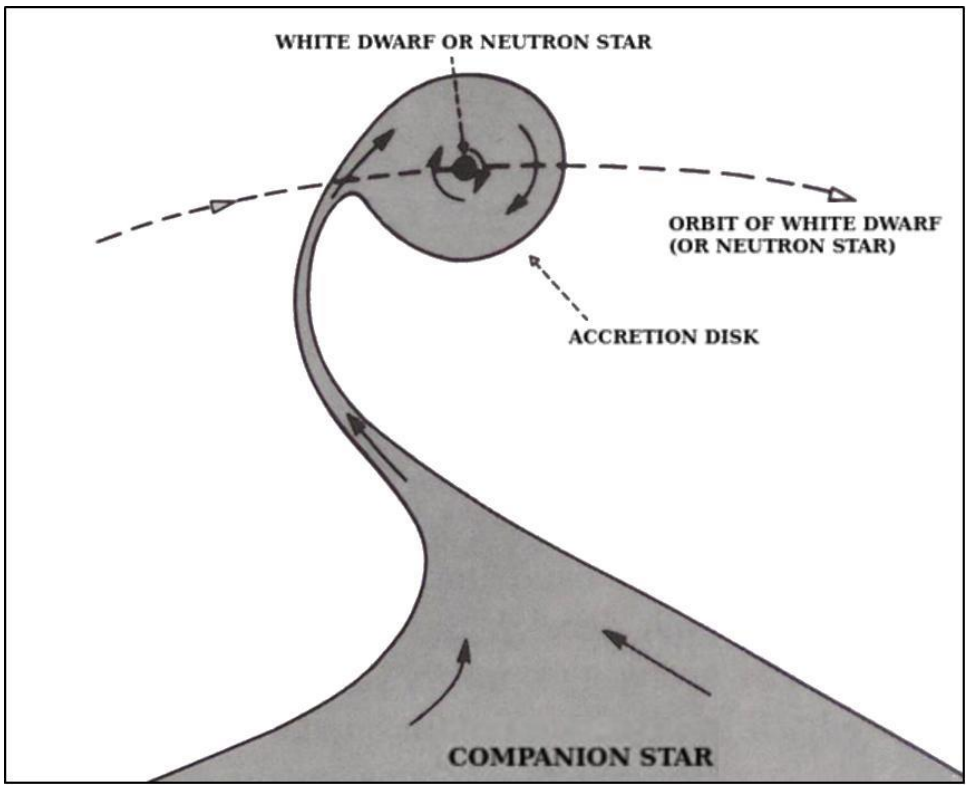

Figure 5: A binary system is represented schematically [1].

X-Ray Bursts

X-Ray Bursts, the most frequent types of thermonuclear stellar explosions in the galaxy, typically may last only 5-10 seconds. The first X-Ray bursts were reported in 1976. Among the most explosive events in the galaxy are X-Ray bursts, which emit energy of $\sim 10^{40}$ ergs [4].

X-Ray burst events occur in a close binary system involving a neutron star, which is denser than a white dwarf. When the neutron star's companion star begins to expand as part of its normal evolution on the main sequence, the hydrogen-rich material accreted from the companion star is funneled onto the surface of the neutron stars via Roche lobe overflow. The material from a companion star is continuously accreted onto the neutron

star surface, as seen in Figure 5, and is compressed until the temperature and density are high enough to ignite nuclear reactions.

At the surface of the neutron star, the accumulated material forms a hot dense medium due to the gravitational pull of the neutron star. Under relatively higher density (10^6–10^8 g/cm^3) and high temperature hydrogen starts to burn via the hot CNO cycle. As temperatures and densities on the surface of neutron star reach over 10^9 K and 10^6 g/cm^3 respectively, X-Ray bursts explosions occur [5]. At this stage, there will be a rapid series of (p,γ) and (α,p) reactions. These reactions will produce a series of unstable proton-rich nuclei up to the A~60 mass region [3], which subsequent beta decay with gamma decays from excited states of daughter nuclei.

Scientific Motivation For The Study of ^{26}Si(p,γ)^{27}P Reaction

The existence of the radioisotope ^{26}Al (half-life 7.17 x 10^5 years) provides significant evidence in the interstellar medium in our galaxy for ongoing nucleosynthesis in stars since its half-life is short compared to the time scale of the chemical evolution of the universe. Several stellar sites have been suggested as a source for the production of ^{26}Al such as novae, supernovae, Wolf Rayet (WR) stars, and Asymptotic Giant Branch (AGB) stars [2, 6].

The possible reaction sequence for production of ^{26}Al, as seen in Figure 6, is ^{24}Mg(p,γ)^{25}Al(β+ν)^{25}Mg(p,γ)^{26}Al, and after ≈7x10^5 years ^{26}Al decays to ^{26}Mg (g.s.) by a beta decay and then emits 1.809 MeV γ-ray .

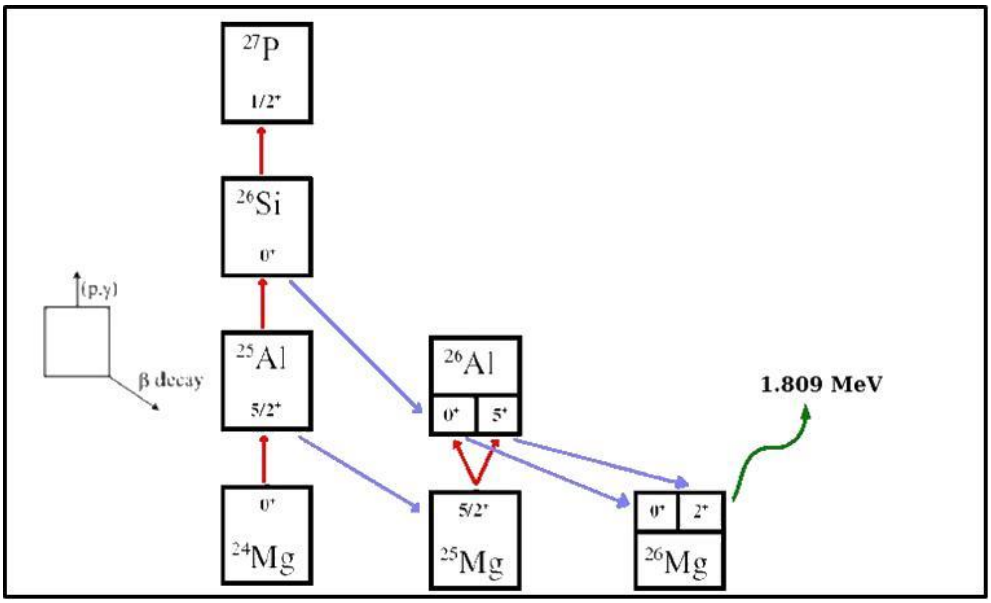

Figure 6: Possible reaction sequences for production and decay of ^{26}Al.

The γ-rays from radioactive ^{26}Al were first discovered by the HEAO3 satellite and reported by [7, 8]. It was later measured by the COMPTEL telescope installed on the CGRO (Compton Gamma Ray Observatory) satellite and INTEGRAL [9], and mapped out in an all-sky distribution of 1.809 MeV γ-rays over the galaxy, as seen in Figure 7.

However, because of the proton capture on ^{25}Al being faster than its β-decay in the sites which have high stellar density and temperature, the dominant chain of the production of ^{26}Al can be by-passed through ^{25}Al(p,γ)^{26}Si(p,γ)^{27}P [10].

In the conditions where the temperature is above 0.4 GK, the isomeric state of ^{26}Al can be produced via the reaction sequence ^{25}Al(p,γ)^{26}Si(β+ν)^{26}Al^{m}, where the β-decay of ^{26}Si feeds only the isomeric state of ^{26}Al. Since the ground and isomeric state of ^{26}Al are in thermal equilibrium above 0.4 GK, this path affects the synthesis of ^{26}Al. The depletion of ^{26}Si by a (p,γ) reaction is thus of interest for determining the quantity of the ground state of ^{26}Al produced through thermal equilibrium [10].

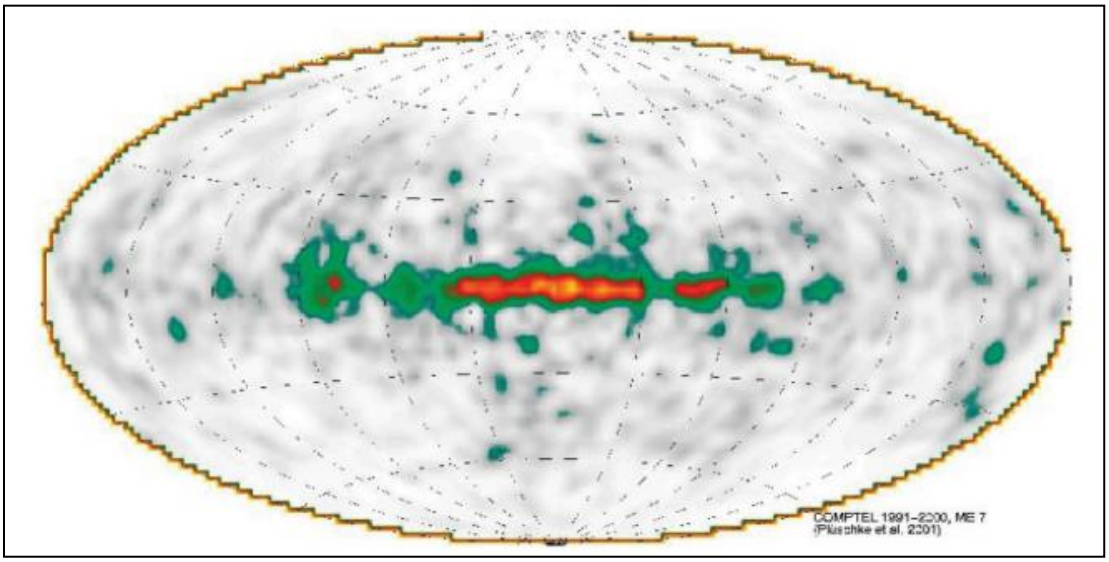

Figure 7: An all-sky distribution of 1.809 MeV γ-rays over the galaxy [11].

In connection with its role in the destruction of the important astrophysical observable ^{26}Al, the proton-capture reaction ^{26}Si(p,γ)^{27}P thus is significant. The reaction rate for ^{26}Si(p,γ)^{27}P has been estimated based on theoretical models where appropriate nuclear structure information is available [12, 13]. However, the uncertainty of the ^{26}Si(p,γ)^{27}P reaction rate is quite large because of very limited experimental information. Hence, the ^{26}Si(p,γ)^{27}P reaction related to the rp-process in novae and X-ray bursts is of primary interest of this dissertation.

Objectives

As noted above, the reaction ^{26}Si(p,γ)^{27}P is important due to its potential role in the destruction of ^{26}Al. However, due to very limited experimental information, the uncertainty of the ^{26}Si(p,γ)^{27}P reaction rate is quite large. Since it cannot be studied today with direct measurements due to unstable radioactive beams and targets required, the low cross section values at stellar energies, and low favored stellar energy band, the aim of this work is to estimate the reaction rate for ^{26}Si(p,γ)^{27}P from the asymptotic

normalization coefficient (ANC) in the mirror nuclear system ^{26}Mg(n,γ)^{27}Mg. Moreover, the optical model parameters for the elastic scattering of ^{28}Si and ^{32}S on ^{13}C are extracted to better understand the optical model parameters that are needed for 26Mg and other systems around ^{26}Mg as well.

Dissertation Outline

This dissertation consists of five chapters. Chapter I is the introduction, which presents the background and motivation for this work. Chapter II covers the theoretical basis of this work, including the extraction procedure of asymptotic normalization coefficients (ANC) in peripheral transfer reactions. The next chapter, Chapter III, presents the experimental setups and details, including the multipole-dipole-multipole (MDM) spectrometer, the Oxford detector and its upgrade process, and data acquisition system. The pre-analysis procedures that need to be followed prior to starting data analysis, the detailed analysis of data and the extraction of the optical model parameters from the various measurements, and the extraction of the ANC for the reaction ^{26}Si(p,γ)^{27}P are presented in Chapter IV. Chapter V covers the results of the determined reaction rate. Chapter VI presents a conclusion.

CHAPTER II

THEORY

Nonrelativistic Kinematics for Nuclear Reactions

If a target $\mathcal{A}$ of mass $m_{\mathcal{A}}$ is bombarded by a particle a of mass m_a and results in a nucleus $\mathcal{B}$ with emitted particle b, this is commonly expressed in one of two ways.

$$a + \mathcal{A} \rightarrow \mathcal{B} + b \quad or \quad \mathcal{A}(a,b)\mathcal{B}\,. \tag{2.1}$$

The combination of $\mathcal{A}$ and a is called the *entrance channel*, while that of $\mathcal{B}$ and b is called the *exit channel*.

The kinetic energy of the entrance channel in the laboratory system is

$$E_{lab} = \frac{1}{2} m_a v_a^2 + \frac{1}{2} m_{\mathcal{A}} v_{\mathcal{A}}^2. \tag{2.2}$$

where $m_{a(\mathcal{A})}$ and $v_{a(\mathcal{A})}$ are the mass and velocity of $a(\mathcal{A})$, respectively.

Using the laboratory coordinates [4], the position of the center of mass $\vec{R}$ and the relative position $\vec{r}$ are defined as

$$\vec{R} = \frac{m_a \vec{r_a} + m_{\mathcal{A}} \vec{r_{\mathcal{A}}}}{m_a + m_{\mathcal{A}}}, \tag{2.3}$$

$$\vec{r} = \vec{r_a} - \vec{r_{\mathcal{A}}}. \tag{2.4}$$

The corresponding kinetic energy in the center of mass (c.m.) can be rewritten in terms of the velocity of c.m., $\mathcal{V}_{cm}$, and the relative velocity, $\mathcal{v}$.

$$\boldsymbol{E = \frac{1}{2}\,\mathcal{M}\mathcal{V}_{cm}^{2} + \frac{1}{2}\mu\mathcal{v}^{2}},\tag{2.5}$$

where the velocity of c.m., $\mathcal{V}_{cm}$, and the relative velocity, $\mathcal{v}$ are

$$\boldsymbol{\mathcal{V}_{cm} = \frac{m_{a}\mathcal{v}_{a} + m_{\mathcal{A}}\mathcal{v}_{\mathcal{A}}}{m_{a} + m_{\mathcal{A}}}},\tag{2.6}$$

$$\boldsymbol{\mathcal{v} = \mathcal{v}_{a} - \mathcal{v}_{\mathcal{A}}}.\tag{2.7}$$

where $\mathcal{M} = m_{a} + m_{\mathcal{A}}$ and $\mu = m_{a}m_{\mathcal{A}} / m_{a} + m_{\mathcal{A}}$ are the total and reduced masses, respectively.

In the Eq. (2.5). the first term is a sum of the energy of motion of c.m., and the second is the energy of relative motion. In a case when particle a with energy E_{a} is incident on a stationary target $\mathcal{A}$, the kinetic energy in c.m. is related to the laboratory system by

$$\boldsymbol{E_{cm} = \frac{m_{\mathcal{A}}}{\mathcal{M}}\,E_{a} = \frac{1}{2}\mu\mathcal{v}_{a}^{2}}.\tag{2.8}$$

Stellar Reaction Rates and the Gamow Window

Reaction Rate

The reaction rate of a nuclear reaction is defined as the cross section, $\sigma(\mathcal{v})$, where $\mathcal{v}$ represents the relative velocity between the projectile and the target nuclei.

If we assume a stellar plasma with N_a particles per cubic centimeter of the projectile a and $N_{\mathcal{A}}$ particles per cubic centimeter of the target $\mathcal{A}$, with the relative velocity v, the rate of nuclear reactions [14] is given by

$$\boldsymbol{r}(\boldsymbol{v}) = \boldsymbol{N_a N_{\mathcal{A}} \sigma_v v}. \tag{2.9}$$

The relative velocity of particles varies over the stellar gas, and the distribution of relative velocities is given by the probability function $\phi(v)$, which is normalized to unity.

$$\int \boldsymbol{\phi}(\boldsymbol{v})\boldsymbol{dv} = \mathbf{1}. \tag{2.10}$$

Hence, the reaction rate per particle pair $< \sigma v >$ is given by

$$< \boldsymbol{\sigma v} > = \int \boldsymbol{\phi}(\boldsymbol{v})\boldsymbol{v}\boldsymbol{\sigma}(\boldsymbol{v})\mathbf{d}\boldsymbol{v}. \tag{2.11}$$

The total reaction rate $\mathfrak{R}$ will then be

$$\boldsymbol{\mathfrak{R}} = \boldsymbol{N_a N_A} \int \boldsymbol{\phi}(\boldsymbol{v})\boldsymbol{v}\boldsymbol{\sigma}(\boldsymbol{v})\boldsymbol{dv}. \tag{2.12}$$

Maxwell-Boltzmann Distributions

For nuclei moving nonrelativistically in a non-degenerate stellar gas in thermodynamic equilibrium, the velocities of the nuclei are given by a Maxwell-Boltzmann velocity distribution, where T and m refers to the temperature of the gas and the mass of the nucleus of interest, respectively.

$$\boldsymbol{\phi(v)} = \left(\frac{\boldsymbol{m}}{\boldsymbol{2\pi kT}}\right)^{\frac{3}{2}} \exp\left(-\frac{\boldsymbol{mv^2}}{\boldsymbol{2kT}}\right). \tag{2.13}$$

Considering that the interacting nuclei a and $\mathcal{A}$ are respectively moving with v_a and $v_{\mathcal{A}}$, the Maxwell-Boltzmann velocity distributions [1], $\Phi(v_a)$ and $\Phi(v_{\mathcal{A}})$, are then given by

$$\boldsymbol{\phi(v_a)} = \left(\frac{\boldsymbol{m_a}}{\boldsymbol{2\pi kT}}\right)^{\frac{3}{2}} \exp\left(-\frac{\boldsymbol{m_a v_a^2}}{\boldsymbol{2kT}}\right), \tag{2.14}$$

$$\boldsymbol{\phi(v_{\mathcal{A}})} = \left(\frac{\boldsymbol{m_{\mathcal{A}}}}{\boldsymbol{2\pi kT}}\right)^{\frac{3}{2}} \exp\left(-\frac{\boldsymbol{m_{\mathcal{A}} v_{\mathcal{A}}^2}}{\boldsymbol{2kT}}\right). \tag{2.15}$$

The reaction rate per particle pair $< \sigma v >$ can be written as

$$< \boldsymbol{\sigma v} > = \int\int \boldsymbol{\phi(v_a)\phi(v_{\mathcal{A}})\sigma(v_a - v_{\mathcal{A}})(v_a - v_{\mathcal{A}})dv_a dv_{\mathcal{A}}}. \tag{2.16}$$

The expanded expression $\boldsymbol{\phi(v_a)\phi(v_{\mathcal{A}})}$ is

$$\boldsymbol{\phi(v_a)\phi(v_{\mathcal{A}})} = \frac{(\boldsymbol{m_a m_{\mathcal{A}}})^{\frac{3}{2}}}{\boldsymbol{(2\pi kT)^3}} \exp\left(-\frac{\boldsymbol{(m_a v_a^2 + m_{\mathcal{A}} v_{\mathcal{A}}^2)}}{\boldsymbol{2kT}}\right). \tag{2.17}$$

The variables v_a and $v_{\mathcal{A}}$ are related to the variables v and $\mathcal{V}_{\text{cm}}$ by the kinematic relations shown in Eq. (2.6) and Eq. (2.7). The last expression in Eq. (2.17) therefore can be rewritten by analogy using the c.m. velocity

$$\boldsymbol{\phi(v)\phi(V_{cm}) = \frac{(m_a m_{\mathcal{A}})^{\frac{3}{2}}}{(2\pi kT)^3} \exp\left(-\frac{(m_a + m_{\mathcal{A}}){V_{cm}}^2}{2kT} - \frac{(m_a m_{\mathcal{A}})v^2}{2kT(m_a + m_{\mathcal{A}})}\right).} \quad (2.18)$$

Then we need the Jacobian transformation to adjust the differentials. Using Eq. (2.6) and Eq. (2.7), we get

$$\boldsymbol{dv dV_{cm} = \begin{vmatrix} \frac{\partial v}{\partial v_a} & \frac{\partial v}{\partial v_{\mathcal{A}}} \\ \frac{\partial V_{cm}}{\partial v_a} & \frac{\partial V_{cm}}{\partial v_{\mathcal{A}}} \end{vmatrix} dv_a dv_{\mathcal{A}} = \begin{vmatrix} \frac{1}{m_a + m_{\mathcal{A}}} & \frac{-1}{m_{\mathcal{A}} + m_{\mathcal{A}}} \end{vmatrix} = dv_a dv_{\mathcal{A}}.}$$

The reaction rate per particle pair in the c.m. can be written as

$$\boldsymbol{< \sigma v > = \int\int \phi(v)\phi(V_{cm})\sigma(v) v dv dV_{cm}.} \quad (2.19)$$

Substituting Eq. (2.18) in Eq. (2.19), the reaction rate per particle pair will be

$$\boldsymbol{< \sigma v > = \left(\frac{m_a m_{\mathcal{A}}}{2\pi kT}\right)^{\frac{3}{2}} \left(\frac{1}{2\pi kT}\right)^{\frac{3}{2}} \int\int \sigma(v) v dv dV_{cm}\, exp\left(-\frac{M{V_{cm}}^2}{2kT} - \frac{\mu v^2}{2kT}\right).} \quad (2.20)$$

where $\mu = m_a m_{\mathcal{A}} / m_a + m_{\mathcal{A}}$ and $\mathcal{M} = m_a + m_{\mathcal{A}}$.

Multiplied by $\left(\frac{m_a + m_{\mathcal{A}}}{m_a + m_{\mathcal{A}}}\right)^{\frac{3}{2}}$, $< \sigma v >$ is

$$\boldsymbol{\left(\frac{M}{2\pi kT}\right)^{\frac{3}{2}} \int exp\left(-\frac{M{V_{cm}}^2}{2kT}\right) dV_{cm} \cdot \left(\frac{\mu}{2\pi kT}\right)^{\frac{3}{2}} \int \sigma(v) v dv\, exp\left(-\frac{\mu v^2}{2kT}\right).} \quad (2.21)$$

The first part of Eq. (2.21) is merely the integral of a Maxwell-Boltzmann distribution and is by definition equal to 1 as shown in Eq. (2.10). The second part describes the distribution over their relative velocity v. Hence, the reaction rate per particle pair integral simplifies to

$$< \sigma v > = \left(\frac{\mu}{2\pi kT}\right)^{\frac{3}{2}} \int \sigma(v) v dv \, exp\left(-\frac{\mu v^2}{2kT}\right). \tag{2.22}$$

By integrating along the radial velocity direction in spherical coordinates, it becomes

$$< \sigma v > = 4\pi \left(\frac{\mu}{2\pi kT}\right)^{\frac{3}{2}} \int \sigma(v) v dv \, exp\left(-\frac{\mu v^2}{2kT}\right). \tag{2.23}$$

Using the center-of-mass energy $E = \mu v^2/2$ as defined in Eq. (2.8), Eq. (2.23) can be rewritten as Eq. (2.24) by transforming the variable of integration to the energy E

$$< \sigma v > = \left(\frac{8}{\pi\mu}\right)^{\frac{1}{2}} \frac{1}{(kT)^{\frac{3}{2}}} \int_0^\infty E\sigma(E) exp\left(-\frac{E}{kT}\right) dE. \tag{2.24}$$

The reaction rate can be determined using this expression at a given stellar temperature. But, depending on the temperature changes in stellar matter, it needs to be evaluated for each temperature of interest. To simplify the evaluation process, it is typical to obtain an analytical expression that is determined by the energy dependence of the cross section σ(E). However, its dependence differs with regards to the type of the reaction mechanism, which is either non-resonant or resonant.

Non-resonant Reactions

A nucleus is a positively charged entity, and thus two colliding nuclei repel each other with a force that is proportional to the product of their nuclear charges. This repulsive force leads to a potential barrier called the Coulomb barrier. The potential energy due to this repulsive force when the nuclei do not overlap has the form

$$V_C(r) = \frac{Z_1 Z_2 e^2}{r}, \tag{2.25}$$

where the symbols Z_1 and Z_2 indicate the number of protons of the interacting nuclei, and r is the distance between nuclei.

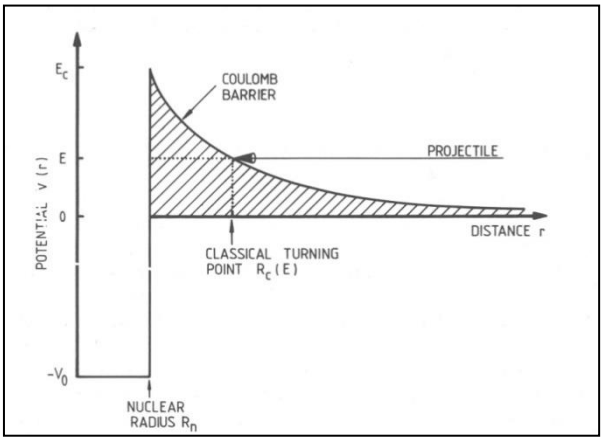

Figure 8: Schematic representation of the combined nuclear and Coulomb potentials. A projectile with energy $E<E_C$ must penetrate the Coulomb barrier to reach the nuclear domain [1].

In order to accomplish the fusion reaction, nuclei must have sufficient energy to overcome this Coulomb barrier, as seen in Figure 8. In a classical condition, this is an insurmountable barrier to surpass. However, quantum mechanically there is a small but

not insignificant probability for the particles with energies $E<E_c$ to tunnel through the Coulomb barrier.

This tunneling probability at low energy where $E < E_c$ can be approximated as

$$\boldsymbol{P \propto \exp(-2\pi\eta)}. \tag{2.26}$$

The quantity η is called the Sommerfeld parameter and is equal to

$$\boldsymbol{\eta = \frac{Z_1 Z_2 e^2}{\hbar v}}. \tag{2.27}$$

In order to compare the tunneling probability with the cross section, the coefficient of proportionality needs to be established. For this reason, the cross section for two interacting particles must be proportional to the de-Broglie wavelength of the particles since nuclei have a wave-like spatial distribution.

$$\boldsymbol{\sigma \propto \pi\lambda^2 \propto \frac{1}{E}}. \tag{2.28}$$

The cross section can then be expressed as

$$\boldsymbol{\sigma(E) = \frac{1}{E}\exp(-2\pi\eta)\, S(E)}, \tag{2.29}$$

where the quantity S(E) is termed the astrophysical S-factor, which contains all the contributions from nuclear effects. For the non-resonant reactions, S(E) is a smoothly varying function over a broad range of energies, and thus is useful while extrapolating

the measured cross section to the astrophysical energies. If Eq. (2.30) is inserted in Eq. (2.24), we get [1]

$$< \sigma v > = \left(\frac{8}{\pi\mu}\right)^{\frac{1}{2}} \frac{1}{(kT)^{\frac{3}{2}}} \int_0^{\infty} S(E) exp\left(-\frac{E}{kT} - \frac{b}{\sqrt{E}}\right) dE, \qquad (2.30)$$

where the quantity b is given by

$$b = (2\mu)^{\frac{1}{2}} \frac{\pi e^2 Z_1 Z_2}{\hbar} = 31.27 Z_1 Z_2 \mu^{\frac{1}{2}} (keV)^{\frac{1}{2}}. \qquad (2.31)$$

Since S(E) varies slowly with energy for non-resonant reactions, only the exponential term defines the behavior of the integral in Eq. (2.30). The first term is for a Maxwell-Boltzmann distribution, which is large at low energies and small at high energies. On the other hand, the penetration through the Coulomb barrier is determined by the second term, which is small at low energies and large at high energies, as shown in Figure 9.

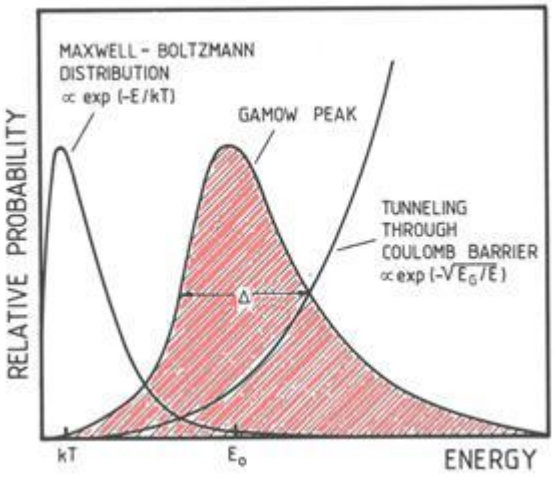

Figure 9: The energy – dependent functions of the Maxwell-Boltzmann distribution function, the quantum mechanical tunneling function through the Coulomb barrier, and the convolution of the functions, which result in a peak (Gamow peak) are shown.

The product of these two terms produces a sharply peaked function near the energy E_0, which is called Gamow window. Nuclear reactions take place mainly in this energy window defined by

$$\boldsymbol{E = E_0 \pm \frac{\Delta}{2}}, \tag{2.32}$$

where E_0 is termed the Gamow peak, which is also known as the effective mean energy for thermonuclear reactions at a given temperature T, determined by

$$\boldsymbol{E_0 = \left(\frac{bkT}{2}\right)^{\frac{2}{3}} = 1.22\left(Z_1 Z_2 \mu T_6^2\right)^{\frac{1}{3}}\ keV}. \tag{2.33}$$

Δ (the Gamow window) is the FWHM (full width at half maximum) of the shaded curve in Figure 9., and is given by

$$\boldsymbol{\Delta = \frac{4}{\sqrt{3}}\left(E_0 kT\right)^{\frac{1}{2}} = 0.749\left(Z_1^2 Z_2^2 \mu T_6^5\right)^{\frac{1}{6}}\ keV}. \tag{2.34}$$

Because the energy where nuclear reactions occur in stellar environments is too low to measure the reaction cross section directly in the laboratory [15, 16], S(E) typically can be found over a range of available laboratory energies and then extrapolated down to astrophysical energies. Then, if the S(E) is approximately constant, the non-resonant reaction rate per particle pair can be estimated as

$$\boldsymbol{< \sigma v > = \left(\frac{2}{\mu}\right)^{\frac{1}{2}} \frac{\Delta}{(kT)^{\frac{3}{2}}}\ S(E_0) \exp\left(-\frac{3E_0}{kT}\right)}. \tag{2.35}$$

On the contrary, if the S-factor varies significantly around the Gamow peak rather than being a constant, then it can be expanded in a Taylor series about zero energy up to the quadratic term and Eq. (2.35) becomes as shown in Eq. (2.38).

$$\boldsymbol{S(E) \approx S(0) + E\,S'(0) + \frac{1}{2}\,E^2\,S''(0)}. \tag{2.36}$$

$$\begin{aligned} \boldsymbol{S_{eff}(E_0) = \left(1 + \frac{5kT}{36E_0}\right) S(0) + \left(E_0 + \frac{35}{36}kT\right) S'(0)} \\ \boldsymbol{+ \frac{1}{2}\,E_0\left(E_0 + \frac{89}{36}\,kT\right) S''(0)}. \end{aligned} \tag{2.37}$$

$$\boldsymbol{< \sigma v > = \left(\frac{2}{\mu}\right)^{\frac{1}{2}} \frac{\Delta}{(kT)^{\frac{3}{2}}}\, S_{eff}(E_0) \exp\left(-\frac{3E_0}{kT}\right)}. \tag{2.38}$$

Non-resonant reactions are reactions with a one-step process, where a direct transition into a bound state occurs. Direct capture is one example of a non-resonant reaction. There are other types of non-resonant reactions such as pickup and stripping reactions, coulomb excitation, and charge-exchange processes.

Resonant Reaction

In contrast to the non-resonant reactions, there is another type of reaction mechanism where an excited state of the compound nucleus is first formed in the entrance channel, and subsequently decays to lower lying states. This process only happens if the energy of the entrance channel matches the energy of the excited state in the compound nucleus.

In the formation of compound nuclei [1], the system is created at an excitation energy, which has a certain energy width, Γ that is related to the decay mean life of the state τ by the uncertainty principle such that

$$\boldsymbol{\Gamma\tau} = \hbar. \tag{2.39}$$

The width and shape of the resonance state is given by the Breit-Wigner formula, such that the nuclear reaction cross-section [1, 14]

$$\boldsymbol{\sigma(E)} = \frac{\boldsymbol{\lambda^2}}{\boldsymbol{4\pi}} \frac{\boldsymbol{2J_r + 1}}{\boldsymbol{(2J_p + 1)(2J_t + 1)}} \frac{\boldsymbol{\Gamma_p \Gamma_\gamma}}{\boldsymbol{(E - E_r)^2 + \left(\frac{\Gamma}{2}\right)^2}}. \tag{2.40}$$

The labels p, t and r refer to the projectile, target and resonance. The J's are the respective intrinsic angular momenta (spins) of the nuclei involved. Γ_p is the partial width of the entrance channel, Γ_γ is the partial width of the exit channel and $\Gamma = \Gamma_p + \Gamma_\gamma$ is the total reaction width. The partial widths are much akin to line widths in that they are an energy range tolerance over which the reaction can occur. Because Γ_p is proportional to the tunneling probability, the Gamow window remains critical to determining which excitation energy states can contribute meaningfully to the reaction rate.

To estimate the rate of a resonance reaction in stars, σ(E) in Eq. (2.40) can be substituted into Eq. (2.30). For a narrow resonance, $\Gamma \ll E_r$, the Maxwell-Boltzmann distribution barely changes, hence the narrow resonance reaction rate per particle pair is given by

$$< \boldsymbol{\sigma v} > = (\hbar^2 \boldsymbol{\omega\gamma}) \left(\frac{\boldsymbol{2\pi}}{\boldsymbol{kT\mu}}\right)^{\frac{3}{2}} \boldsymbol{exp}\left(-\frac{\boldsymbol{E}}{\boldsymbol{kT}}\right), \tag{2.41}$$

where the quantity ωγ is known as the resonance strength, which is

$$\boldsymbol{\omega} = \frac{\mathbf{2}\boldsymbol{J_r} + \mathbf{1}}{\left(\mathbf{2}\boldsymbol{J_p} + \mathbf{1}\right)\left(\mathbf{2}\boldsymbol{J_t} + \mathbf{1}\right)} \; \boldsymbol{and} \; \boldsymbol{\gamma} = \frac{\boldsymbol{\Gamma_p}\boldsymbol{\Gamma_\gamma}}{\boldsymbol{\Gamma}}. \tag{2.42}$$

The Derivation of Scattering Amplitude and DWBA

For the reaction a + X → Y + b, the Schrödinger equation [17] is given by

$$(\boldsymbol{H} - \boldsymbol{E})\boldsymbol{\Psi} = \mathbf{0}. \tag{2.43}$$

where H is the total Hamiltonian, E is the total energy, and Ψ is the total wave function that includes the information on all open reactions channels. The Hamiltonian H can be expressed in terms of any partition channel

$$\boldsymbol{H} = \boldsymbol{H_\alpha} + \boldsymbol{T_\alpha} + \boldsymbol{V_\alpha} = \boldsymbol{H_\beta} + \boldsymbol{T_\beta} + \boldsymbol{V_\beta}. \tag{2.44}$$

where the total Hamiltonian for the system is the sum of the internal Hamiltonians for the particles a and X, ($H_\alpha = H_a + H_X$), the kinetic energy of their relative motion, and the potential energy, respectively. The Schrödinger equation then can be rewritten as in Eq. (2.45). Here V_α is the potential energy, while T_α is the kinetic energy for the entrance channel, α.

$$(\boldsymbol{E} - \boldsymbol{H_\alpha} - \boldsymbol{T_\alpha})\boldsymbol{\Psi} = \boldsymbol{V_\alpha}\,\boldsymbol{\Psi_\alpha}. \tag{2.45}$$

To determine an equation that represents the motion in the exit channel, Eq. (2.45) can be multiplied by Φ_β and integrated over the internal coordinates. The result will be

$$(\boldsymbol{E_\beta - T_\beta})\boldsymbol{\psi_\beta} = (\boldsymbol{\Phi_\beta}, \boldsymbol{V_\beta \Psi_\alpha}). \tag{2.46}$$

where $\boldsymbol{\psi_\beta} \equiv (\boldsymbol{\Phi_\beta}, \boldsymbol{\Psi_\beta})$ is given by

$$(\boldsymbol{\Phi_\beta}, \boldsymbol{\Psi_\beta}) \equiv (\boldsymbol{\Phi_\beta}|\boldsymbol{\Psi_\beta}) = \int \boldsymbol{\Phi_\beta^*}\, \boldsymbol{\Psi_\beta}\, \boldsymbol{d}(\boldsymbol{internal\ coordinates}).$$

Eq. (2.46) can be rewritten using the Green's function which gives a solution of the corresponding equation

$$(\boldsymbol{E_\beta - T_\beta})\boldsymbol{G_\beta^0}(\overrightarrow{\boldsymbol{r_\beta}} - \overrightarrow{\boldsymbol{r_\beta}}') = \boldsymbol{\delta}(\overrightarrow{\boldsymbol{r_\beta}} - \overrightarrow{\boldsymbol{r_\beta}}'). \tag{2.47}$$

By direct substitution the solution to Eq. (2.46) can be written

$$\boldsymbol{\Psi_\beta} = \int \boldsymbol{G_\beta^0}\,(\overrightarrow{\boldsymbol{r_\beta}}, \overrightarrow{\boldsymbol{r_\beta}}')(\boldsymbol{\Phi_\beta}, \boldsymbol{V_\beta \Psi_\alpha})\boldsymbol{d}\overrightarrow{\boldsymbol{r_\beta}}. \tag{2.48}$$

A solution to Eq. (2.47) is

$$\boldsymbol{G_\beta^{0(+)}}(\vec{\boldsymbol{r}} - \vec{\boldsymbol{r}}') = -\left(\frac{\boldsymbol{2m_\beta}}{\boldsymbol{4\pi\hbar^2}}\right)\frac{\mathbf{exp}(\mathbf{ik_\beta} \boldsymbol{r})}{\boldsymbol{r}}\mathbf{exp}(-\boldsymbol{i}\vec{\boldsymbol{k}}_\beta'.\vec{\boldsymbol{r}}). \tag{2.49}$$

The scattering amplitude can be found by inserting Eq. (2.49) into Eq. (2.48) as

$$\boldsymbol{f_{\beta\alpha}}(\boldsymbol{\theta}) = -\frac{\boldsymbol{m_\beta}}{\boldsymbol{2\pi\hbar}} \int \boldsymbol{exp}(-\boldsymbol{i}\vec{\boldsymbol{k}}_\beta'.\vec{\boldsymbol{r}})\,(\boldsymbol{\Phi_\beta}, \boldsymbol{V_\beta \Psi_\alpha^+})\boldsymbol{d}\vec{\boldsymbol{r}}. \tag{2.50}$$

Using the following convention, the scattering amplitude [17] can be rewritten as the $\mathcal{T}$ matrix in Eq. (2.51)

$$< \boldsymbol{\Phi_\beta}, \boldsymbol{\Psi_\alpha} > \equiv < \boldsymbol{\Phi_\beta} | \boldsymbol{\Psi_\alpha} > = \int \boldsymbol{\Phi_\beta^*}\, \boldsymbol{\Psi_\alpha}\, \boldsymbol{d(all\ coordinates)}.$$

$$\boldsymbol{I_{\beta\alpha}} = < \boldsymbol{\phi_\beta} |\, \boldsymbol{V_\beta} | \boldsymbol{\Psi_\alpha^{(+)}} >. \tag{2.51}$$

where $\boldsymbol{\phi_\beta}$ is the wave function describing the plane wave motion of a free particle

$$\boldsymbol{\phi_\beta} = \mathbf{exp}(-\boldsymbol{i}\vec{\boldsymbol{k}}_{\boldsymbol{\beta}}.\vec{\boldsymbol{r}})\, \boldsymbol{\Phi_\beta}. \tag{2.52}$$

In Eq. (2.51) the relative motion of the particles in the outgoing channel is represented by a plane wave, while the entrance channel includes the exact wave function that contains a description of all processes that occur. To calculate the exact wave function is typically not possible. But, even if it were possible to compute Ψ_α, the overlap for $\boldsymbol{I_{\beta\alpha}}$ would be an inefficient procedure. It thus is useful to introduce a potential U(r) which describes the relative motion in this channel and depends only on the relative coordinate between nuclei in the given channel. This potential can be chosen in such a way that it would describe the elastic scattering well. Then, the direct reactions can be thought of as perturbations. After following similar manipulations as are used from Eq. (2.46) to (2.51), Eq. (2.51) [17] becomes

$$\boldsymbol{I_{\beta\alpha}} = < \boldsymbol{\chi_\beta^{(-)}} \boldsymbol{\Phi_\beta} |\, \boldsymbol{V_\beta} - \boldsymbol{U_\beta} | \boldsymbol{\Psi_\alpha^{(+)}} >. \tag{2.53}$$

Here $\boldsymbol{\chi_\beta}$ is a distorted wave which describes the motion in the exit channel due to the potential U.

Optical Model Potential

The amplitude for a transition of the system from one partition to another was derived, and the reaction defined by Eq. (2.51) contains Ψα, the exact solution to the many-body

scattering problem involving a large number of possible reaction channels. For the reduction of the complicated many-body problem to a two-body problem, the optical model potential can be useful as it offers a simple way to characterize the interaction of two nuclei through a potential U(r), where $\vec{r}$ refers to the relative coordinate of the two particles in the channel. This potential is inherently complex and its imaginary part takes into account the absorption of the reaction flux from the elastic channel to the non-elastic reaction channels. The values of the model parameters can be obtained empirically by fitting the elastic scattering or calculated from microscopic models, and used for DWBA calculations [17].

The most common form of the potential is

$$\boldsymbol{U(r) = V(r) + \ i[\ W(r) + W_S(r)] + V_{SO}(r) + V_C(r).} \qquad (2.54)$$

where V refers to the real part of the potential, which is important for the elastic scattering part, while W is for the absorptive potential. W_S, V_{SO}, and V_C respectively represent surface, spin-orbit and Coulomb potential.

Typically two different shapes are mostly used for fitting the elastic scattering: the Woods-Saxon and the Double Folding potential.

The Woods-Saxon Potential

The interaction potential is generally described by an attractive nuclear well of the form [18]

$$\boldsymbol{V(r) = \frac{V_0}{1 + \exp\left(\frac{r - R_0}{a_0}\right)}.} \qquad (2.55)$$

Here $\boldsymbol{V_0}$ is the central depth, while $\boldsymbol{a_0}$ is the surface diffuseness. $\boldsymbol{R_0}$ is the nuclear radius, and is often parameterized as

$$\boldsymbol{\mathcal{R}_0 = r_0\left(a^{\frac{1}{3}} + A^{\frac{1}{3}}\right).} \tag{2.56}$$

where $\boldsymbol{r_0 \approx 1.2\ fm}$. This potential is usually combined with an imaginary part.

$$\boldsymbol{U(r) = -V(r) + iW(r).} \tag{2.57}$$

In case of charged particles, the Coulomb potential also must be taken into account. At small distance where a charged projectile is close to a target nucleus, the Coulomb potential is determined by the charged distribution of the two nuclei, whereas at large distance it is simply calculated in the sense of potential of two point charges. Hence, for a uniform change distribution, the Coulomb contribution to the potential is

$$\boldsymbol{V_C = Z_a Z_{\mathcal{A}} e^2} * \begin{cases} \left(\dfrac{3}{2} - \dfrac{r^2}{2R_C^2}\right)\dfrac{1}{R_C}. & \boldsymbol{for\ \ r \le R_C} \\ \dfrac{1}{r}\ . & \boldsymbol{for\ r > R_C} \end{cases} \tag{2.58}$$

The Double Folding Potential

An alternative method to analyze scattering data is to use the double folding potential to obtain the optical model potential. In this method, the nuclear density distributions first need to be calculated in a standard Hartree-Fock procedure. Then a double integration, as shown in Eq. (2.59) is performed over the two nuclei in order to obtain the potential.

$$\boldsymbol{V_{fold}(r) = \int d\vec{r}_1 \int d\vec{r}_2 \rho_1(\vec{r}_1)\rho_2(\vec{r}_2)v_{eff}(\vec{r}_1 + \vec{r} - \vec{r}_2)}. \quad (2.59)$$

For the nucleon-nucleon interaction potential ($\boldsymbol{v_{eff}}$) which depends on the local densities and the energy of the incident particle, JLM (the Jeukenne, Lejeune and Mahaux) was used [19]. Hence, Eq. (2.59) is rewritten as

$$\boldsymbol{V(r) = \int\int d\vec{r}_1 d\vec{r}_2 \rho_1(\vec{r}_1)\rho_2(\vec{r}_2)v_0(\rho, E)\delta(\vec{s})}, \quad (2.60)$$

where $\vec{\boldsymbol{s}} = \boldsymbol{\vec{r}_1 + \vec{r} - \vec{r}_2}$.

$$\boldsymbol{v_0(\rho, E) = \frac{V_0(\rho, E) + iW_0(\rho, E)}{\rho}}, \quad (2.61)$$

where V and W respectively are real and imaginary parts for NN interactions. The local density is approximated as

$$\boldsymbol{\rho = \left[\rho_1\left(\vec{r}_1 + \frac{\vec{s}}{2}\right)\rho_2\left(\vec{r}_2 + \frac{\vec{s}}{2}\right)\right]^{\frac{1}{2}}}. \quad (2.62)$$

The general form in JLM in Eq. (2.60) is improved by replacing the delta function with a Gaussian form factor given by

$$\boldsymbol{g(\vec{s}) = \left(\frac{1}{t\sqrt{\pi}}\right)^{\frac{1}{3}} \exp\left(\frac{-\vec{s}^2}{t^2}\right)}. \quad (2.63)$$

Here t is a range parameter, and the final form of the double folding potential is

$$U(r) = N_v V_{fold}(r) + iN_w W_{fold}(r). \quad (2.64)$$

Asymptotic Normalization Coefficients (ANC)

The asymptotic normalization coefficient (ANC) is one of the indirect techniques that have been developed to provide ways to determine astrophysical reaction rates for direct proton capture when the presence of the Coulomb barrier makes it difficult to measure the rate directly at astrophysical energies in the laboratory [20].

For $a(b + c) + A \rightarrow b + B(A + c)$, the nuclear structure of the reaction is contained in the overlap between the bound state wave functions $< \psi_a | \psi_b \psi_c >$ and $< \psi_B | \psi_A \psi_c >$ in the transfer reaction. These overlaps are defined by a factor called the spectroscopic factor $\mathcal{SF}$, which is a measure of the probability for the nucleus B with ψ_B to be made up of the nucleon c with specific quantum numbers ℓ, j relative to the nucleus A with ψ_A. This is expressed as the square of the norm of the overlap function [21], as shown in Eq. (2.65).

$$SF_{l_B j_B J_B} = \int_0^\infty dr_{Ac} r_{Ac}^2 \left[I^B_{A c l_B j_B J_B}(r_{Ac}) \right]^2 . \quad (2.65)$$

Direct radioactive capture reactions in astrophysical environments involve systems where the binding energy of the captured particles is low. Hence, a direct capture takes place through the tail of the nuclear overlap function in the corresponding two-body channel. So, the reaction is peripheral. The shape of this tail is completely determined by the Coulomb interaction between the nuclei, thus the capture rate can be calculated accurately if the amplitude of the tail is known, which is given by the ANC. The ANC can be calculated from peripheral transfer reactions at energies above, near the Coulomb barrier or sub-Coulomb barrier, and can be used to determine peripheral radioactive capture reactions [22].

For the decomposition $\boldsymbol{B \rightarrow A + c}$, the overlap function [23] is given by

$$\boldsymbol{I^{B}_{Ac}(r_{Ac}) = \binom{A}{c}^{\frac{1}{2}} < \Phi_A(\xi_A)\Phi_c(\xi_c) \mid \Phi_B(\xi_A, \xi_c; r_{Ac}) >.} \tag{2.66}$$

Here $\boldsymbol{\Phi}$ stands for the wave function and $\binom{\boldsymbol{A}}{\boldsymbol{c}}$ is antisymmetrization factor, while $\boldsymbol{\xi}$ and $\boldsymbol{r}$ define the internal coordinates and the motion of center-of mass. The above equation can be written in terms of Clebsch-Gordan coefficients as

$$\begin{aligned}\boldsymbol{I^{B}_{Ac}(r_{Ac}) = \sum_{l_B m_{l_B} j_B m_{j_B}} < J_A M_A j_B m_{l_B} \mid J_B M_B > < J_c M_c j_B m_{l_B} \mid J_B m_{l_B} >} \\ \boldsymbol{i^{l_B}\, Y_{l_B m_{l_B}}(\hat{r}_{Ac}) I^{B}_{Ac l_B j_B J_B}(r_{Ac}).}\end{aligned} \tag{2.67}$$

The approximation of the overlap function to a single-particle wave function is often given by

$$\boldsymbol{I^{B}_{Ac l_B j_B J_B}(r_{Ac}) = SF^{\frac{1}{2}}_{l_B j_B J_B} \Phi_{l_B j_B J_B}.} \tag{2.68}$$

The $\mathcal{SF}$ is a model dependent quantity, thus it can differ from unity due to the dependency of contribution of an infinite number of channels coupled to the two-body channel $\boldsymbol{(Ac)_{l_B j_B J_B}}$. In the single-particle approach, the radial overlap function in Eq. (2.68) can be approximated by a single-particle overlap function [24]

$$\boldsymbol{I^{B}_{Ac l_B j_B J_B}(r_{Ac}) \approx I^{B(sp)}_{Ac n_B l_B j_B J_B}(r_{Ac}) = [SF^{(sp)}{}_{n_B l_B j_B J_B}]^{\frac{1}{2}} \Phi_{n_B l_B j_B J_B}(r_{Ac}).} \tag{2.69}$$

where $\boldsymbol{\Phi_{n_B l_B j_B J_B}(r_{Ac})}$ is the normalized single-particle radial wave function of the bound state $(\boldsymbol{Ac})$ used in DWBA to analyze the experimental data. The single-particle SF, $\boldsymbol{SF^{(sp)}_{n_B l_B j_B J_B}}$, and the SF, $\boldsymbol{SF_{l_B j_B J_B}}$, are identical if Eq. (2.68) and (2.69) are equivalent in both the nuclear interior and the exterior. However, for r<RAc where both the overlap function $\boldsymbol{I}$ and the single-particle wave function $\boldsymbol{\Phi}$ have most of their probability, the radial dependence of the overlap function may differ from that of the single-particle wave function because the overlap function is a many-body object, while the single-particle wave function is a solution of the single-particle Schrödinger equation. Hence, the single-particle SF and the microscopically calculated SF do not coincide. For r>RAc, on the other hand, the radial dependences of $\boldsymbol{\Phi_{n_B l_B j_B J_B}(r_{Ac})}$ and $\boldsymbol{I^B_{Ac l_B j_B J_B}(r_{Ac})}$ are the same, and they differ only in their overall normalizations, which is given by the ANC. The asymptotic behavior of the radial overlap function and the radial bound-state wave function are given by [21, 22]

$$\boldsymbol{I^B_{Ac l_B j_B J_B}(r_{Ac}) \rightarrow C^B_{Ac l_B j_B J_B} \frac{W_{-\eta_B, l_B+\frac{1}{2}}\left(2\kappa^B_{Ac} r_{Ac}\right)}{r_{Ac}}}, \tag{2.70}$$

and

$$\boldsymbol{\Phi_{n_B l_B j_B J_B}(r_{Ac}) \rightarrow b_{n_B l_B j_B J_B} \frac{W_{-\eta_B, l_B+\frac{1}{2}}\left(2\kappa^B_{Ac} r_{Ac}\right)}{r_{Ac}}}, \tag{2.71}$$

respectively. Here C is the ANC, while b is the single-particle ANC. $\boldsymbol{W_{-\eta_B, l_B+\frac{1}{2}}\left(2\kappa^B_{Ac} r_{Ac}\right)}$ is the Whittaker function describing the asymptotic behavior of two charged particles interacting by the Coulomb force, while $\boldsymbol{\kappa}$ is the bound-state wave number. Then, comparing Eq. (2.69), (2.70), and (2.71), we get the relation which connects the single-particle SF to the ANC, as shown in Eq. (2.72).

$$SF^{(sp)}{}_{n_B l_B j_B J_B} = \frac{\left(C^{B}_{Acl_B j_B J_B}\right)^2}{\left(b_{n_B l_B j_B J_B}\right)^2}. \tag{2.72}$$

Using Eq. (2.69), the reaction cross section can be parameterized in terms of the product of the SFs of the initial and final channels, and given by

$$\frac{d\sigma}{d\Omega} = \sum_{j_B j_a} SF^{(sp)}{}_{n_B l_B j_B J_B} SF^{(sp)}{}_{n_a l_a j_a J_a} \sigma^{DW}_{n_B l_B j_B J_B n_a l_a j_a J_a}. \tag{2.73}$$

where $\sigma^{DW}_{n_B l_B j_B J_B n_a l_a j_a J_a}$ is the reduced DWBA cross section. For peripheral reactions, taking into account Eq. (2.69) and (2.72), the DWBA cross section can be rewritten in the form [25, 26]

$$\frac{d\sigma}{d\Omega} = \sum_{j_B j_a} \left(C^{B}_{Acl_B j_B J_B}\right)^2 \left(C^{a}_{bcl_a j_a J_a}\right)^2 R_{l_B j_B J_B n_a l_a j_a J_a}. \tag{2.74}$$

where $R_{l_B j_B J_B n_a l_a j_a J_a} = \frac{\sigma^{DW}_{n_B l_B j_B J_B n_a l_a j_a J_a}}{\left(b_{n_B l_B j_B J_B}\right)^2 \left(b_{n_a l_a j_a J_a}\right)^2}$.

Eq. (2.73) implies $\sigma^{DW}_{n_B l_B j_B J_B n_a l_a j_a J_a} \propto \left(b_{n_B l_B j_B J_B}\right)^2 \left(b_{n_a l_a j_a J_a}\right)^2$ for peripheral reactions, so R is nearly independent of $b_{n_B l_B j_B J_B}$ and $b_{n_a l_a j_a J_a}$.

The ANC for ^{26}Si(p,γ)^{27}P from ^{13}C(^{26}Mg,^{27}Mg)^{12}C

The reaction ^{26}Si(p,γ)^{27}P plays a significant role in the destruction of the important astrophysical observable ^{26}Al. The Gamow windows of the reaction for several temperatures are shown in Figure 10. The reaction rate for ^{26}Si(p,γ)^{27}P has been estimated in [12] and [13] based on theoretical models. However, due to several difficulties, direct measurements of the reaction ^{26}Si(p,γ)^{27}P at stellar energies have not been reported yet. The major difficulties are that it is impossible to make ^{26}Si as a target due to its short lifetime ($t_{1/2}$=2.29 s), and it is difficult to obtain an intense ^{26}Si beam for the direct measurements in inverse kinematics.

In order to overcome these difficulties, it was proposed in [27] that the proton capture reaction ^{26}Si +p → ^{27}P can be studied by means of the neutron transfer reaction ^{26}Mg+n→^{27}Mg using the advantages of a stable beam and target.

To extract the value of $\boldsymbol{C^2_{s1}}(^{27}Mg)$, the peripheral transfer reactions ^{13}C(^{26}Mg,^{27}Mg)^{12}C, where the ^{26}Mg beam picks up a loosely bound neutron from the target ^{13}C, was used. From this reaction the ANC for ^{26}Mg + n → ^{27}Mg can be obtained from the relation shown in Eq. (2.75). The ANC for ^{13}C was previously measured by means of the ^{13}C(^{12}C,^{13}C)^{12}C in [28], which will be used for extract the ANC for ^{27}Mg. Once the ANC of the ground state in ^{27}Mg is extracted, it will be transposed to the relevant state of ^{27}P, which is used to determine the reaction rate for ^{26}Si(p,γ)^{27}P.

$$\frac{d\sigma}{d\Omega} = C^2_{p\frac{1}{2}}(^{13}C)\,C^2_{s\frac{1}{2}}(^{27}Mg)\,\frac{\sigma^{DWBA}_{\frac{1}{2}\frac{1}{2}}}{b^2_{p\frac{1}{2}}(^{13}C)\,b^2_{s\frac{1}{2}}(^{27}Mg)}. \qquad (2.75)$$

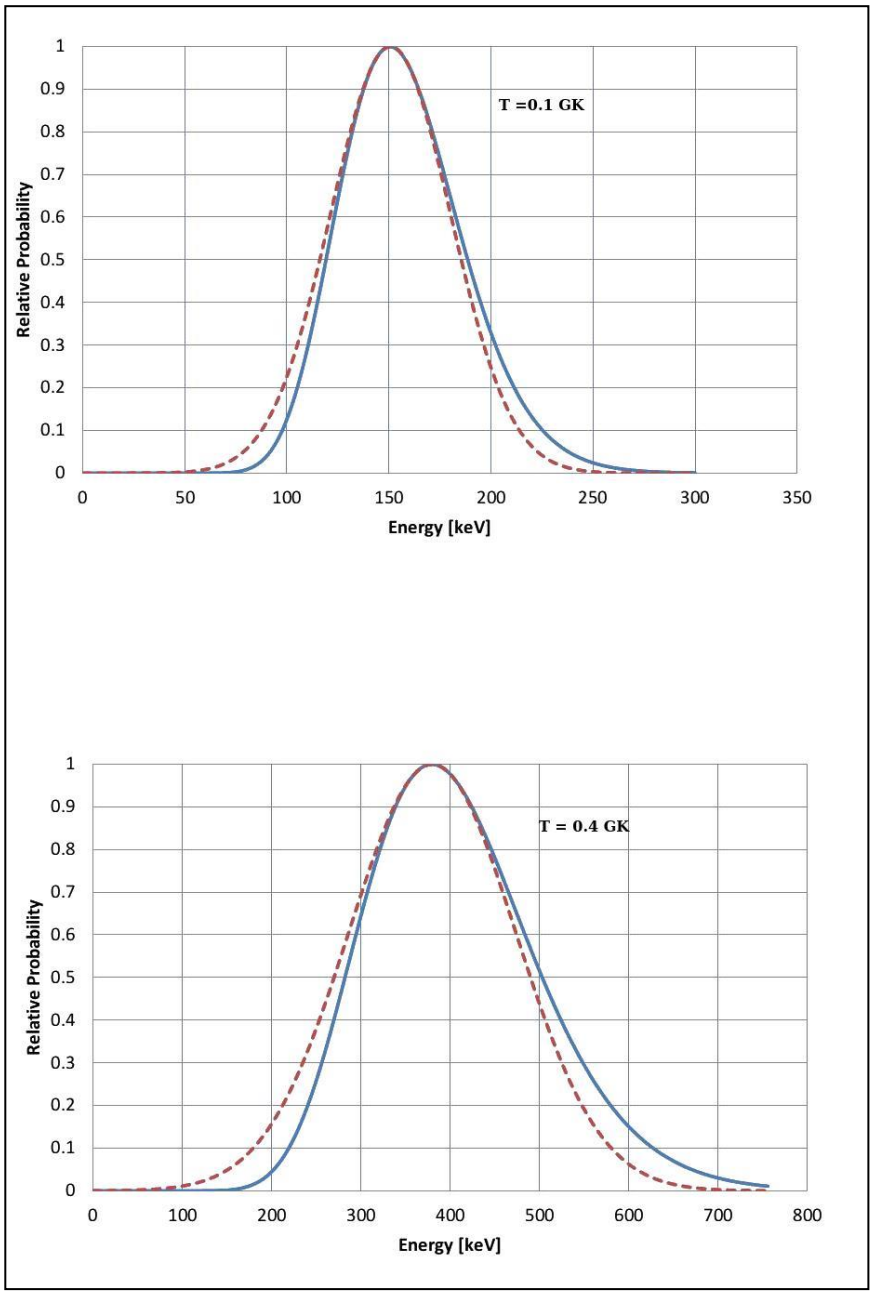

Figure 10: The Gamow peak for the ^{26}Si+p reaction at several stellar temperatures. The dashed line represents the Gaussian approximation, while solid lines represent the integrand of Eq. (2.32).

CHAPTER III

EXPERIMENTAL SETUP AND PROCEDURES

All experiments in this dissertation were conducted at the Texas A&M University Cyclotron Institute with beams accelerated from the K150 cyclotron facility, using the beam line as seen in Figure 11. Reaction products from the experiments were measured using the high-resolution multipole-dipole-multipole (MDM) spectrometer coupled with the Oxford detector.

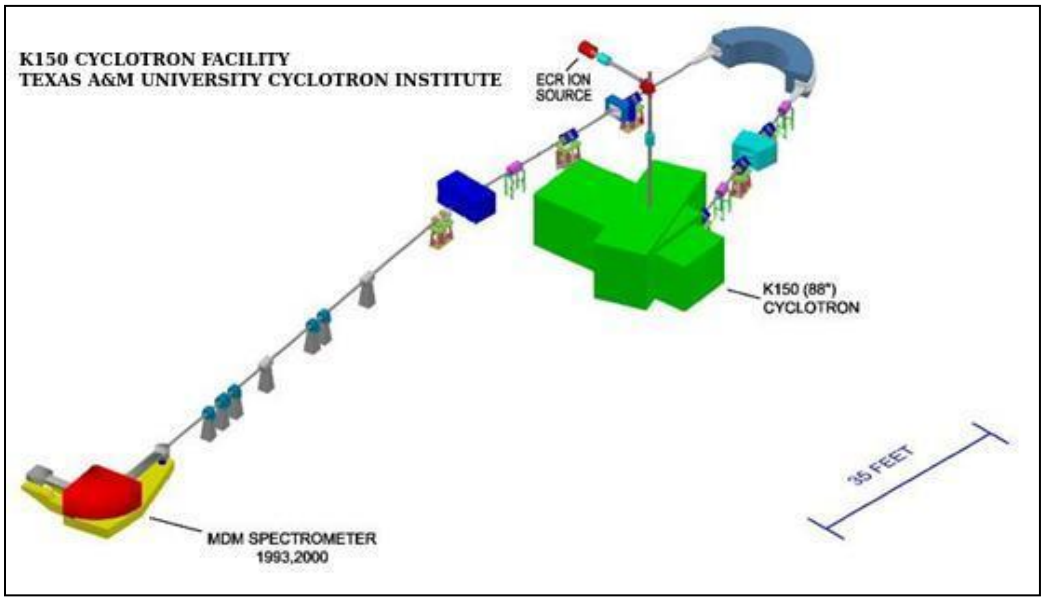

Figure 11: A diagram that illustrates the beam line used in the experiments with the K150 cyclotron.

The following conventions are used within this chapter: the axis along which the beam travels is determined as the z-axis, whereas the x- and the y-axes are defined as the horizontal axes perpendicular to the path of the beam and the vertical axis perpendicular to the beam path, respectively. The angle θ represents the angle in the x-z plane, while the angle ϕ is used for the angle in the y-z plane.

The MDM Spectrometer

After completion of the beam development process in the cyclotron, an accelerated beam is transported through the high-vacuum beamline, and reaches the target chamber of the MDM spectrometer. Inside the cylindrical target chamber, as seen in Figure 12, an aluminum target ladder with vertically positioned 5 circular slots is placed at the center point of the chamber on top of the remote-controlled base, so the target ladder can be remotely monitored, and vertically positioned from outside the sliding-seal target chamber.

Figure 12: The picture on the left shows the MDM spectrometer sitting on the rotatable platform. The center picture is the side view of the target chamber, while the top view of the target chamber is on the right.

The beam is perpendicularly aligned to the center position of the target, and impinges on a self-supporting thin foil target in the target chamber of the MDM spectrometer. Reaction products travel through the exit port of the chamber, where the Faraday Cup (FC), as shown in Figure 13, is mounted to measure the incoming beam charge for scattering angles larger than 4^{o}.

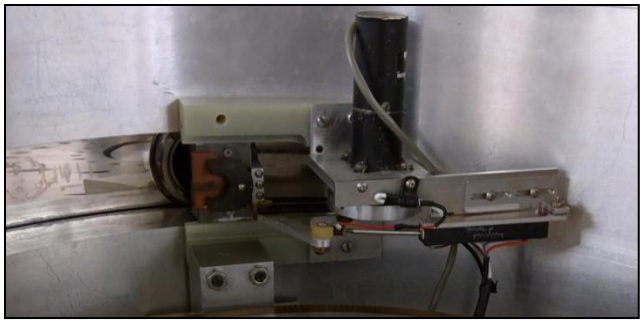

Figure 13: The Faraday Cup mounted inside the target chamber of the MDM spectrometer.

Downstream of the target chamber, reaction products pass through collimating slits inside the collimator box, a.k.a. "slit box". The collimator box contains 3 collimating slits made of brass, with different angular acceptances. These are the single slit (0.1^o θ and 1^o Φ), 5-finger (5 rectangular openings located at 0^o, $\mp$ 0.77^o, $\mp$ 1.53^o) and 4by1 (4^o acceptance in θ and 1^o in Φ), as shown in Figure 14.

Figure 14: The single slit mask is on the left, while 5- finger and 4by1 masks are on the center and right, respectively.

After the slit box, reaction products reach the MDM spectrometer, which is mounted on a rotatable platform, to be measured in a wide range of scattering angles. The MDM spectrometer was originally built and operated in the Nuclear Physics Laboratory, Oxford, UK. In the late 1990's, the spectrometer was relocated to the Texas A&M

University Cyclotron Institute, and has since then been used there. As detailed in Figure 15, it was designed based on a single dipole magnet to achieve large dispersion, low magnification and a high-energy product. A 100^{o} angle of deflection, 1.6 m central radius dipole magnet, with maximum field strength of over 1T was chosen to fulfill all criteria. The concave boundary at the exit of the dipole magnet also ensures the incident particles are normal to the focal plane [29].

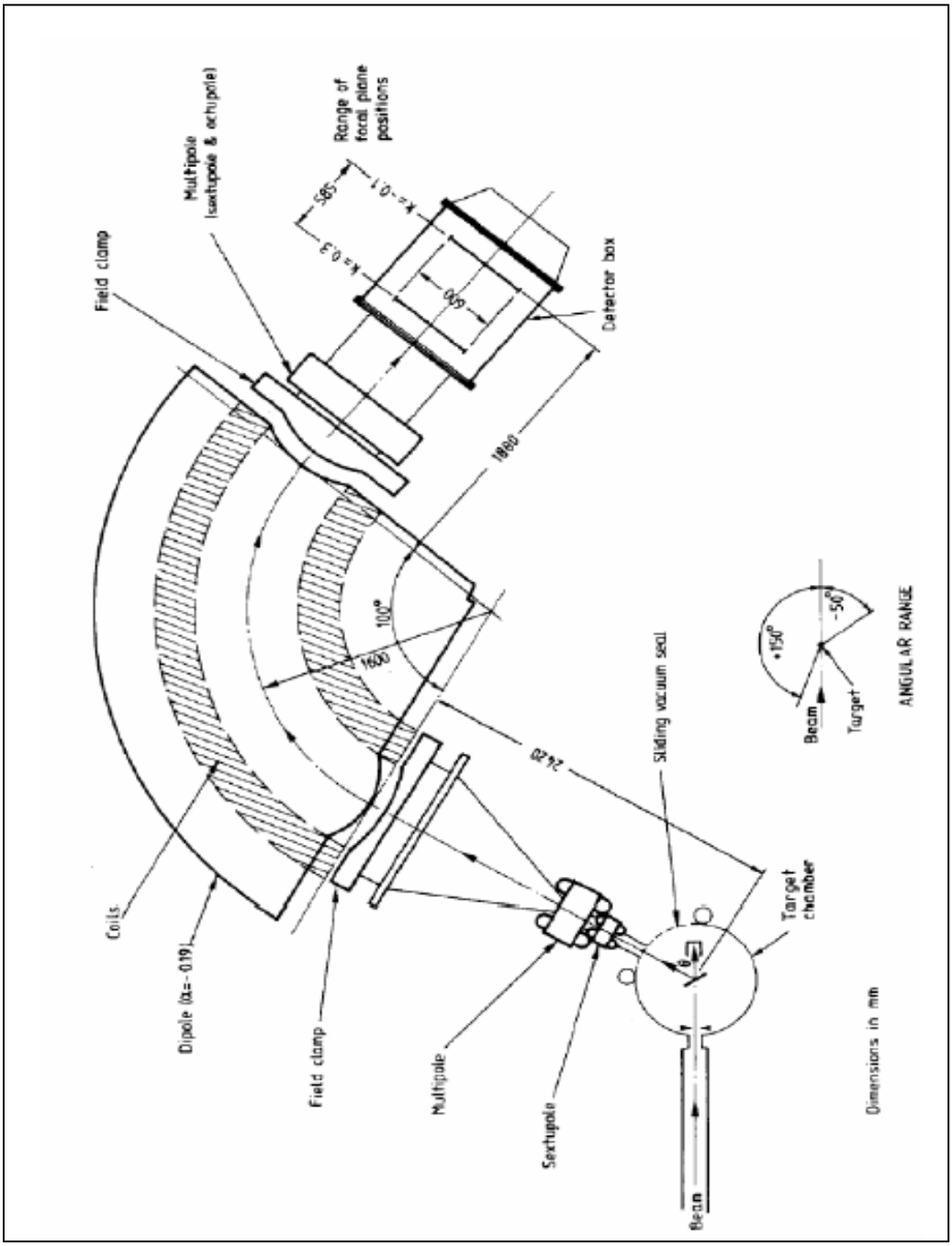

Figure 15: A diagram of the MDM spectrometer [21].

Oxford Detector and the Upgrade Process

Oxford Detector

One of the focal plane detection systems coupled with the MDM spectrometer is the Oxford detector, which is used to observe heavy ions. It is mounted at the back of the spectrometer for the purpose of measuring the energy and trajectory of scattered particles, as seen in Figure 16.

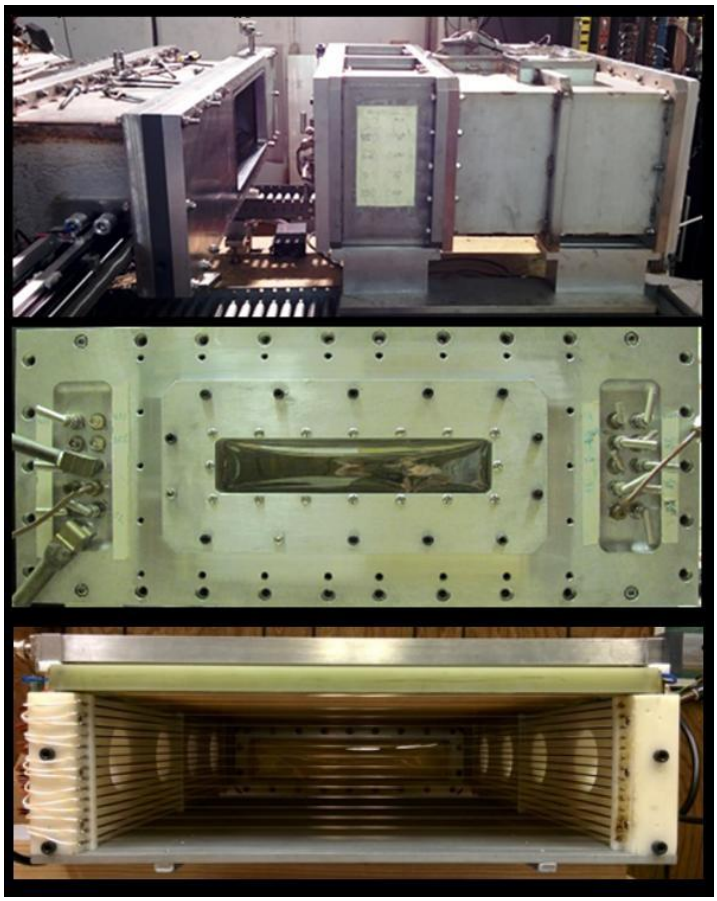

Figure 16: The figure at the top shows the Oxford detector before mounting at the back of the spectrometer. The center and bottom figures show the front and inside of the Oxford detector, respectively. All feedthroughs and the 25 μm thick Aramica foil can be seen from the picture on the center above.

The Oxford detector is an ionization chamber made of stainless steel, with entrance and exit windows covered by 25 and 50 μm thick Aramica foil [30], respectively. The inside of the chamber is filled with isobutane gas to typically no more than 150 Torr. In order to minimize any further impurities of the gas during the experiment, this gas is continuously refreshed at a constant rate by a low flow regulation system without affecting regulated gas pressure.

Before upgrading the detector, the inside structure of the detector consisted of a cathode plate, three anode plates to measure particle energy loss in isobutane gas, four resistive avalanche counters (AC) to determine the position of the particles in the focal plane as well as their deviation angles, a 6.35 mm thick scintillator (type BC-400) placed behind the exit window where the particles stop, and two photomultiplier tubes (Hamamatsu – Model Nr. H1949-50) positioned at each end to determine their residual energy.

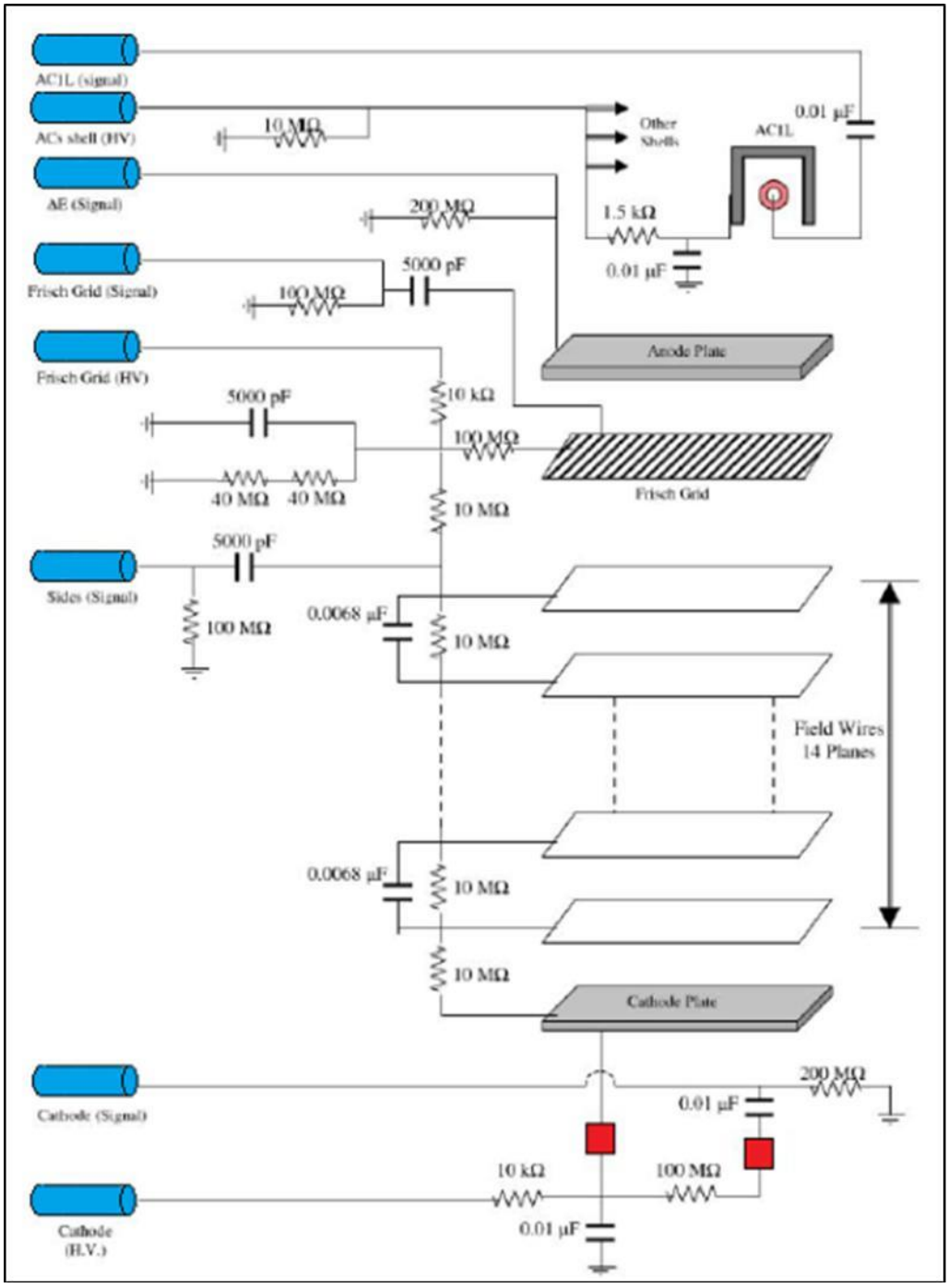

Figure 17: The internal electronic diagram of the Oxford detector.

The cathode plate is made of aluminum, and typically biased in the range between 800-1000 V. At 10.5 cm above the cathode plate, there is a multi-wire Frisch Grid (FG) as detailed in Figure 17. It consists of uniformly spaced Be-Cu wires with 80 μm diameter, fixed at a rectangular shaped frame of G10 glass fiber.[31] There are also 14 field shaping wires inside detector, vertically spaced with 7 mm wide gaps, running along the sides of the detector, to provide uniformity of the field in this region [32].

At the top of the Frisch Grid, four avalanche counters sit along the detector. The first AC is placed 2 cm behind the entrance window. The other ACs are placed 15.1 cm, 31.4 cm, 47.7 cm behind the first AC, respectively. A resistive avalanche counter (AC) consists of a 40 cm long rectangular aluminum shell, and a Ni-Cr alloy wire (StablOhm 675) with 12.7 μm diameter inside the shell.

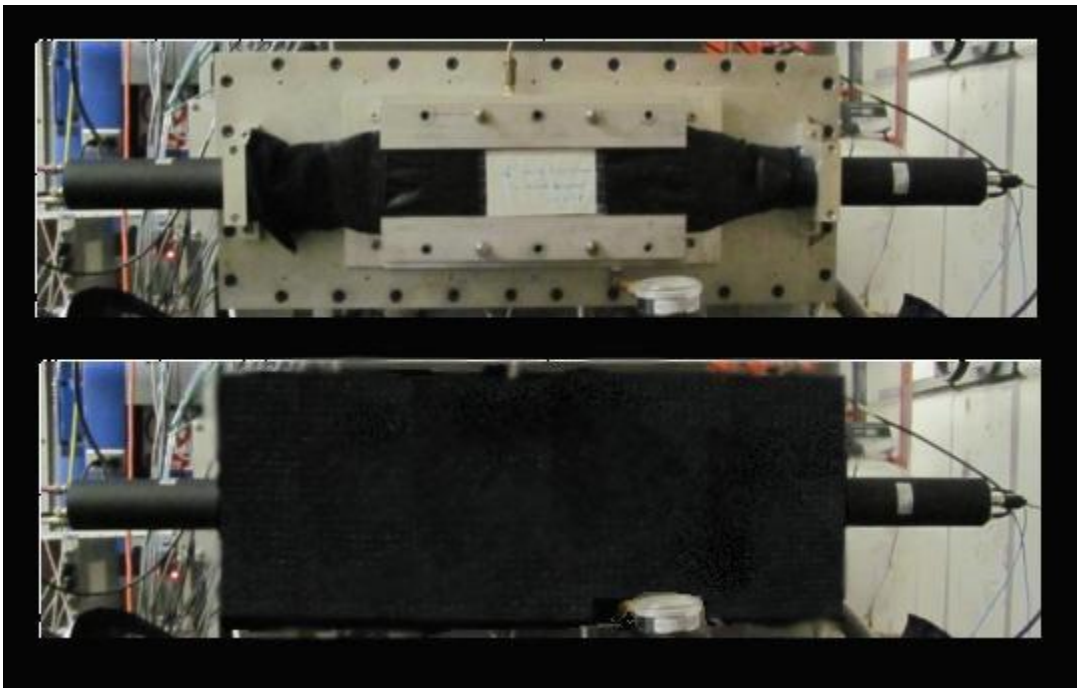

Figure 18: The figure at the top shows the back of the Oxford detector after the scintillator and PM were mounted, while the bottom illustrates it after being covered by a long thick black cloth to minimize possible light leaks.

Downstream of the exit window of the detector, after a 31.75 mm gap, a 6.35 mm thick BC-400 type plastic scintillator is attached to the frame of the back of the detector with two clamps, and a vacuum between two surfaces is secured with an O-ring. The light produced by particles stopping in the scintillator is collected with two Photomultiplier tubes (PM), which are placed on each side of the scintillator without using any optical grease or epoxy. By not using optical grease between PM and scintillator, the possibility of degradation of the light transmission due to imperfections in the mounting is minimized. The entire scintillator system then was covered by a long thick black cloth to reduce the possible light leaks, as shown in Figure 18.

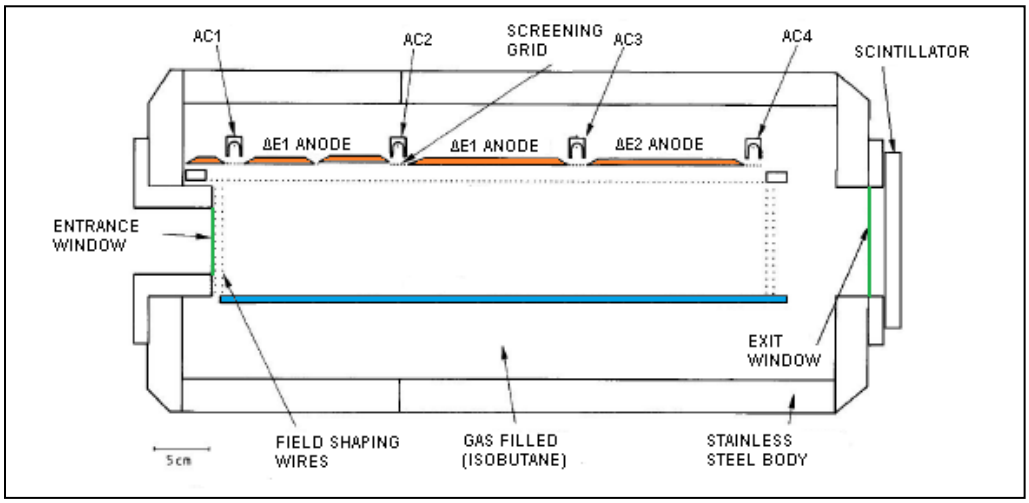

Figure 19: A drawing representing a cross section view of the conventional setup of the Oxford detector with its main internal parts.

Three aluminum anode plates placed 12 cm above the cathode plate were used to determine the differential energy loss of particles. The first two plates were connected and produced a signal called ΔE1, whereas the third plate gave a similar signal called ΔE2, as shown in Figure 19. However, since the signal obtained from ΔE2 was rather noisy, only ΔE1 was used to measure the particle energy loss in the detector.

The First Upgrade

The Oxford detector had been used with this setup to study scattering and transfer reactions involving beams up to Ne. However, when it was decided to study nuclear reactions with heavier ions, the energy resolutions obtained from the anode plates and the scintillator were poor for the particle identification (PID), especially at larger scattering angles where cross sections of interest drop.

The result of an experiment conducted with a beam of ^{26}Mg at 12 MeV/A at 30 Torr, for instance, found that the energy resolutions of ΔE1 and PM, respectively, were 10% and 16%, which was clearly not good enough for PID even at forward angles, as seen in Figure 20. Hence, in order to improve the particle identification resolution for the heavier particles, and increase the detection of both of these signals, it was proposed to upgrade of the Oxford detector by replacing the third plate with a Micromegas array.

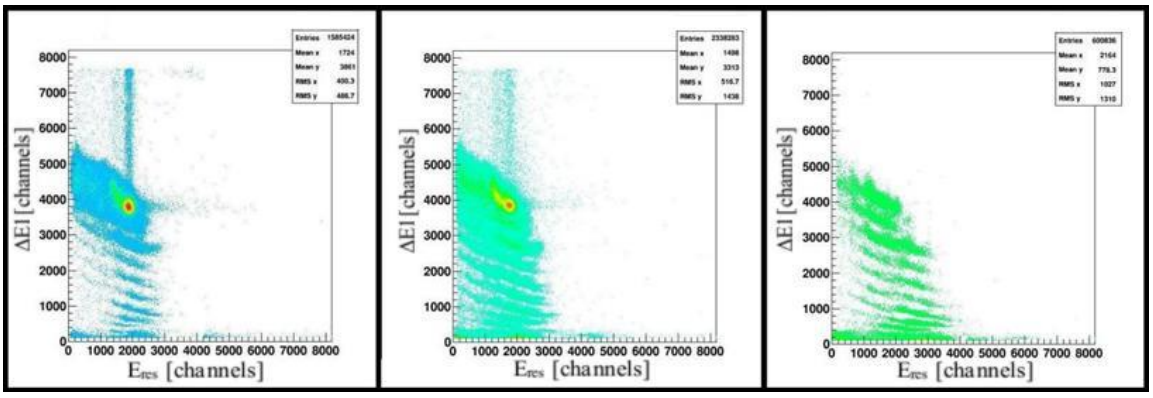

Figure 20: The three ΔE1-E_{res} spectra presented above were obtained from the experiment conducted with a beam of ^{26}Mg at 12 MeV/A impinging on a 100 μg/cm^2 self-supporting ^{13}C target at 4°, 6° and 9.1°, respectively. The x-axis on each spectrum represents the particle energy loss in the gas, detected by the first plate (ΔE1), while the y-axis is for the residual energy of the particle deposited in the scintillator.

The Micromegas (Micro-Mesh-Gaseous Structure) array, as illustrated in Figure 21, is a double-stage parallel plate chamber made of an anode pad, insulating spacers, a

micromesh and a drift electrode (cathode) [33]. A micromesh divides the gas volume into two parts, a small amplification gap on the order of microns and conversion-drift gap on the order of cm. In the drift gap, the charged particles ionize the gas atoms and generate pairs of positive ions and electrons. Due to the electric field in the drift zone, the electrons drift toward the micromesh and into the amplification zone, whereas the positive ions move toward the cathode. Since the electric field in the amplification zone is more intense compared to the drift zone, the electrons there produce more ion-electron pairs that will also create pairs (the avalanche effect). The electron cloud is collected by the anode pad, while the positive ions flow to the micromesh and are captured by it.

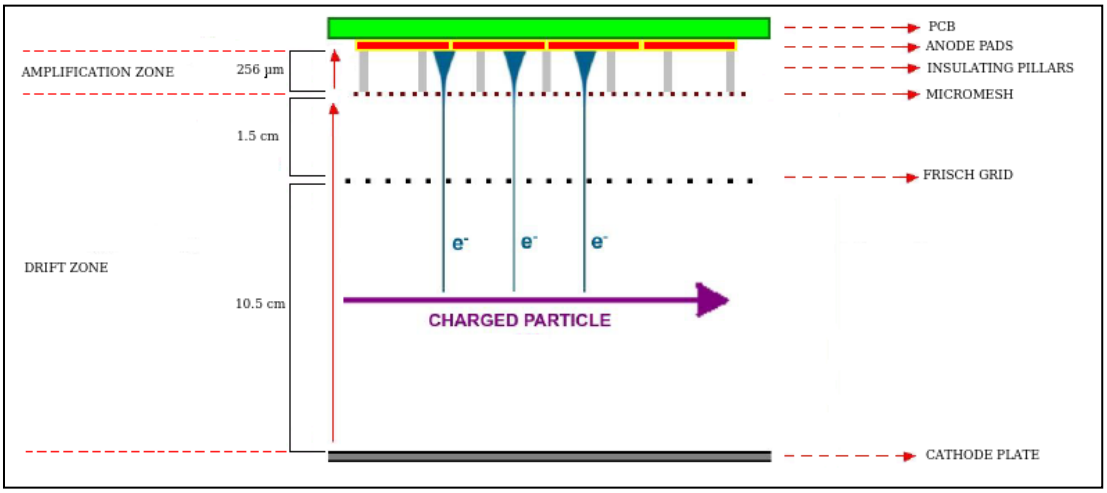

Figure 21: A diagram showing the cross section of the Micromegas array with its main internal parts along with the Oxford detector.

This micromesh structure has been tested with different gas mixtures at atmospheric pressure or higher such as [34]. But, since the Oxford detector needs to be used at low pressure (~30 Torr), it was challenging to combine this structure with the conventional setup of the Oxford detector. For this reason, the size of Micromegas array was chosen to be identical to the third anode plate dimensions, so all modifications could be done

without adversely affecting the existing setup in case of any conflict between the two systems.

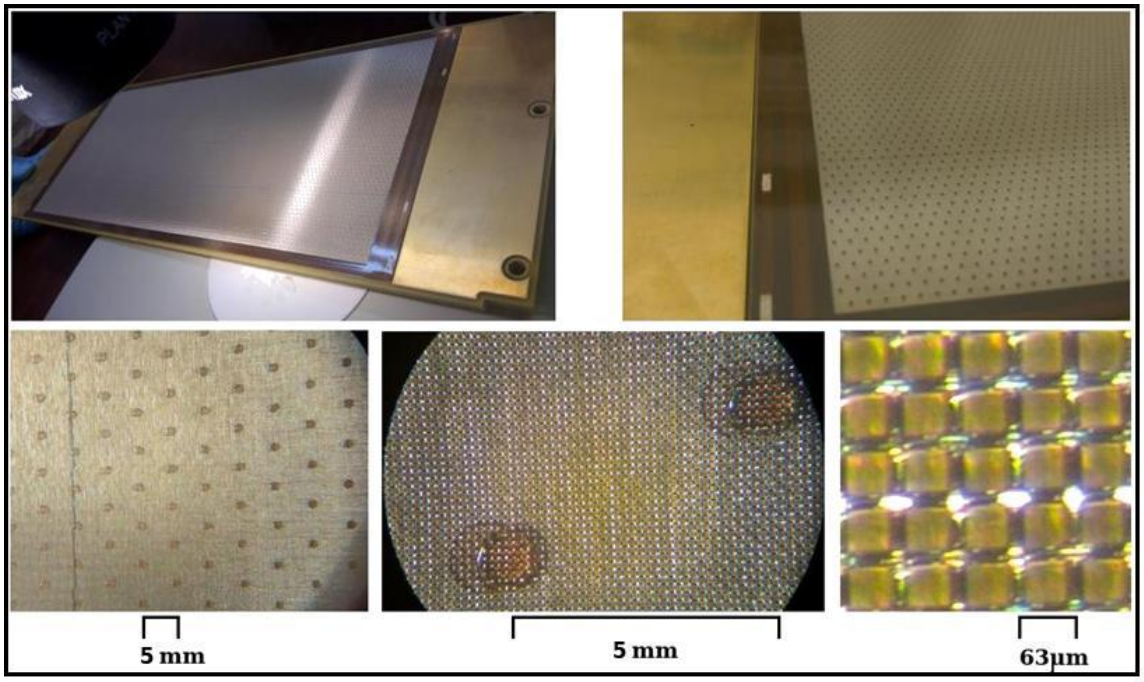

Figure 22: Pictures of the Micromegas captured under the microscope with different magnification settings. Insulating cylindrical shape pillars can be seen on the left and center pictures at the bottom with different focus settings. The bottom right picture shows the stainless-steel mesh.

For the Oxford detector upgrade, a new custom-made bulk type Micromegas, as in Figure 22, was developed that consists of a 6 mm thick multi-layered printed circuit board (PCB) with gold-plated copper for a uniform conducting surface. Insulating cylindrical shape spacers (pillars) that are 400 µm in diameter and printed with a distance of 5 mm on top of the anode plane are used as a supporting structure for the micromesh, which is a stainless-steel mesh made by stainless steel wires of 18 µm in diameter interwoven at a pitch of 63 µm.

There are 4 rows along the structure and each row hosts 7 pads, as seen in Figure 23. These 28 individual pads in total give 28 read-out signals. Each pad is 3.25 cm by 4.4 cm in in size, and the gap between pads is approximately 0.2 mm. The amplification gap

is 256 μm thick, which is larger than that of conventional Micromegas detectors having amplification gaps of 50-100 μm, in order to obtain a sufficient level of gas gain at low pressure [35].

Figure 23: The photographs at the top and bottom, respectively, show the front and back view of the Micromegas.

Once the Micromegas was inserted in place of the third anode plate (ΔE2), the upgraded Oxford detector system was tested with 3 beams: ^{16}O, ^{22}Ne, and ^{28}Si at about 12 MeV/A. For the test purpose, only elastic scattering on ^{197}Au at 4^{o} was performed at various gas pressures (30-100 Torr) with different anode voltages (190-290 V) [36]. The results showed that this structure works well with the Oxford detector at low pressure, without disturbing any other part of the detector. The energy resolution obtained from the Micromegas is, moreover, 3-5%, which is a quite good compared to the energy resolution previously obtained from ΔE1 (10%). This will be discussed in detail in A. Spiridon's thesis [36].

Since the test experiment was successful, we decided to repeat the experiment which was previously conducted to measure elastic scattering $^{13}C(^{26}Mg,^{26}Mg)^{13}C$ and the single-neutron transfer reaction $^{13}C(^{26}Mg,^{27}Mg)^{12}C$ (see Chapter IV for details). The experiment confirmed the test experiment result by indicating that the energy resolution of Micromegas was 5.6%, whereas the energy resolution for ΔE1 was 8%.

The Second Upgrade

Subsequently, $^{13}C(^{28}Si,^{28}Si)^{13}C$ and $^{13}C(^{32}S,^{32}S)^{13}C$ experiments were performed. However, the plastic scintillator at the back of the detector was insufficient at larger scattering angles ($\geq 10^{o}$) for particle identification where the particles have much less energy to lose in the scintillator compared to small forward angles.

Additionally, as demonstrated by the test experiment, lowering the gas pressure leads to a reduction of the energy resolution of the Micromegas. Hence, in order to have a better resolution for the Micromegas by increasing the gas gain, we decided to replace the second aluminum anode plate, as illustrated in Figure 24, with the second Micromegas array, which is identical to the first one, and used it for PID instead of the PM.

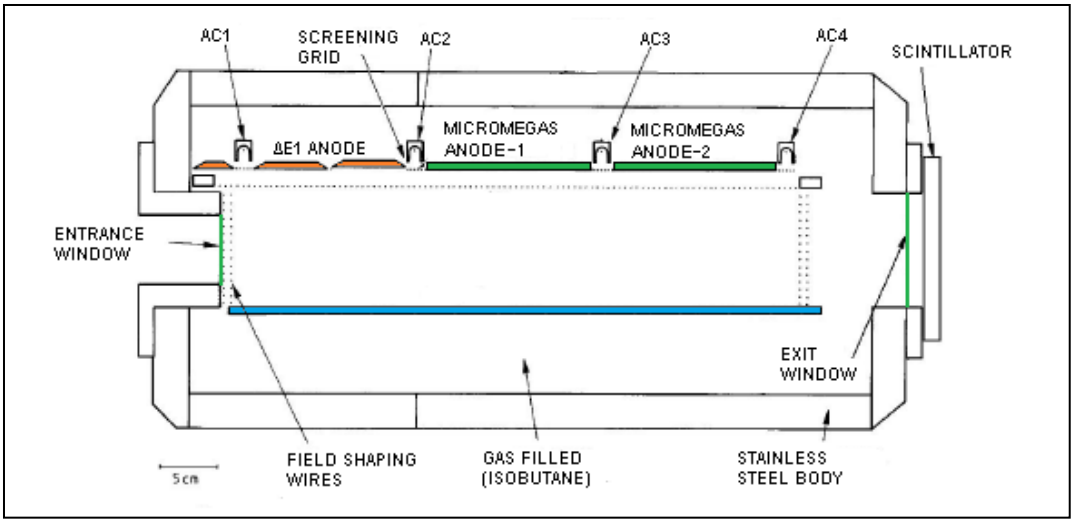

Figure 24: A drawing representing a cross sectional view of the setup of the Oxford detector with its main internal parts after the second upgrade was completed.

Prior to inserting the second Micromegas array in place of the anode plate, two new flanges were designed to bring the Micromegas signals out from the interior of the detector, each one includes a 6 mm thick PCB with two D-shaped connectors on each side, sealed with epoxy in case of any leaks, as in Figure 25. Thus, the 28 individual signals from each Micromegas (56 individual signals in total) are routed through the detector body by two kapton insulated ribbon cables (4 cables in total) in the flanges, as seen in Figure 26.

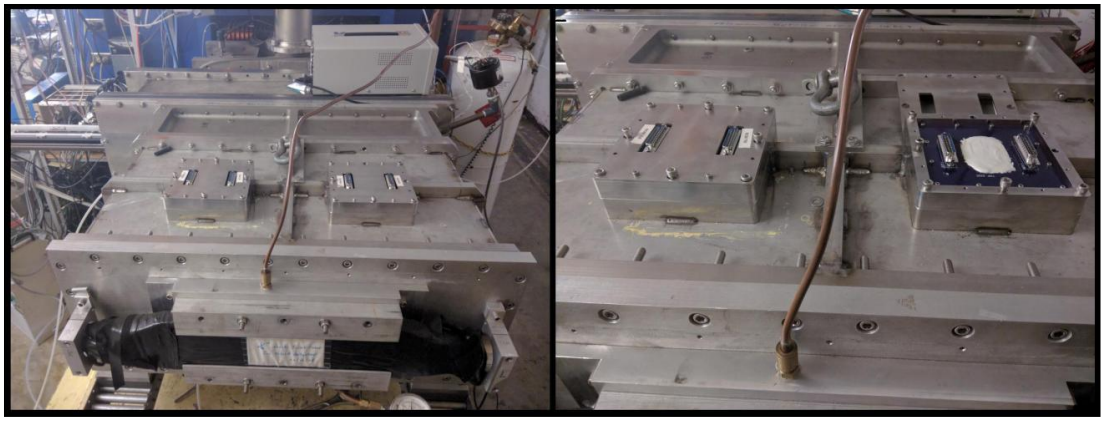

Figure 25: Both pictures showing the Oxford detector with the mounted flanges. As seen on the left picture, the flanges were sealed with epoxy in case of any leaks after completing the soldering process.

After the second Micromegas array was inserted, it was tested to determine whether it could be used in place of the scintillator. For this reason, by fixing the counts measured by the FC, we determined the number of counts on ΔE1, PM, and MM with the PM coincidence signal as a trigger. Following that, the same procedure was used with the Micromegas coincidence signal as the trigger. These two trigger systems are discussed below. The data from the Micromegas trigger were compared to that using the PM coincidence signal as a trigger. The comparison was made using elastic scattering of the ^{28}Si beam on the ^{13}C target at 4^{o} with the 4by1 slit. The number of counts detected with FC being fixed were recorded in ΔE1, PM, and MM histograms, and compared for both acquisition approaches. It showed that the number of the detected counts was increased 8% for ΔE1, ~5.89% for PM, and 5.19% for MM. Since the number of the counts detected by these two different acquisition approaches was essentially the same, we decided to use the Micromegas as the trigger while repeating both the ^{13}C(^{28}Si,^{28}Si)^{13}C and ^{13}C(^{32}S,^{32}S)^{13}C experiments (see Chapter 4 for details).

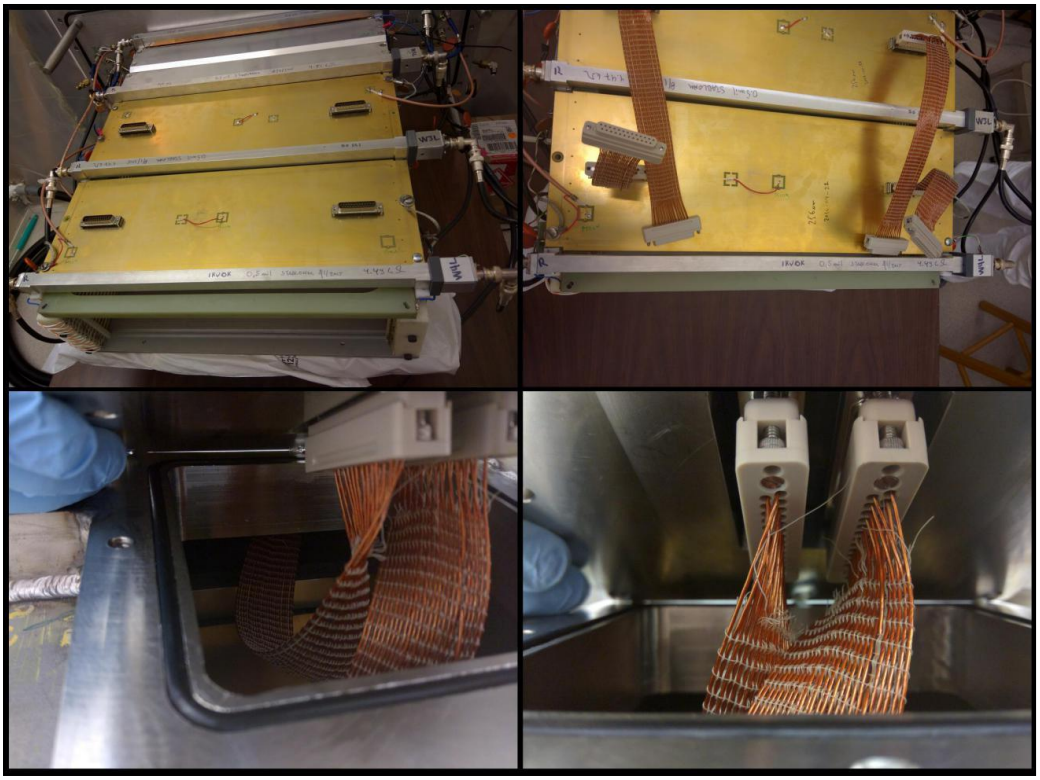

Figure 26: The photograph on the top left corner showing both Micromegas array in the detector. As seen in the picture on the top right corner, four kapton insulated ribbon cables were connected to the Micromegas arrays. The photographs on the bottom show the cables connected to the connector at the bottom of the flanges.

The Data Acquisition (DAQ) System and Procedures

The data acquisition was set to monitor and record 39 signals from the Oxford detector in total: 8 signals from the each end of the four ACs, 28 signals for the Micromegas placed between AC3 and AC4, one signal for the first anode plate (ΔE1), and two signals from PM anode outputs.

The signal obtained from each end of the AC was connected to a preamplifier (Canberra 2004) using a short SHV (Safe high voltage) coaxial cable to minimize noise, and then transmitted to a 16 channel spectroscopy amplifier (CAEN N568B) with a BNC (Bayonet Neill-Concelman) coaxial cable. The output signals from the amplifier were then sent to the first bank of the first ADC (Analog-to-Digital Converter) (Mesytec MADC-32) module with a 16-way rainbow ribbon cable. Only the right side of each AC wire was biased in the range of 800 V to 1 kV through the preamplifier, and the voltage was optimized depending on the particles, their energies and gas pressure in order to get the best possible position and angle resolution.

Four signals from PM (2 dynode output signals used for data, 2 anode signals for PM coincidence) were obtained. Two dynode output signals, after a delay of 600 ns to have the signals inside the ADC gate, were sent to a summing amplifier. Following the summing amplifier, the signals were transferred to the second 16 channel spectroscopy amplifier (CAEN N568B) along with the signal (ΔE1) from the first anode plate after being amplified by a preamplifier. All three output signals (PM-Left, PM-Right, ΔE1) were sent to the second bank of the first ADC module.

For each Micromegas, there are two 25-pin D-shaped connectors soldered at the back, as seen in the top left picture in Figure 3-16. Each connector was linked to two rows (corresponding to 14 pads). Each group of 14 pads were amplified with a preamplifier (Mesytec MPR16) at first, and then sent to a 16 channel shaping amplifier with CFD (Constant Fraction Discriminator) (Mesytec MSCF-16) with a round, shielded flat cable.

Afterwards, the output signals from both amplifiers were connected to the second ADC module.

Due to the fast response time, the PM coincidence signal was used as the DAQ system trigger for some of the experiments. The two anode signals from PM were optimized with a constant fraction discriminator (CFD) by accepting only signals above threshold, and were forwarded to a coincidence module (Philips scientific Model 754). On the coincidence module, one output was used for a Gate Generator (Ortec 8010) module to generate the gate for both ADC modules (one ADC for the Micromegas, the other for wires, ΔE1 and PM). The trigger and veto (dead time) outputs from the coincidence module were connected to a processor module (Wiener VM-USB) in VME crate.

A multi-channel scaler (SIS3801 VME multi scaler) was also used to measure counting rates for PM coincidence (ungated events), trigger (gated events), PM-Left and PM-Right, MSCF-16 Trigger Out Left and Right. Additionally, the signal coming from FC was measured with a Current Integrator (TAMVEC, Model 1000c), while total beam charge was read by a counter (Ortec Dual Counter 995).

This DAQ system was used as described above for the elastic scattering $^{13}C(^{26}Mg,^{26}Mg)^{13}C$ and single-neutron transfer reaction $^{13}C(^{26}Mg,^{27}Mg)^{12}C$ measurements. However, because the Oxford detector was upgraded with the second Micromegas array for both $^{13}C(^{28}Si,^{28}Si)^{13}C$ and $^{13}C(^{32}S,^{32}S)^{13}C$ experiment, a Mesytec MADC-32, and pair of both Mesytec MPR16 and Mesytec MSCF-16 were acquired for the second Micromegas.

The connection for the second Micromegas was repeated as it was done for the first Micromegas, as seen in Figure 27. Each group of 14 pads for the second MM was amplified with Mesytec MPR16 at first, and then Mesytec MSCF-16. The output signals from both amplifiers (Mesytec MSCF-16) were afterwards sent to the third ADC module.

Since the Micromegas coincidence signal was used as a trigger instead of the PM coincidence signal, the PM anode signals were removed from the coincidence unit, and the trigger outputs from all 4 MSCF-16 were put into a Philips coincidence module. Since the scintillator response time is faster than the Micromegas, the PM dynode signals were delayed 2 μs between the summing amplifier and amplifier (CAEN N568B) to make sure that the signals were properly in time relative to the computer gate.

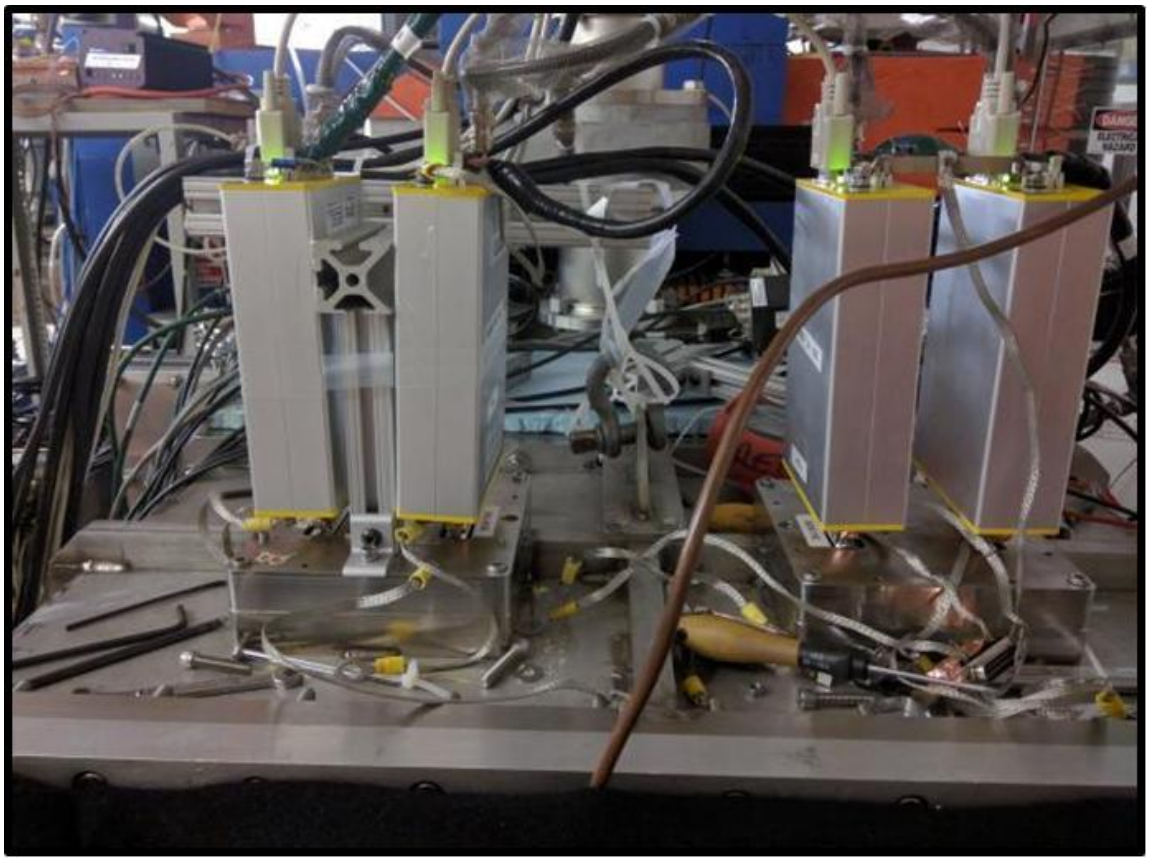

Figure 27: The photographs showing all four preamplifiers mounted on the flanges.

CHAPTER IV

DATA ANALYSIS

Pre-Analysis Procedures

Previous to starting data analysis, there are a certain number of processes that need to be performed during and after the experiment such as gain-matching for wires and the Micromegas pads, and position and angle calibrations. In this subsection, these processes will be discussed.

After the DAQ system was setup, the MDM spectrometer was set at 4^{o} lab angle. Then, the ^{197}Au target and the single slit were selected. The position of the moveable FC was optimized by monitoring with the Current Integrator, and it was left where the beam current was at the highest level. Then voltage was applied to the cathode plate (800-1000 V), ACs shell (100 V), PM (negative 1600-1750 V), ACs (800-1000 V) and Micromegas (250-400 V).

Subsequently, by adjusting the voltages applied to each AC wire, the best possible position (on the POS histogram) resolution was obtained for all four ACs. The position in the POS histogram for each AC wire was determined with the charge division method:

$$\boldsymbol{POS}_{[i]} = \boldsymbol{NC} \times \left(\boldsymbol{W}_{\boldsymbol{l}_{[i]}} / \left(\boldsymbol{W}_{\boldsymbol{l}_{[i]}} + \boldsymbol{W}_{\boldsymbol{r}_{[i]}}\right)\right) \qquad \text{i=1-4} \qquad (4.1)$$

where NC is the number of channels in the histogram, W_l and Wr are the numbers corresponding to the digitized ADC signal from the left and right of each ACs, respectively.

After obtaining the best position and angle resolution for all four ACs, the cathode voltage was adjusted to improve the resolution of ΔE1 signal, and then the PM voltages

were optimized until the resolution of PM-Left, PM-Right, and PM(Total) signals were favorable. The PM(total) signal was obtained taking the square root of product of the PM-Left and PM-Right signals.

Gain Matching for Wires and Micromegas Pads

The next process was the gain-matching for wires. To gain-match all 4 wires separately, a pulse generator was connected to a T-type connector through a 25 pF charge converter. One leg of the T-type connector was attached to the detector input of the preamplifier, while the other leg was connected to one end of the AC wire. Then, the output signal position was determined using the DAQ monitoring system. This was repeated for the other end of the same AC wire, and both output signals obtained from each end of the AC wire were matched by adjusting the gain in the CAEN amplifier.

The next process was to gradually increase the high voltage applied to the Micromegas anode, starting from the point that the MM signal appeared in the Micromegas Pad histogram up to the point that the MM signal overflowed. The voltage was then set to provide the best resolution signal for the Micromegas. In the $^{13}C(^{28}Si,^{28}Si)^{13}C$ and $^{13}C(^{32}S,^{32}S)^{13}C$ experiments, this process was performed for both Micromegas arrays individually.

With the detector set up, the next step was to sweep the scattered beam across the Oxford detector by adjusting the dipole magnetic field of the MDM spectrometer. The first thing was to find the edges of the Oxford detector (i.e. the acceptance limits of the detector), and thus the center. In the conventional setup of the Oxford detector, this process was done by means of PM. Yet, it was a tricky method due to possibly seeing another charge state of the beam, as seen on Figure 28.

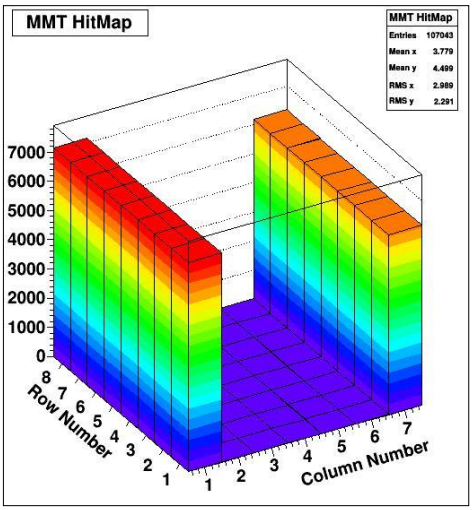

Figure 28: A hit map is showing the beams passing through the both Micromegas pads while magnetic field of the MDM spectrometer is 6207.5±0.5 G. The fully-stripped ^{28}Si beam can be seen on the first column, while the next charge state ($^{28}Si^{+13}$) is on the 7th column.

After the upgrade, the Micromegas was used for that instead of PM. Since the Micromegas array nicely covers the detection area along the x-axis, the edges of the central column (column 4) were found, and thus the center of the detector was calculated. Then, using the reaction kinematics and magnetic rigidity of the MDM spectrometer, the beam energy was determined. Once the central column was found, the collimated beam was sent through each column, and the collected data for each column was individually saved to later use for gain-matching for the Micromegas pads, as seen in Figure 29.

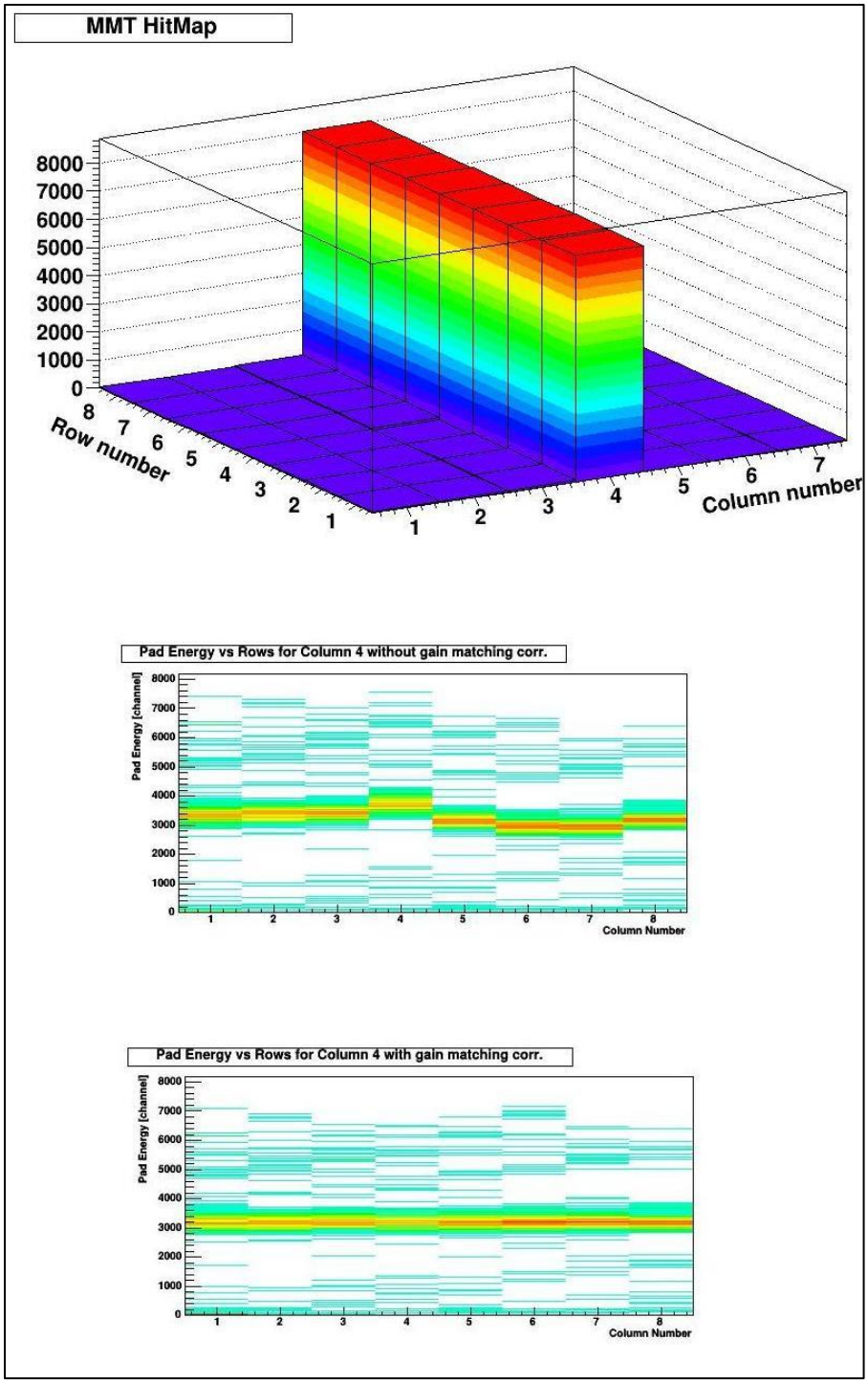

Figure 29: The picture at the top shows a hit map, where the ^{32}S beam scattered on the gold target at 4^{o} is passing through both Micromegas pads at Column 4. The center and bottom picture represents the Micromegas Pad Energy per Row prior to the gain matching and after the gain matching, respectively.

Position Calibration

Following the anode sweep, the position calibration was performed to determine the path of particles along the x-axis in the focal plane. For this purpose, the 5-finger mask was selected, while still ^{197}Au was the target and the MDM spectrometer was at 4^{o}. Since the center and the edges of the detector were already determined, the beam was sent through the 5-finger mask into the detector at five different magnetic rigidities in such a way as to cover the full detection area along the x-axis. Figure 30 below shows the raw signals from the left and right ends of the first AC wire in addition to the determination of the position signal for the first AC calculated using Eq. (4.1).

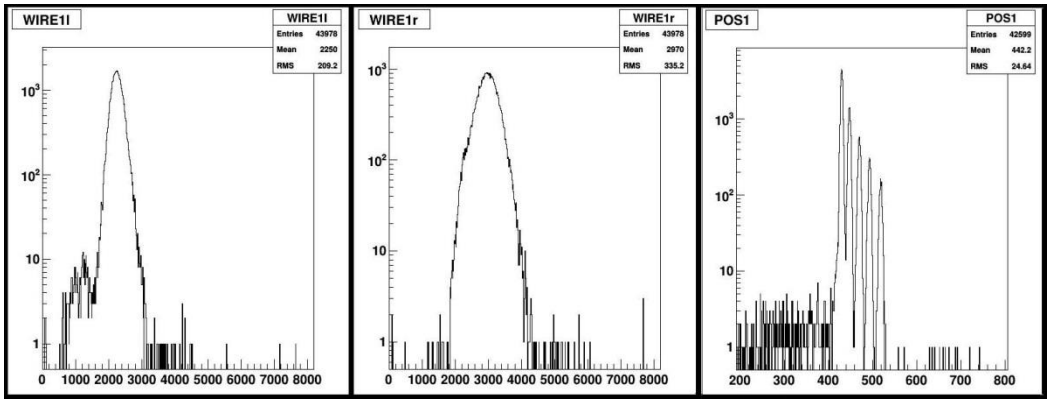

Figure 30: The left and center pictures show the raw signals obtained from the left and right ends of the first wire after ^{26}Mg ions from elastic scattering on at gold target at 4^{o}, pass through the 5-finger slit. The right picture illustrates the position signals obtained using Eq. 4.1, where the five trajectories can be seen clearly.

Along with the measurement, the corresponding positions on each of the four wires were calculated by means of the code RAYTRACE. RAYTRACE [37] is a computer code which can be used to determine the track of the particles beginning from the exit of the target chamber through the MDM spectrometer, taking into account the effect of all components located along the path. The output gives the positions and angles of the particles on the first wire. By using the five calculated trajectories for the particles that

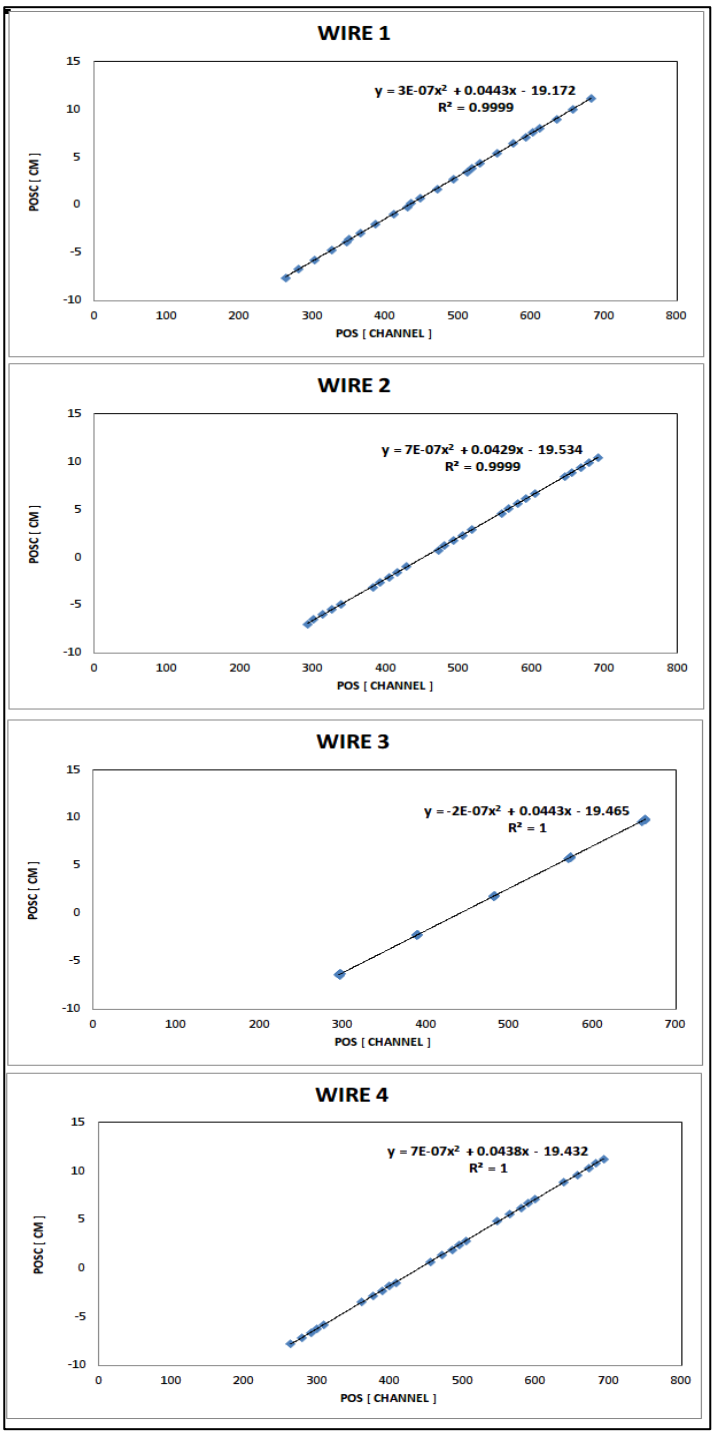

Figure 31: The position calibration for the ^{26}Mg beam scattered on the gold target at 4^{o} is shown along with the calculated correlation between the POS and the POSC.

passed through the 5-finger mask, their positions and angles on the first wire, the positions of the particles on the other wires were calculated. For each wire, the calculated positions (POSC) in cm were correlated to the observed channel number (POS) using a second-order polynomial as shown on Figure 31.

Angle Calibration

The angle of the particles in the detector, θ_d, was determined by means of their positions in any two of the four wires. In order to get the scattering angle at the target, θ_t, RAYTRACE calculations were performed for several beam energies using the same dipole magnetic field. For each beam energy, θ_t was obtained as a function of θ_d by

$$\boldsymbol{\theta_t = A + B\theta_d + C\theta_d^2}. \tag{4.2}$$

Since changing the beam energy will change the position of the particles in the focal plane (POSFP), the coefficients A, B and C were plotted as a second-order polynomial functions of the focal plane position, thus the relationship between the A, B, and C coefficients and POSFP was found to be described by the following equations.

$$\boldsymbol{A = A_1 + A_2 POSFP + A_3 POSFP^2} \tag{4.3}$$

$$\boldsymbol{B = B_1 + B_2 POSFP + B_3 POSFP^2} \tag{4.4}$$

$$\boldsymbol{C = C_1 + C_2 POSFP + C_3 POSFP^2} \tag{4.5}$$

where A1,A2,...,C3 are the final calibration parameters for the data analysis, and this process was repeated for every MDM angle and each outgoing particle. The angle calibration shown on Figure 32, for instance, was calculated for the elastic scattering of a ^{26}Mg beam on the ^{13}C target at 4^{o}.

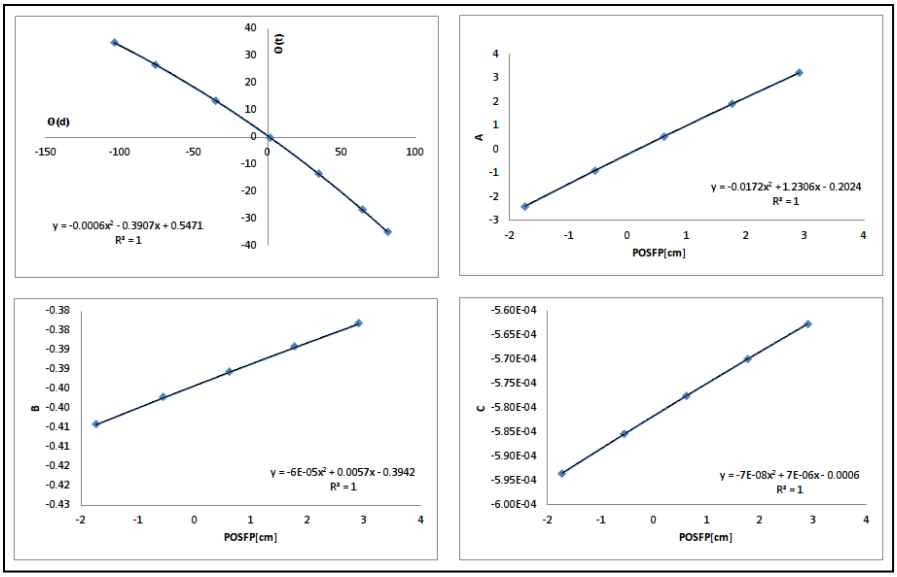

Figure 32: The figure shows the calculated angle calibration for the elastic scattering of ^{26}Mg on ^{13}C at 4^{o}.

Target Thickness Measurement

Measurements of the thickness of the thin ^{13}C target was performed online with all three beams (^{26}Mg, ^{28}Si, ^{32}S) using a double target method. First, only the gold target was placed on the target ladder, and bombarded with a beam with the MDM spectrometer at 4^{o}. The position of the elastic scattering along the dispersive x-axis in the focal plane of the detector was determined, and then ^{13}C target was placed in front of the gold target while the spectrometer was still at 4^{o}. The new position of the elastic scattering peak was measured and the shift in the position was used to calculate the energy loss of the beam in the target by means of RAYTRACE. Using the LISE code [38], the thickness of the ^{13}C was found to be 99± 6 μg/cm^{2}.

The $^{13}C(^{26}Mg,^{27}Mg)^{12}C$ Experiment

The reaction $^{13}C(^{26}Mg,^{27}Mg)^{12}C$ was measured to determine the ANC for the ground state in ^{27}Mg. The result was used to obtain the ANC of the corresponding states in its mirror nucleus ^{27}P. For this reason, an 11.86 MeV/nucleon ^{26}Mg beam was used on a ^{13}C target to measure the reaction cross section. Reaction products were measured at several spectrometer angles, allowing overlap for consistency checks of the data, using the MDM spectrometer and the Oxford detector after the first upgrade.

The Elastic Scattering Data

The elastic scattering angular distribution was measured at various spectrometer angles in the range 2^o–16^o in the lab frame. As an initial step for analysis, the scattered ^{26}Mg particles were gated on the $E_{residual}$ vs Micromegas histogram, as shown in Figure 33. The selected polygon gate from the MM vs $E_{residual}$ histogram was plotted on the Micromegas vs POSFP histogram for an additional constraint to avoid the possible impurities.

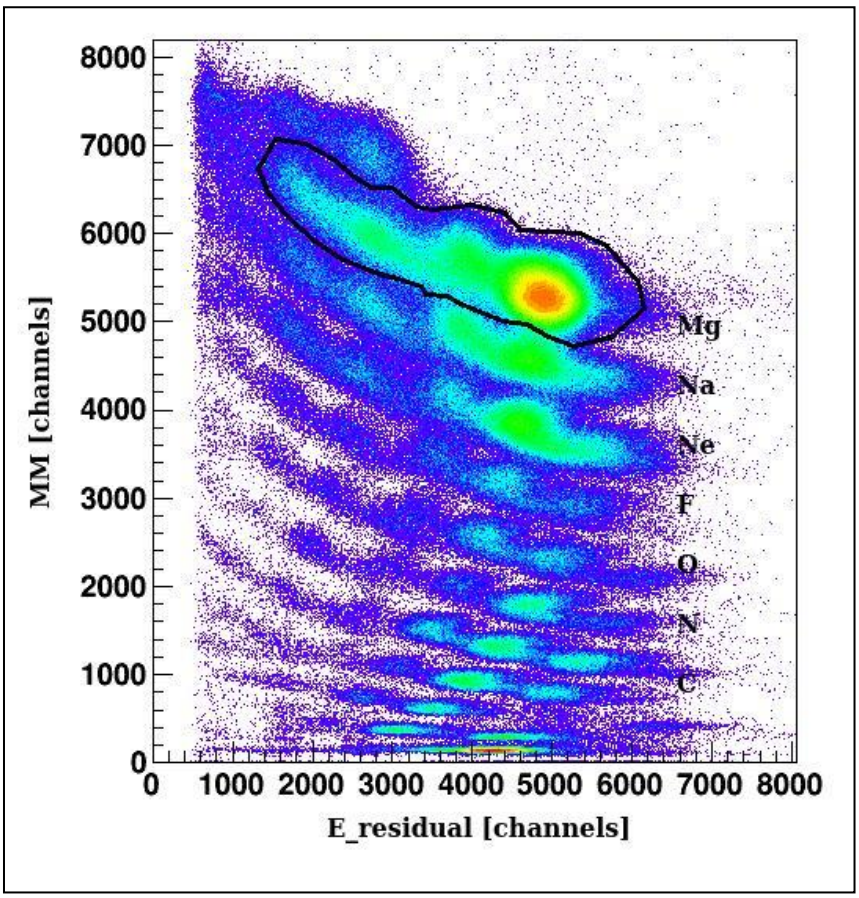

Figure 33: MM-$E_{residual}$ spectra presented above were obtained from the experiment conducted with a beam of ^{26}Mg at 11.86 MeV/A impinging on a 100 µg/cm^2 self-supporting ^{13}C target at 7^o. The y-axis on each spectrum represents the particle energy loss in the gas, detected by the Micromegas Array, while the x-axis is for the residual energy of the particle deposited in the scintillator.

Then the selected data was plotted on the TargetAngle vs POSFP, as seen in Figure 34. The position of the focal plane and the angle calibration were set for the elastic scattering using RAYTRACE. Based on the RAYTRACE calculation, the position of the elastic scattering ($J^{\pi}=0^{+}$), the inelastic scattering of the first excited state ($J^{\pi}=2^{+}$, 1.809 MeV) of ^{26}Mg as well as the scattering on the heavier impurities (Fe, Al and O) along the dispersive x-axis in the focal plane of the Oxford detector were determined. Then another polygon gate was placed around the elastic scattering, and projected onto the target angle axis, and divided into 16 bins 0.25^o in width.

The differential cross sections is determined by

$$\frac{\mathbf{d\sigma}}{\mathbf{d\Omega}}(\boldsymbol{\theta}) = \frac{\boldsymbol{N_{detected}}}{\boldsymbol{N_{incident} N_t \Delta\Omega(\theta) C_{FC} C_{DT}}}, \tag{4.6}$$

where $N_{detected}$ represents the number of particles detected in solid angle $\Delta\Omega(\theta)$ at the scattered angle θ. $N_{incident}$ is the total number of the incident particles on the target, which is N_t atoms/cm^2 thick. C_{FC} is the Faraday cup normalization factor, whereas C_{DT} is the correction for the data acquisition system dead time. The total number of the incident particles on the target is determined by dividing the integrated charge by the charge of the beam (fully stripped in our case).

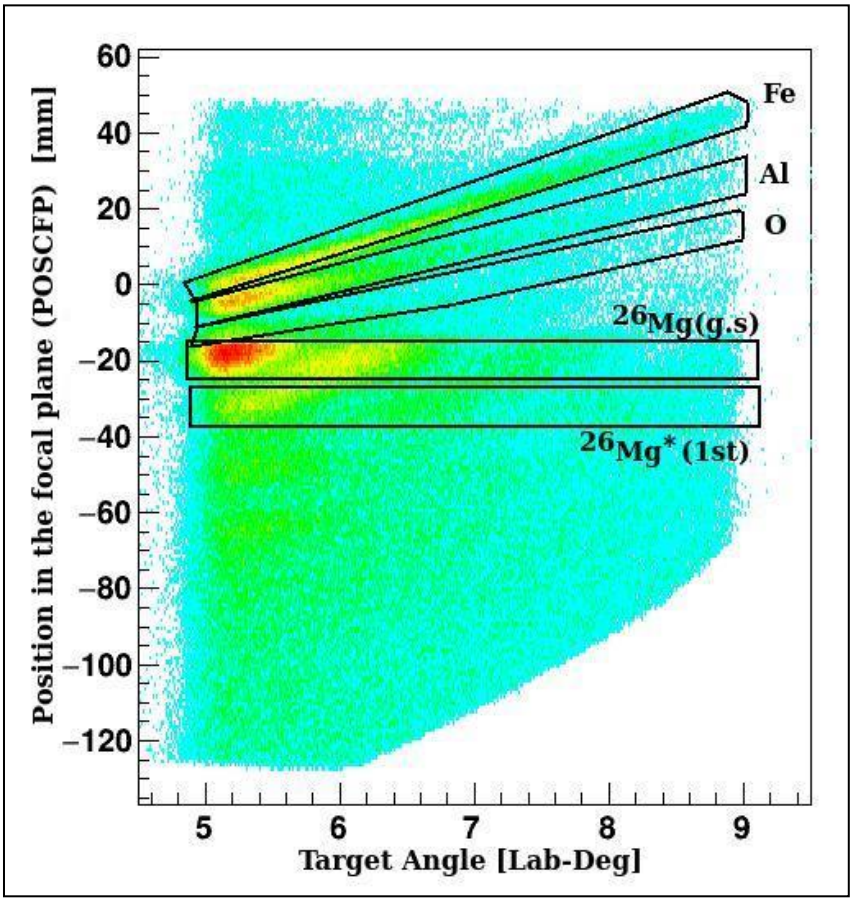

Figure 34: The POSCFP vs TargetAngle histogram for the $^{13}C(^{26}Mg,^{26}Mg)^{13}C$ reaction with the MDM at 4^o.

Normalization of the measured angular distribution was performed testing the efficiency of the Faraday cup. Using the single slit, the fully stripped ^{26}Mg beam impinge on a thin gold target at 4 degree to test the efficiency of the Faraday cup, and thus to get the correct normalization of the cross section values. The ^{26}Mg beam experiment required a Faraday cup normalization factor of 4%. The additional correction for the dead time of the data acquisition was also applied for each angle at which the MDM spectrometer is set. For example, a correction of 3% was applied for the measurement at 4^{o} in the lab frame.

Following gating and projecting the ground state on the target angle axis within the $\pm 2^{o}$ range for around 4^{o}, 7^{o}, 10^{o}, 14^{o}, and 16^{o} in lab frame, the elastic scattering angular distribution measurement of ^{26}Mg+^{13}C for the angular range 8^{o}-51^{o} in the C.M. frame was obtained.

Optical Model Fits

To obtain the optical potentials, which later were used for the transfer DWBA calculation, the data provided by the elastic scattering have been fit using the code PTOLEMY [39] in a standard optical model analysis with phenomenological Woods-Saxon form as presented in Eq. (2.61). However, spin-orbit couplings and imaginary surface terms were excluded in order to minimize complexity of the fitting procedure.

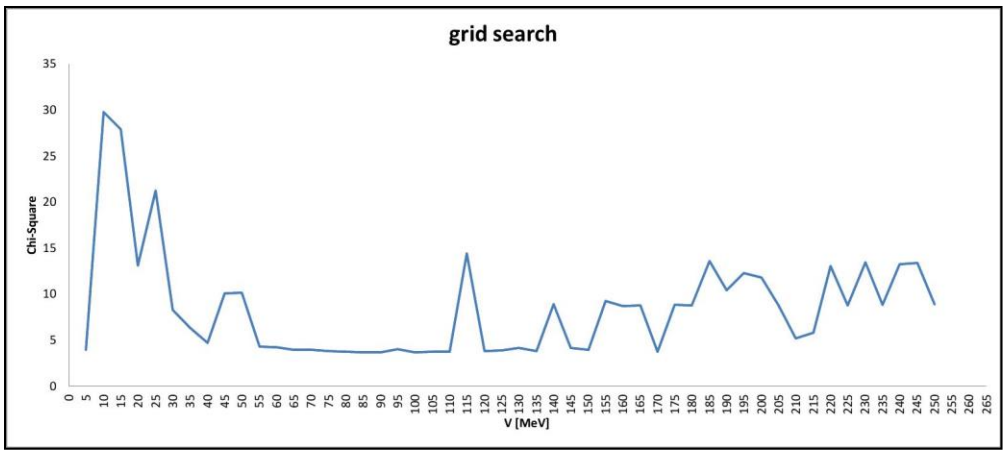

Figure 35: Grid search in the depth of the real potential (V) for the reaction $^{13}C(^{26}Mg,^{26}Mg)^{13}C$.

The fitting procedure was started performing a grid search in V (Figure 35), the depth of the real potential while the other five parameters (r_v, r_w, a_v, a_w, W) were set to fit the data for each point. The goodness of fit to the experimental data was determined with a χ^2 criterion which is given by

$$\boldsymbol{\chi^2 = \frac{1}{N-f} \sum_{i} \frac{(\sigma_{exp}(\theta_i) - \sigma_{theory}(\theta_i))^2}{\left(\Delta\sigma_{exp}(\theta_i)\right)^2}}, \qquad (4.7)$$

where N represents the number of the data points. f is the number of free parameters, while $\boldsymbol{\Delta\sigma_{exp}(\theta_i)}$ is for the experimental uncertainty of the data point i. After identifying the minima in χ^2 that were obtained by varying V, several were selected for a further fitting where the all six parameters (r_v, r_w, a_v, a_w, W, V) were run to determine the best fit. The extracted optical model potentials from the fits are presented in Table 1, where $r_{V(W)}$ and $a_{V(W)}$ are for the real (imaginary) radius parameter and diffuseness, respectively. J_V and J_W are respectively the volume integrals per nucleon pair of the real and imaginary part, which defined as

$$J = J_V + J_W = -\left(\frac{4\pi}{A_P A_T}\right)\int_0^\infty \big(V(r) + iW(r)\big)r^2 dr. \tag{4.8}$$

The other parameters labeled in the Table 1 are the root mean squared radii of the real and imaginary potentials given by

$$< R_V^2 >= \frac{\int_0^\infty V(r)r^4 dr}{\int_0^\infty V(r)r^2 dr}\ , and \tag{4.9}$$

$$< R_W^2 >= \frac{\int_0^\infty W(r)r^4 dr}{\int_0^\infty W(r)r^2 dr}. \tag{4.10}$$

Table 1: The optical model potential parameters for the elastic scattering of ^{26}Mg on ^{13}C.

Pot	V [MeV]	W [MeV]	r_V [fm]	r_W [fm]	a_V [fm]	a_W [fm]	χ^2	J_V [MeV fm^3]	R_V [fm]	J_W [MeV fm^3]	R_W [fm]
1	94.1	34.3	0.841	0.950	0.942	1.04	3.7	150	4.93	78	5.50
2	161	48.7	0.741	0.873	0.942	1.06	4.9	191	4.64	91	5.33

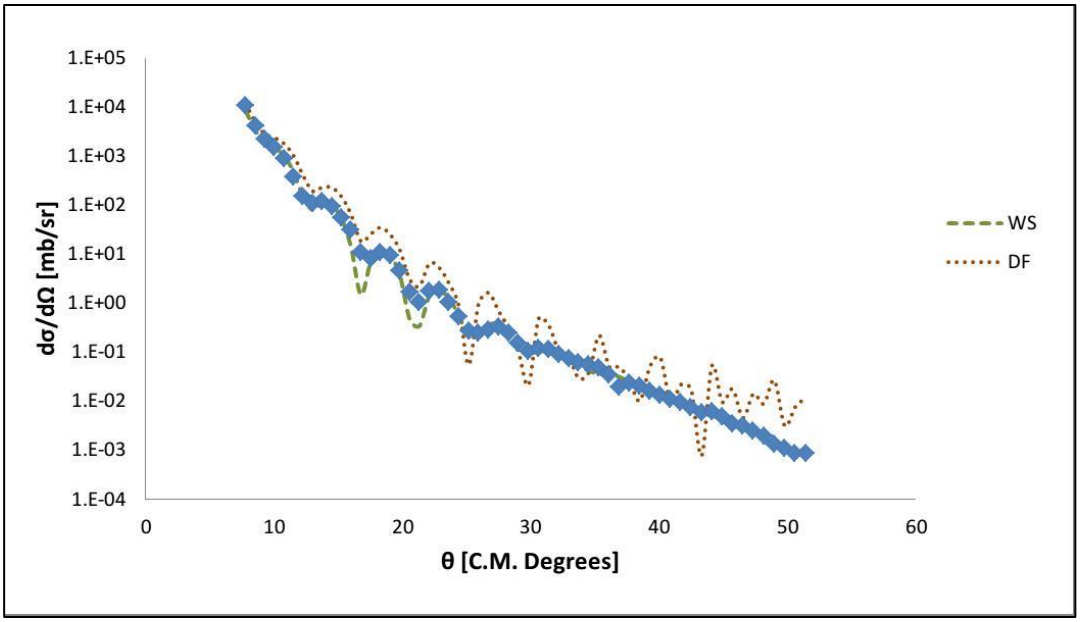

Figure 36: The angular distribution for the elastic scattering of ^{26}Mg from ^{13}C target. Experimental points are the blue dots. The green dash-line is the Woods-Saxon fit calculated using PTOLEMY, whereas the red pointed line is the double folding fit calculated using OPTIMINIX.

The result of the Woods-Saxon fit using the optical parameters from Pot.1 in Table 1 is shown in Figure 36. An alternative approach, the double folding (DF) method with the JLM effective interaction was also used to determine OMP for the ^{26}Mg+^{13}C elastic channel. A best fit to the data was obtained with N_v=0.37, N_w=1.00, t_v=1.2 and t_w=1.75, which can be seen in Figure 36.

Transfer Data

Due to similar Bρ values for the elastic scattering, the neutron transfer reaction ^{13}C(^{26}Mg,^{27}Mg)^{12}C was simultaneously measured for the ^{27}Mg ground state ($J^{\pi}=½^{+}$) from about 6^{o} to 30^{o} in the C.M.

The neutron transitions from the $1p_{1/2}$ orbital in ^{13}C to the $2s_{1/2}$ and $1d_{3/2}$ orbitals in ^{27}Mg were observed along the x-axis of the focal plane, as seen in Figure 37. To disentangle the ground state from the closely populated first excited state of ^{27}Mg, both were contained in the gate for further analysis. Then the positions of the ground and first excited state of ^{27}Mg were determined using RAYTRACE and the peaks were fitted using a multi-Gaussian peak fitting routine, as seen in Figure 38. The resulting function was integrated for each peak to extract the angular distribution for the ground state of ^{27}Mg.

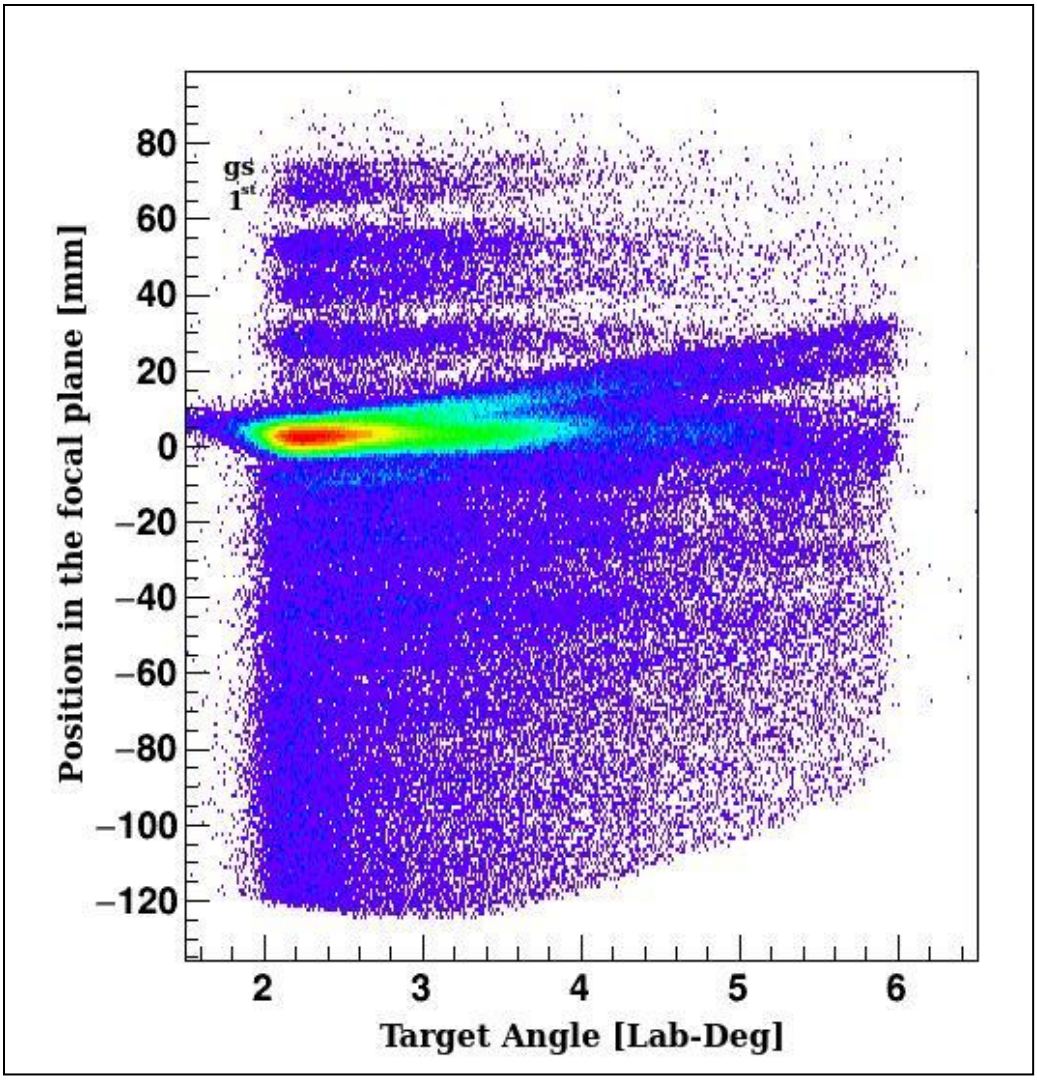

Figure 37: The POSCFP vs Target Angle histogram when the MDM was at 4^{o}.

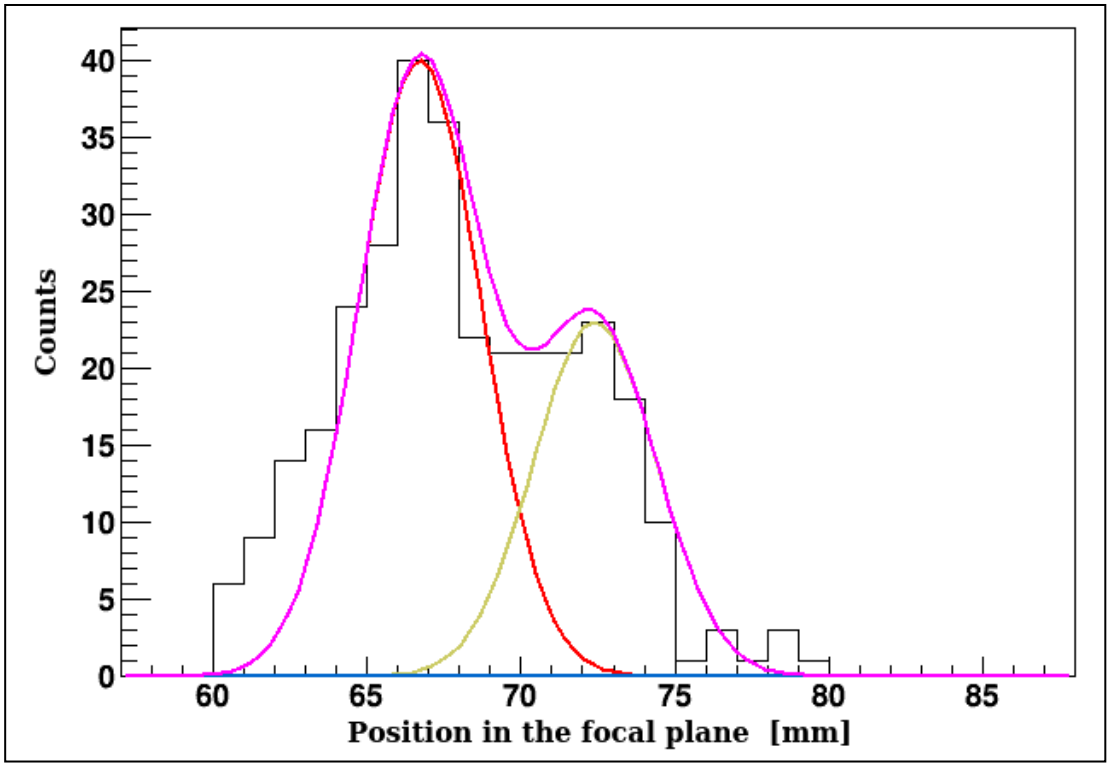

Figure 38: An example of a fit of Gaussian functions to the ground state (right-side) and the combination of the first (3/2+) and second (5/2+) excited state of ^{27}Mg.

The DWBA calculations were carried out using the PTOLEMY [39] and FRESCO [40] codes. These calculations were done using the same optical potential parameters in Table 1 for both the entrance and exit channels. The DWBA calculations were then normalized to the experimental angular distribution to obtain the $\boldsymbol{C^2_{s_{\frac{1}{2}}}}(^{27}Mg)$. Fits of the DWBA calculations to the data are shown in Figure 39.

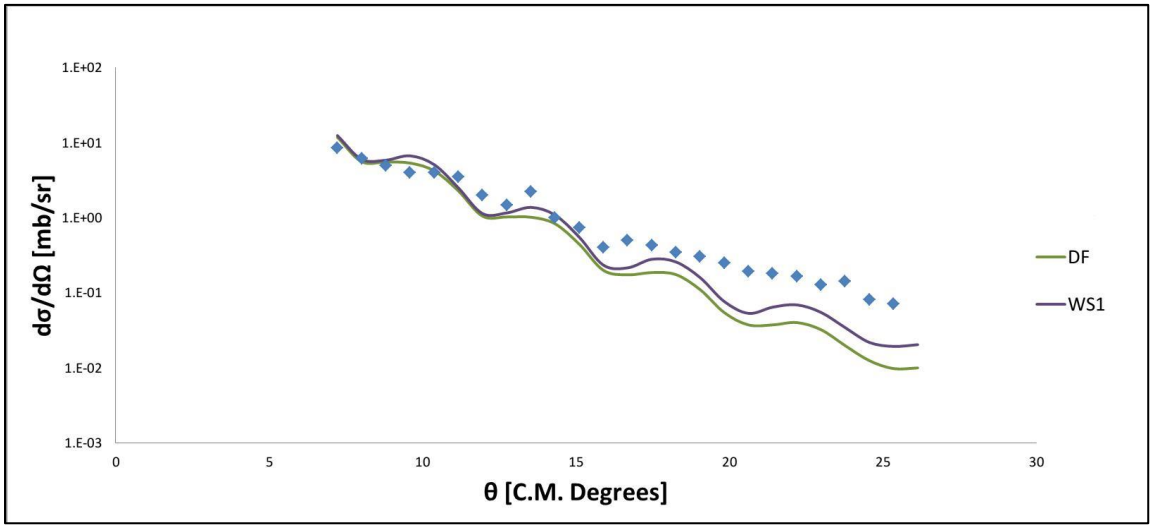

Figure 39: Fits of the DWBA calculations to the data. The calculated distribution for the ground state has been normalized to the experimental data. The green dash-line is the Woods-Saxon , while the red pointed line is the double folding.

Extracting the ANC

In order to extract the asymptotic normalization coefficients for the reaction ^{13}C(^{26}Mg,^{27}Mg)^{12}C, Eq. (2.81) can be written as

$$\frac{d\sigma}{d\Omega} = \sum C^2_{p_{\frac{1}{2}}}(13C)\, C^2_{s_{\frac{1}{2}}}(27Mg) \frac{\sigma^{DWBA}}{b^2_{p_{\frac{1}{2}}}(13C)\, b^2_{s_{\frac{1}{2}}}(27Mg)} \,. \qquad (4.11)$$

The value for the ANC for ^{13}C $\leftrightarrow$ ^{12}C + n, as determined in [28], is $C^2_{p_{\frac{1}{2}}}(^{13}C)$ = 2.31 ± 0.08 fm^{-1}. The value of the single particle ANC, on the other hand, is defined as in Eq. (2.70), and the Whittaker function is replaced by the corresponding Hankel function because the Sommerfeld parameter (η) for a neutron is zero. The calculated wave function divided by the Hankel function over radius was plotted as a function of the radius. The value in the asymptotic region where this function is flat gives the single

particle ANC. After the single particle ANC for both ^{13}C and ^{27}Mg was determined, the ANC for ^{27}Mg ↔ ^{26}Mg + n was obtained using the Eq. (4.11), which is $C^2_{s_{\frac{1}{2}}}(^{27}Mg)$ = 29.19 ± 3.50 fm^{-1}. In Figure 40 the values extracted for the ANC $C^2_{s_{\frac{1}{2}}}(27Mg)$ are compared with those of the extracted spectroscopic factor $S_{s_{\frac{1}{2}}}(27Mg)$ for different geometries of the Woods-Saxon neutron binding potential. It can be seen that the model dependent value of S varies over the range, while the ANC is almost constant. Hence, the reaction is peripheral.

The uncertainty in the value of the ANC for the ground state includes 6% from the measurement of the target thickness, 5% from the faraday cup normalization, 9% from the data extraction and disentanglement from the first excited state of ^{27}Mg, and 5% statistical errors, 1.5% for the normalization of the cross section with different optical potentials in Table 1. Therefore, the overall uncertainty in determining the C^2 is almost 13.5%.

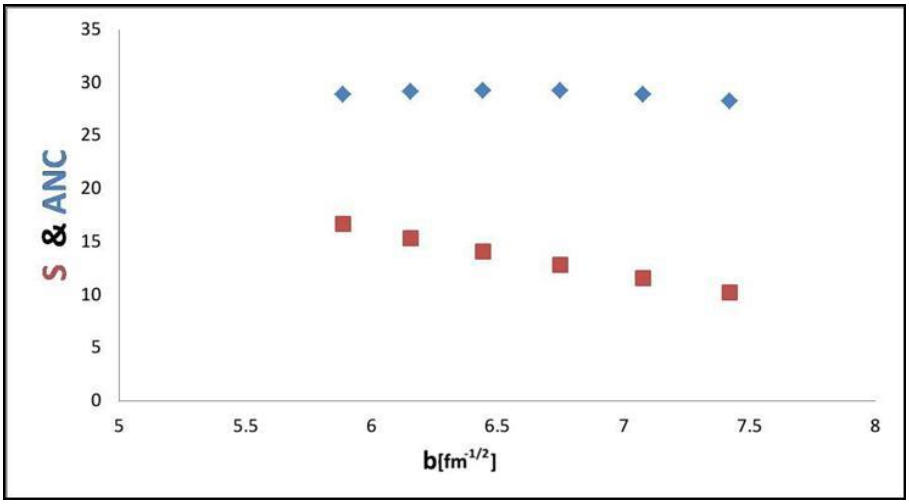

Figure 40: Comparison between the spectroscopic factor (red squares) and the ANC C^2 (blue diamonds) for the ground state of ^{27}Mg as a function of the single particle ANC $b_{s1/2}$.

The $^{13}C(^{28}Si,^{28}Si)^{13}C$ Experiment

Elastic Scattering Data

The ^{28}Si beam at 11.86 MeV/A impinged on the ^{13}C target to measure the elastic scattering angular distribution at several spectrometer angles, allowing overlapping measurements for consistency checks of the data. After completing the position calibration, the angle calibration and gain matching processes, the focal plane position was set for the $^{13}C(^{28}Si,^{28}Si)^{13}C$.

Since this experiment was performed after the second upgrade of the Oxford detector was completed, particle identification was started by plotting the histograms showing the energy loss of the particles through the first Micromegas array (MM1) against the energy loss of the particles through both the first and second Micromegas arrays (MMT), and then a simple multiplicity condition was set on the data result to decrease the background scattering, as seen in Figure 40. When the MDM was at 4^{o}, for instance, after applying the multiplicity condition, the total counts on the MM1vsMMT histogram were decreased by 6.25%, whereas the counts of the elastic scattering band in the TargetAngle vs POSFP histogram were only decreased by 0.065%.

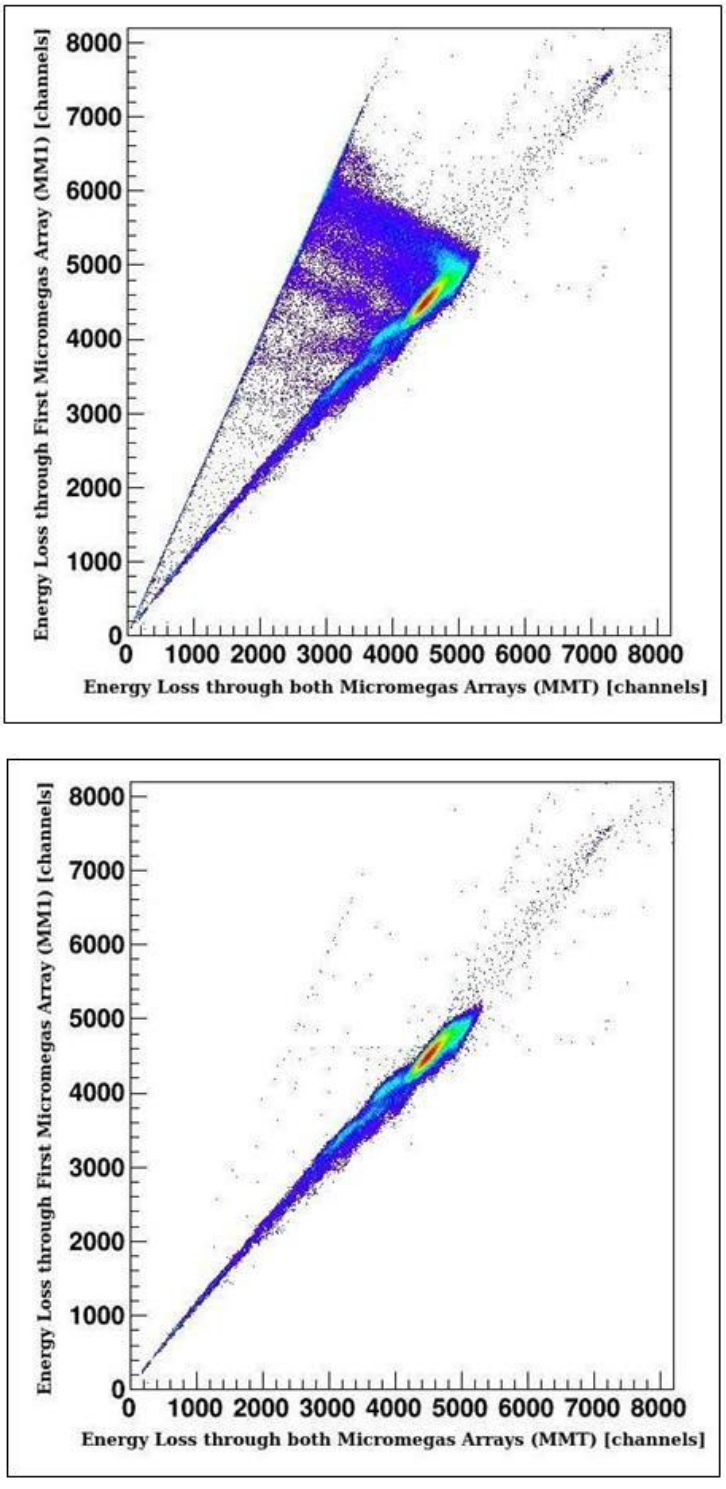

Figure 41: Using the multiplicity condition the raw data was accepted only if it passed through Row 8, which is the last row for the second Micromegas Array. On the top histogram the multiplicity condition was not applied. The histogram where the multiplicity condition was applied is shown at the bottom.

The selected polygon gate (Figure 41) from the MM1 vs MM2 histogram was plotted on the TargetAngle vs POSFP, and the position of elastic scattering of ^{28}Si on ^{13}C in the focal plane was determined using RAYTRACE [37], as shown in Figure 42. The inelastic scattering and the scattering on the heavier impurities were also observed.

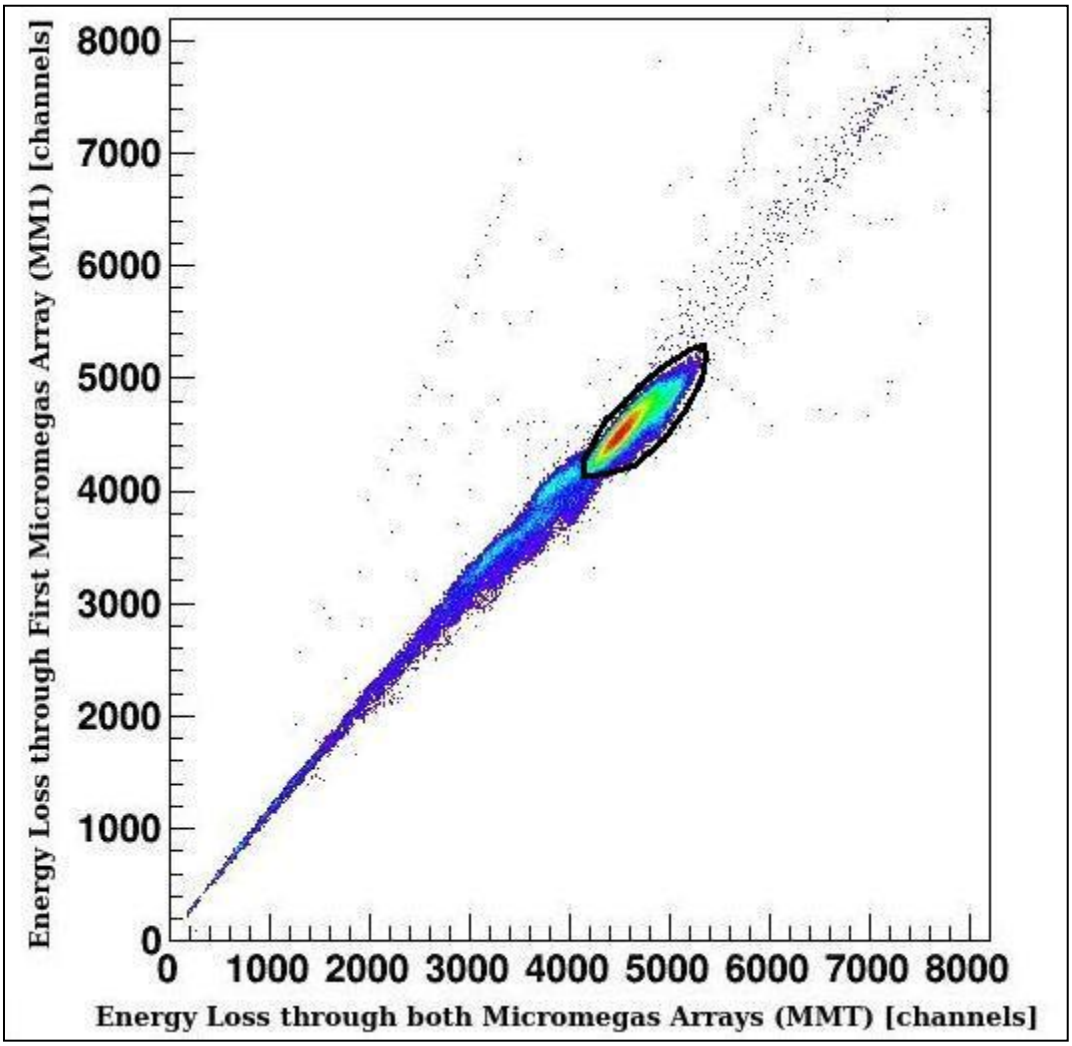

Figure 42: Particle identification for the reaction ^{13}C(^{28}Si,^{28}Si)^{13}C.

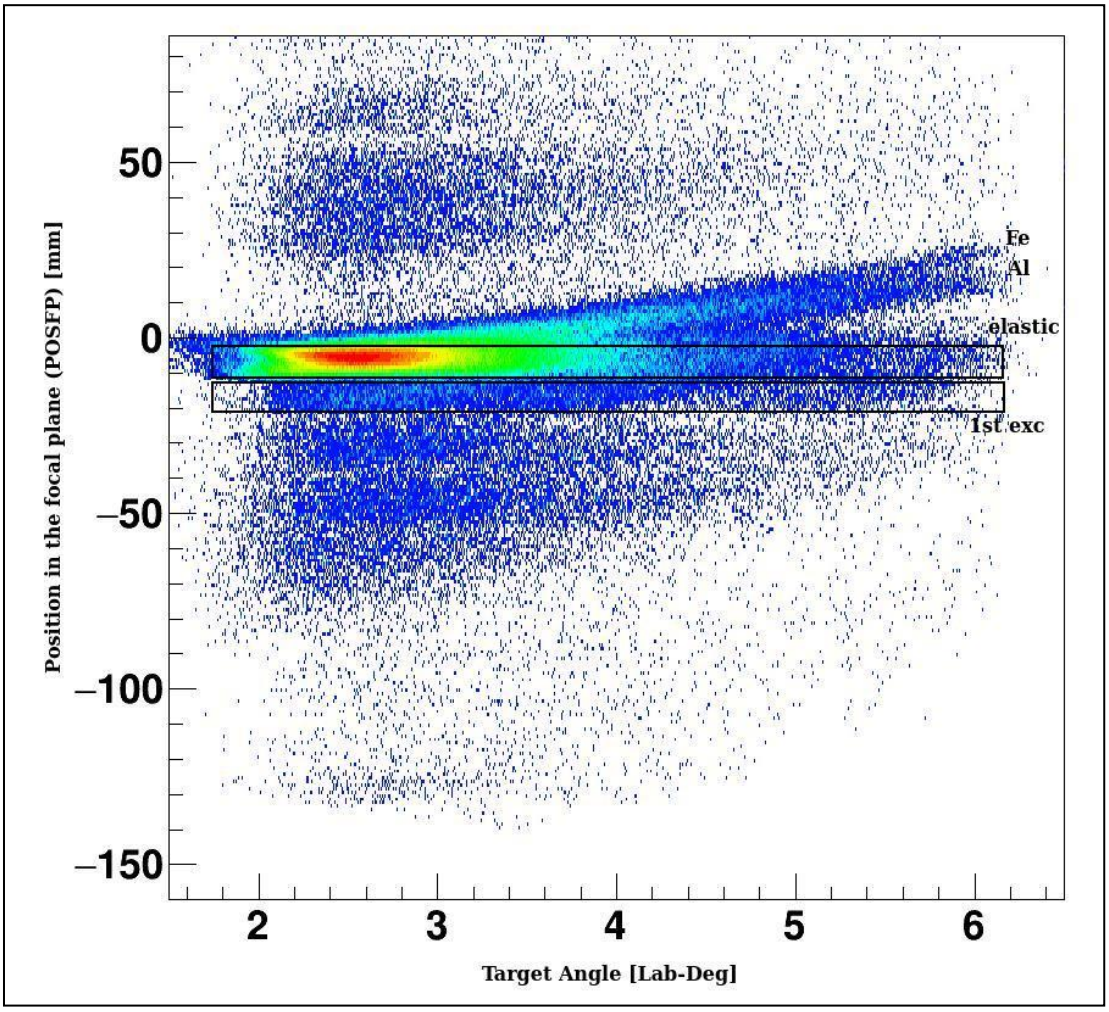

Figure 43: The POSCFP vs Target Angle histogram for the reaction $^{13}C(^{28}Si,^{28}Si)^{13}C$ when the MDM was at 4^{o}.

The second polygon gate was placed around the elastic scattering group, and projected onto the target angle axis, and divided into 16 bins that were 0.25^{o} in width. After Faraday cup normalization and the correction for the dead time of the data acquisition were applied, the angular distribution for the reaction $^{13}C(^{28}Si,^{28}Si)^{13}C$ was obtained in the range 8^{o}-52^{o} in the C.M.

Optical Model Fits

Fitting to the experimental data was performed using the code PTOLEMY [39]. As noted above, the imaginary surface and spin orbit terms were excluded to minimize the complexity of the fitting procedure, and the same procedure was followed as was used for ^{26}Mg. Using the χ^2 as criterion to determine the best fit to the data, a grid search was performed in V, and then a complete search on all six parameters was run to obtain the best fit to the data. All parameters are presented in Table 2.

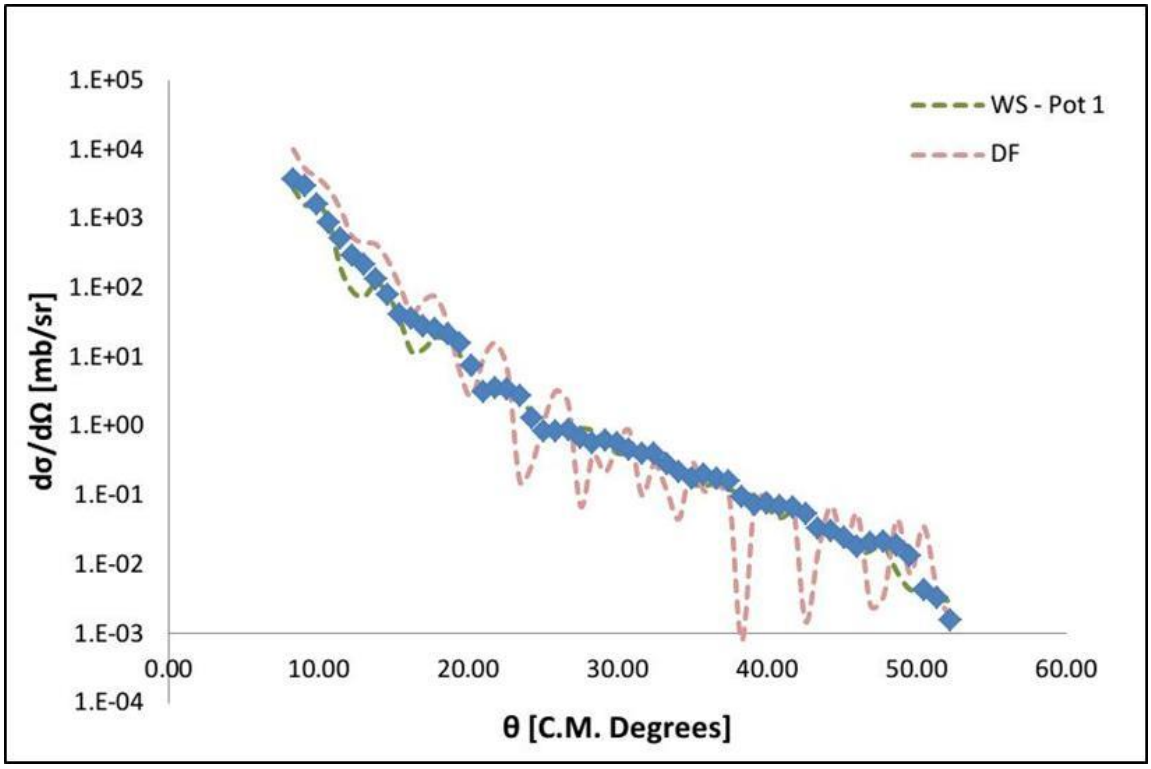

Figure 44: The angular distribution for the elastic scattering of ^{28}Si on ^{13}C. Experimental points are the blue dots. The green dashed-line is the Woods-Saxon fit (potential parameters are row 1 in Table 2).

Table 2: The optical model potential parameters the $^{13}C(^{28}Si,^{28}Si)^{13}C$ reaction.

Pot	V [MeV]	W [MeV]	r_V [fm]	r_W [fm]	a_V [fm]	a_W [fm]	χ^2	J_V [MeV fm^3]	R_V [fm]	J_W [MeV fm^3]	R_W [fm]
1	130	13.1	0.651	1.16	1.32	0.686	5.4	156.3	5.6	41.18	5.47
2	242	17.1	0.744	1.26	1.11	0.90	7.2	315.8	5.16	72.25	6.23

The result of the Woods-Saxon fit using the optical parameters from Pot.1 in Table 2 is shown in Figure 43. The elastic scattering data have been also analyzed using the double folding (DF) method with the JLM effective interaction. The fitting procedure started with the average values N_v=0.37, N_w=1.0, t_v=1.2 and t_w=1.75 and a reasonable fit to the data was determined with N_v=0.45, N_w=1.00 t_v=1.2 and t_w=1.75.

The $^{13}C(^{32}S,^{32}S)^{13}C$ Experiment

Elastic Scattering Data

The elastic scattering angular distribution was measured for spectrometer angles 2^{o}-16^{o} by bombarding the ^{13}C target with a ^{32}S beam at 11.88 MeV/A. Following the same procedures that were followed as described above, the angular distribution for the reaction $^{13}C(^{32}S,^{32}S)^{13}C$ was extracted in the range 9^{o}-57^{o} in the C.M. The elastic scattering on impurities in the target along with the ground and first excited state of ^{32}S can be seen in Figure 44.

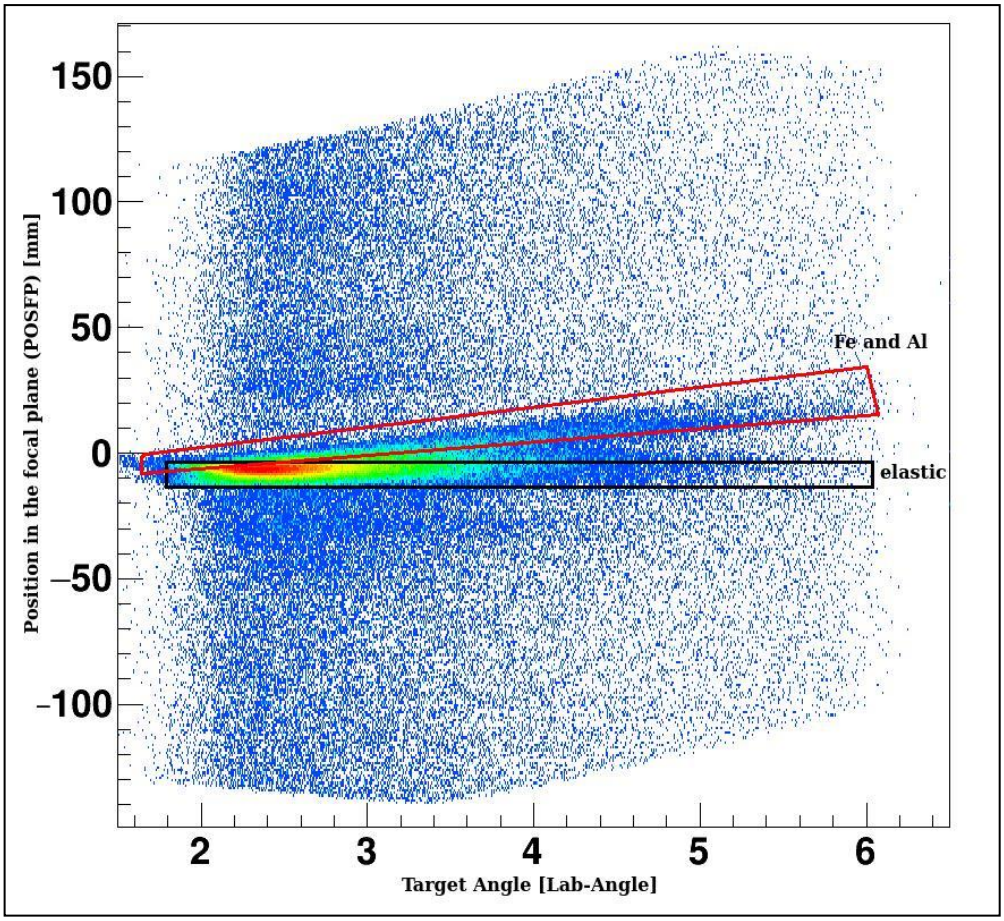

Figure 45: The POSCFP vs Target Angle histogram for the $^{13}C(^{32}S,^{32}S)^{13}C$ reaction.

Optical Model Fits

Optical potentials for the reaction $^{13}C(^{32}S,^{32}S)^{13}C$ have been determined using phenomenological Woods-Saxon shapes. The same procedure was followed as described previously. The extracted optical potentials are listed in Table 3. The angular distributions for the elastic scattering of $^{32}S+^{13}C$ and the result of the fits to the data with the Woods-Saxon form can be seen in Figure 45. The elastic scattering data also have been fitted using the double folding (DF) method with the JLM effective interaction. A reasonable fit to the data was obtained with N_v=0.40, N_w=0.70, t_v=1.2 and t_w=1.75.

Table 3: The optical model potential parameters for the $^{13}C(^{32}S,^{32}S)^{13}C$.

Pot	V	W	r_V	r_W	a_V	a_W	χ^2	J_V	R_V	J_W	R_W
	[MeV]	[MeV]	[fm]	[fm]	[fm]	[fm]		[MeV fm^3]	[fm]	[MeV fm^3]	[fm]
1	146	15.8	0.855	1.27	1.24	1.31	11.12	260.86	5.88	73.91	7.29
2	172	14.3	0.904	1.40	1.19	1.22	11.60	337.16	5.88	83.06	7.52

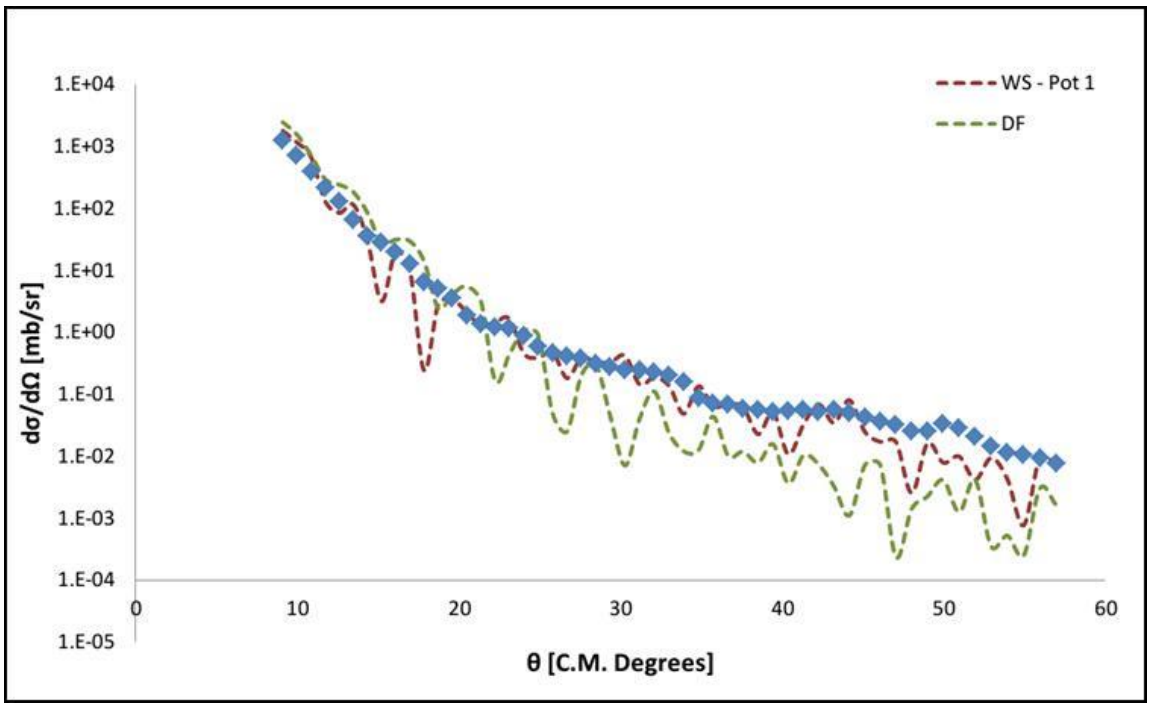

Figure 46: Experimental points are the blue dots. The fit of a Woods-Saxon potential to the data is shown with the purple line.

CHAPTER V

ASTROPHYSICAL REACTION RATE

The Direct Capture Reaction Rate for ^{26}Si(p,γ)^{27}P

The ANC for ^{27}Mg is deduced in the previous chapter. Using mirror symmetry [41, 42], the ANC for the ground state of ^{27}P was obtained from the corresponding ANC for its mirror pair, ^{27}Mg.

$$C^2_{s_{\frac{1}{2}}}(^{27}P) = \frac{b^2_{s_{\frac{1}{2}}}(^{27}P)}{b^2_{s_{\frac{1}{2}}}(^{27}Mg)} C^2_{s_{\frac{1}{2}}}(^{27}Mg) \qquad (5.1)$$

The single-particle ANC for ^{27}P was calculated for a proton bound in a Woods-Saxon potential with the same geometry (r_0=1.25 fm and a=0.65 fm) that was used for a neutron bound in ^{27}Mg. The ratio $b^2(^{27}P)/b^2(^{27}Mg)$ was found to be 38.6 ± 0.1 for the ground state ($J^{\pi}=1/2^{+}$). Inserting this ratio and the values of the ANC for ^{27}Mg, the square of proton ANC for ^{27}P→^{26}Si+p is determined to be 1126±152 fm^{-1}. Our value for $C^2_{s_{\frac{1}{2}}}(^{27}P)$ is almost 40% less than the value reported in [43].

In order to estimate the ^{26}Si(p,γ)^{27}P direct-capture reaction rate, the astrophysical S-factor was determined using the RADCAP code [44]. The depth (V_0) of the nuclear binding potential was adjusted to reproduce the binding energy of the ground state E_p in ^{27}P, which is 870 keV, while the other parameters were fixed. The bound-state wave function was then calculated. Assuming the direct capture into the ground state of ^{27}P is dominated by an E1 transition from the incoming proton to the bound *s* state for the ^{26}Si(p,γ)^{27}P reaction, the astrophysical S-factor calculation was done for the energy range E=0.01 to 1.0 MeV, in steps of 0.003 MeV. The calculated energy dependence of the S-factor was plotted for the direct proton capture reaction ^{26}Si(p,γ)^{27}P, and fitted with a second-degree polynomial equation, as seen in Figure 46.

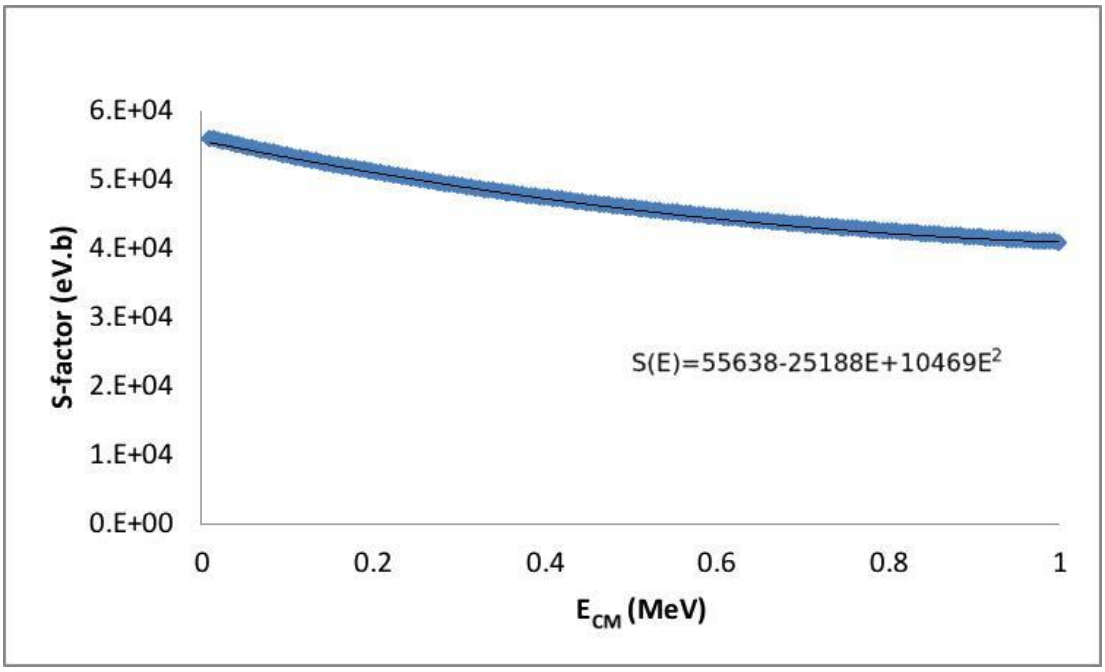

Figure 47: The dependence of the S-factor on the C.M. energy for the $^{26}Si(p,\gamma)^{27}P$ reaction. Fitting it with a second degree polynomial function gives $S(0)=(5.56\pm0.75)x10^{4}$ eV b.

The astrophysical S-factor for the direct capture for $^{26}Si(p,\gamma)^{27}P$ was found to be $S_{1\text{-}26}(0)=(5.56\pm0.8)x10^{-2}$ MeV.b in this work. In [43] the neutron ANC of $^{27}Mg\rightarrow^{26}Mg+n$ was deduced by analyzing the existing $^{26}Mg(d,p)^{27}Mg$ angular distribution data [45]. Using charge symmetry the proton ANC of $^{27}P\rightarrow^{26}Si+p$ was extracted, and used to obtain the rate of the direct capture into the ^{27}P ground state. As seen in Table 4, the astrophysical S-factor of the direct capture for the $^{26}Si(p,\gamma)^{27}P$ reaction was found to be $8.7 \pm 1.1\ x10^{-2}$ MeV b in [43], which is about 1.5 times larger than our value. The S-factor value also was predicted using a shell model calculation in [12], and the value, as listed in Table 4, is about 40% less than our value.

Table 4: Comparison of the astrophysical S-factor of the direct capture for the $^{26}Si(p,\gamma)^{27}P$.

	S_0 [MeV.b]
Ref. [12]	3.63×10^{-2}
Ref. [43]	$8.7 \pm 1.1 \times 10^{-2}$
This work	$5.6 \pm 0.8 \times 10^{-2}$

The central energy of the Gamow peak for $p+^{26}Si$ is at $E_0=0.7T_9^{2/3}$ [MeV]. Inserting this equation into Eq. (2.38), the effective S-factor (S_{eff}) in terms of T_9 is given by

$$S_{\text{eff}}(T_9) = 55638\left[1 + 0.017T_9^{1/3} - 0.32T_9^{2/3} - 0.03T_9 + 0.09T_9^{4/3} + 0.03T_9^{5/3}\right] \quad (5.2)$$

Substituting Eq. (5.2) and Eq. (2.35) into Eq. (2.39), the direct capture reaction rate for $^{26}Si(p,\gamma)^{27}P$ can be obtained as a function of T_9 using

$$\mathbf{N_A} < \boldsymbol{\sigma v} > = \tau^2 \, \boldsymbol{S_{eff}}(\boldsymbol{T_9}) \boldsymbol{e}^{-\tau} \left[\frac{\boldsymbol{cm^3}}{\boldsymbol{mol.s}}\right] \quad (5.3)$$

where $\tau = 24.36/T_9^{1/3}$. In addition to the direct capture calculated above, there is a resonant contribution through the first ($J^{\pi}=3/2^{+}$) and second ($J^{\pi}=5/2^{+}$) excited state of ^{27}P. The contribution of these resonances to the reaction rate has been estimated using Eq. (2.42). The resonant energies are determined with $E_r=E_{exc}-S_p$. The measured excitation

energy for the first ($J^{\pi}=3/2^{+}$) and second ($J^{\pi}=5/2^{+}$) excited state are 1.119 MeV and 1.631 MeV, respectively [46], and the value of the S_p is 0.861 MeV [47].

The resonant strength for ($J^{\pi}=3/2^{+}$) was determined to be 1.51×10^{-9} MeV in [12] and 3.5×10^{-9} MeV in [48], whereas they were estimated to be 9.9×10^{-10} MeV in both [12] and [48] for the ($J^{\pi}=5/2^{+}$). Hence, these values are adopted in estimating the reaction rates for two resonant captures. The reaction rates for the direct capture and two resonant captures are shown in Figure 47, and it can be seen that the resonant capture into the first excited state of ^{27}P dominates the total reaction rate for $T_9>0.1$.

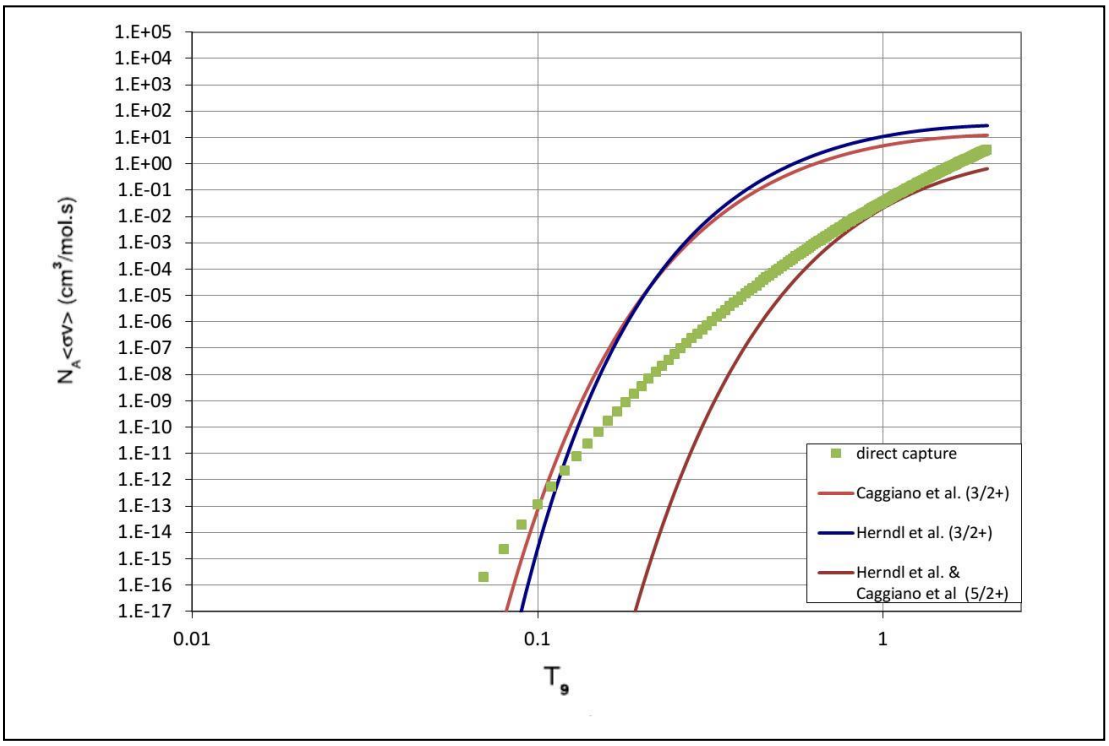

Figure 48: The direct and resonant capture rate contributions to the ^{26}Si(p,γ)^{27}P reaction.

The estimated direct capture reaction rate in this work is also compared with the previously determined rate by Caggiano et al. [48], as seen in Figure 48. Our rate is two times larger than the estimate by Caggiano et al. [48].

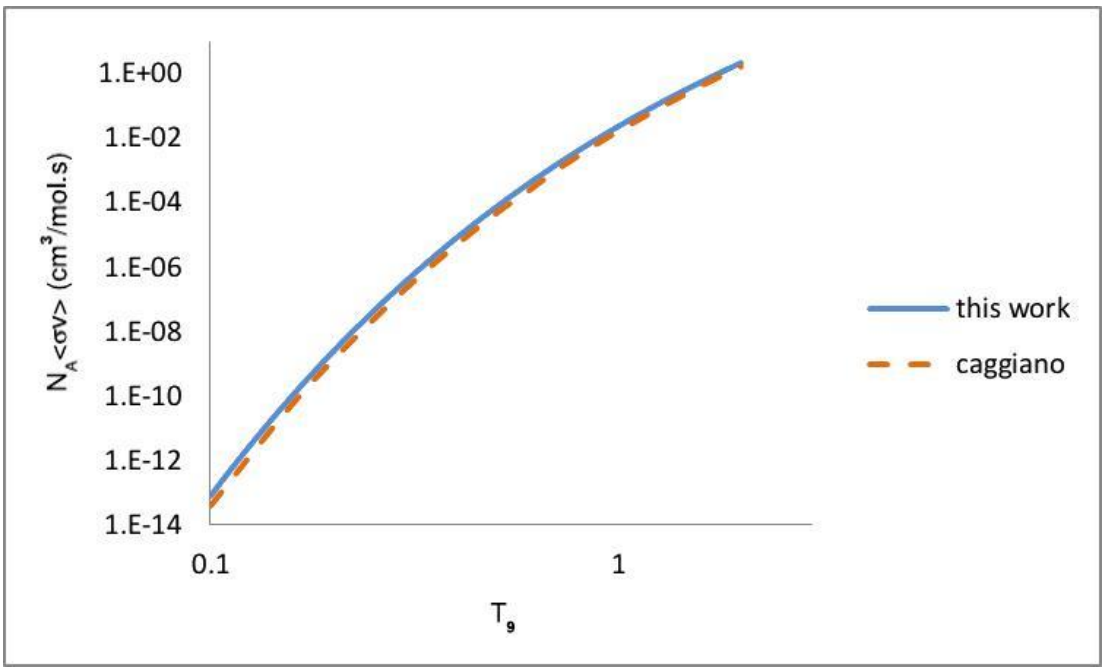

Figure 49: Comparison between the estimated reaction rate in this work with the previously determined rates by Caggiano.

CHAPTER VI

CONCLUSION

The ^{26}Si(p,γ)^{27}P reaction plays an important role as one of the destruction mechanisms of ^{26}Al in stellar environments. The reaction rate for ^{26}Si(p,γ)^{27}P has been estimated based on theoretical models. Large uncertainties however exist due to the very limited experimental information. The work here therefore is an important step in this quest. Due to the experimental difficulties of direct measurements, the asymptotic normalization coefficient technique has been used to determine the reaction rate for ^{26}Si(p,γ)^{27}P by measuring the ANC of its mirror nuclear system since mirror symmetry means that the spectroscopic factors of {^{27}P,^{27}Mg} are the same. Therefore, using the advantages of stable beam and target, the ^{13}C(^{26}Mg,^{27}Mg)^{12}C experiment has been performed to extract the neutron ANC for the ground state ($J^{\pi}=1/2^{+}$) in ^{27}Mg yielding ($C^2_{s_{\frac{1}{2}}}(^{27}Mg) = 29.19 \pm 3.94\ \mathrm{fm}^{-1}$), and the ANC in ^{27}Mg is used to determine its corresponding proton ANC in ^{27}P ($C^2_{s_{\frac{1}{2}}}(^{27}P) = 1126 \pm 152\ \mathrm{fm}^{-1}$) using mirror symmetry. The value of SF= $C^2_{s_{\frac{1}{2}}}(^{27}P)/b^2_{s_{\frac{1}{2}}}(^{27}P)$ was determined to be 0.64±0.09 and is involved in determining the astrophysical S-factor for the ^{26}Si(p,γ)^{27}P reaction, which gives $S_{1\text{-}26}(0)= (5.6\pm0.8)\times10^{-2}$ MeV b. This value is about 1.5 times larger than the previously reported value in [9], and about 40% less than the value presented in [33]. The estimated direct proton capture reaction rate is found to be two times larger than the previous estimation made by [48].

The ^{13}C(^{28}Si,^{28}Si)^{13}C and ^{13}C(^{32}S,^{32}S)^{13}C experiments were also performed to provide the optical model parameters that may be needed for systems around A~30, and to help extend the systematics for optical model potentials to higher Z. Prior to these two elastic scattering measurements, the Oxford detector, a gridded ionization chamber used as a focal plane detector, was modified using Micromegas detector technology in order to allow for extending reaction measurements to higher Z. Further study with different

heavier particles is also intended to be performed with the system. Testing the newly upgraded Oxford detector with a different gas mixture might be one choice for further study in the future. It was also worth noting that the upgraded Oxford detector is in particular intended for use in studies with radioactive beams as the development of the radioactive beam (RIB) technique proceeds further [49, 50]. Along with the availability of a reaccelerated radioactive beam of ^{26}Si from the Texas A&M Reaccelerated Exotics (T-REX), the rate of the radioactive proton capture reaction the ^{26}Si(p,γ)^{27}P can be determined in the future with an asymptotic normalization coefficient measurement from the proton transfer reaction by means of the improved Oxford detector.

REFERENCES

1. Rolfs, C.E. and W.S. Rodney, Cauldrons in the Cosmos. 1988, Chicago, London: The University of Chicago Press.

2. Iliadis, C., Nuclear Physics of Stars. 2007, Weinheim, Germany: Wiley-VCH Verlag GmbH &Co. KgaA.

3. Thompson, I.J. and F.M. Nunes, Nuclear Reactions for Astrophysics. 2009, The Edinburgh Building, Cambridge CB2 8RU, UK: Cambridge University Press.

4. Champagne, A.E. and M. Wiescher, Explosive Hydrogen Burning. Annu. Rev. Nucl. Part. Sci. , 1992. 42: p. 39-76.

5. Smith, M.S. and K.E. Rehm, Nuclear Astrophysics Measurements With Radioactive Beams. Annual Review of Nuclear and Particle Science, 2001. 51(1): p. 91-130.

6. Coc, A., Porquet M., Lifetimes of ^{26}Al and ^{34}Cl in an Astrophysical Plasma. ArXiv:astro-ph/9910186 1999.

7. Mahoney, W.A., et al., Diffuse Galactic Gamma-ray Line Emission from Nucleosynthetic Fe-60, Al-26, and Na-22 - Preliminary Limits from HEAO 3. Astrophysical Journal, , 1982. 262: p. 742, 748.

8. Diehl, R., et al., COMPTEL Observations of the 1.809 MeV Gamma-ray Line from Galactic Al-26. The Astrophysical Journal Supplement Series, 1994. 92: p. 429-432.

9. Diehl, R., Measuring ^{26}Al and ^{60}Fe in the Galaxy. New Astronomy Review, 2006. 50: p. 534-539.

10. Jose, J., A. Coc, and M. Hernanz, Nuclear Uncertainties in the NeNa-MgAl Cycles and Production of ^{22}Na and ^{26}Al During Nova Outbursts. The Astrophysical Journal Supplement Series, 1999. 520.

11. Pluschke, S., Diehl, R., The Comptel 1.809 Mev Survey. Astro-Ph 0104047, 2001. 1.

12. Herndl, H., et al., Proton Capture Reaction Rates in the rp Process. Physical Review C, 1995. 52(2): p. 1078-1094.

13. M. Wiescher, et al., Explosive Hydrogen Burning in Novae, Astron. Astrophys., 1986. 160: p. 56-72.

14. Clayton, D.D., Principles of Stellar Evolution and Nucleosynthesis. 1968, Chicago, London: The University of Chicago Press.

15. Mukhamedzhanov, A., Clark, H. , Gagliardi C. A., Asymptotic Normalization Coefficients and Astrophysical Radiative Capture Reactions. Nuclear Physics A, 1998. 631: p. 788-792.

16. Mukhamedzhanov, A.M., Blokhintsev, L. D. , Brown , S. , Burjan, V. ,, Indirect Techniques in Nuclear Astrophysics: Asymptotic Normalization Coefficient and Trojan Horse. Nuclear Physics A, 2007. 787: p. 321-328.

17. Glendenning, N.K., Direct Nuclear Reactions. 1983, Singapore: World Scientific Publishing Co. Pte. Ltd.

18. Woods, R.D. and D.S. Saxon, Diffuse Surface Optical Model for Nucleon-Nuclei Scattering. Physical Review, 1954. 95(2): p. 577-578.

19. Jeukenne, J.P., A. Lejeune, and C. Mahaux, Optical-Model Potential in Finite Nuclei from Reid's Hard Core Interaction. Physical Review C, 1977. 16(1): p. 80-96.

20. Tribble, R.E., Indirect Techniques in nUclear Astrophysics: The ANC Method. Nuclear Instruments and Methods in Physics Research Section B: Beam Interactions with Materials and Atoms, 2005. 241(1–4): p. 204-208.

21. McCleskey, M., et al., Determination of the Asymptotic Normalization Coefficients for $C^{14}+n\leftrightarrow C^{15}$, the $C^{14}(n,\gamma)C^{15}$ Reaction Rate, and Evaluation of a New Method to Determine Spectroscopic Factors. Physical Review C, 2014. 89(4).

22. Tribble, R.E., et al., Indirect Techniques in Nuclear Astrophysics: A Review. Rep Prog Phys, 2014. 77(10): p. 106901.

23. Mukhamedzhanov, A.M., et al., Asymptotic Normalization Coefficients for B^{10} -> Be^{9} + p. Physical Review C, 1997. 56(3): p. 1302-1312.

24. Mukhamedzhanov, A.M., C.A. Gagliardi, and R.E. Tribble, Asymptotic Normalization Coefficients, Spectroscopic Factors, and Direct Radiative Capture Rates. Physical Review C, 2001. 63(2).

25. Kroha, V., Azhari, A., Asymptotic Normalization Coefficients in Nuclear Astrophysics. Nuclear Physics A, 2003. 719: p. 119-122.

26. Gagliardi, C.A., Astrophysical S Factors Determined from Asymptotic Normalization Coefficients Measured in Peripheral Transfer Reactions. Nuclear Physics A, 2001. 688: p. 536-538.

27. Timofeyuk, N.K., P. Descouvemont, and I.J. Thompson, Threshold Effects in the $^{27}P(3/2^{+})\rightarrow{}^{26}Si+p$ and $^{27}Mg(3/2^{+})\rightarrow{}^{26}Mg+n$ Mirror Decays and the Stellar Reaction $^{26}Si(p,\gamma)^{27}P$. Physical Review C, 2008. 78(4).

28. Al-Abdullah, T., et al., Stellar Reaction Rate for $Mg^{22}+p\rightarrow Al^{23}$ from the Asymptotic Normalization Coefficient in the Mirror Nuclear System $Ne^{22}+n\rightarrow Ne^{23}$. Physical Review C, 2010. 81(3).

29. Pringle, D.M., et al., The Oxford Mdm-2 Magnetic Spectrometer. Nuclear Instruments and Methods in Physics Research, 1986. A245: p. 230-247.

30. Mccleskey, M., $^{14}C(n,\gamma)^{15}C$ As A Test Case In The Evaluation Of A New Method To Determine Spectroscopic Factors Using Asymptotic Normalization Coefficients, in Physics Department. 2011, Texas A&M University.

31. Winfield, J.S., et al., Focal Plane Detector For The Oxford Mdm-2 Spectrometer. Nuclear Instruments and Methods in Physics Research A251 (1986) 297-306, 1986. A251: p. 297-306.

32. Al-Abdullah, T.A., Extracting The Asymptotic Normalization Coefficients In Neutron Transfer Reactions To Determine The Reaction Rates For $^{22}Mg(p,gamma)^{23}Al$ and $^{17}F(p,gamma)^{18}Ne$, in Physics Department. 2007, Texas A&M University.

33. Giomatarisa, Y., et al., MICROMEGAS: A High-Granularity Position-Sensitive Gaseous Detector for High Particle-flux Environments. Nuclear Instruments and Methods in Physics Research, 1996. A 376: p. 29-35.

34. Pollacco, E., et al., AstroBox: A Novel Detection System for Very Low-Energy Protons from β-Delayed Proton Decay. Nuclear Instruments and Methods in Physics Research Section A: Accelerators, Spectrometers, Detectors and Associated Equipment, 2013. 723: p. 102-108.

35. Nakhostin, M., Performance of a low-pressure Micromegas-like gaseous detector. Nuclear Instruments and Methods in Physics Research Section A: Accelerators, Spectrometers, Detectors and Associated Equipment, 2009. 598(2): p. 496-500.

36. Spiridon, A., et al., Upgrade of the TAMU MDM-focal plane detector with MicroMegas technology. Nuclear Instruments and Methods in Physics Research Section B: Beam Interactions with Materials and Atoms, 2016. 376: p. 364-368.

37. Kowalski, S. and H.A. Enge, Computer Code RAYTRACE (unpublished),. 1986: University of Oxford, UK.

38. Tarasov, O.B. and D. Bazin, LISE++: Exotic Beam Production with Fragment Separators and Their Design. Nuclear Instruments and Methods in Physics Research Section B: Beam Interactions with Materials and Atoms, 2016. 376: p. 185-187.

39. Rhoades-Brown, M., S. Pieper, and M. Macfarlane, Computer Code PTOLEMY. 1978, Argonne National Lab Report ANL-76-11-rev-1.

40. Thompson, I.J., Coupled Reaction Channels Calculations in Nuclear Physics. Computer Physics Reports, 1988. 7(4): p. 167-212.

41. Timofeyuk, N.K. and P. Descouvemont, Asymptotic Normalization Coefficients for Mirror Virtual Nucleon Decays in a Microscopic Cluster Model. Physical Review C, 2005. 71(6).

42. Timofeyuk, N.K., R.C. Johnson, and A.M. Mukhamedzhanov, Relation Between Proton and Neutron Asymptotic Normalization Coefficients for Light Mirror Nuclei and its Relevance to Nuclear Astrophysics. Phys Rev Lett, 2003. 91(23): p. 232501.

43. Guo, B., et al., Determination of the astrophysical $Si^{26}(p,\gamma)P^{27}$ Reaction Rate from the Asymptotic Normalization Coefficients of $Mg^{27}\rightarrow Mg^{26}+n$. Physical Review C, 2006. 73(4).

44. Bertulani, C.A., RADCAP: A Potential Model Tool for Direct Capture Reactions. Computer Physics Communications. 156(1): p. 123-141.

45. Meurders, F. and A. Van Der Steld, Investigation of the $^{26}Mg(d, p)^{27}Mg$ Reaction. Nuclear Physics A, 1974. 230(2): p. 317-328.

46. Togano, Y., et al., Study of $^{26}Si(p,\gamma)^{27}P$ Reaction Using Coulomb Dissociation Method. Nuclear Physics A, 2005. 758: p. 182-185.

47. Audi, G., A.H. Wapstra, and C. Thibault, The Ame2003 Atomic Mass Evaluation: (II). Tables, Graphs and References. Nuclear Physics A, 2003. 729(1): p. 337-676.

48. Caggiano, J.A., et al., Spectroscopy of ^{23}Al and ^{27}P Using the (^{7}Li,^{8}He) Reaction and the Implications for ^{22}Na and ^{26}Al Nucleosynthesis in Explosive Hydrogen Burning. Physical Review C, 2001. 64(2).

49. Tribble, R.E., Radioactive Beams at Texas A&M University: Recent Results and Future Plans. Nuclear Physics A, 2004. 746: p. 27-31.

50. Tribble, R.E., Abegglen F., Chubarian G., Clark H.L., A Facility Upgrade At Texas A&M University For Accelerated Radioactive Beams. The European Physical Journal Special Topics, 2007. 150(1): p. 255-258.